Development and Testing of a Three-dimensional Deepwater Oil Spill Model (DWOSM) to Predict the Transport and Fate of Subsea Blowouts

Zhaoyang Yang

A Thesis

In the Department

of

Building, Civil, and Environmental Engineering

Presented in Partial Fulfillment of the Requirements

For the Degree of

Doctor of Philosophy (Civil Engineering) at

Concordia University

Montréal, Québec, Canada

February 2024

CONCORDIA UNIVERSITY
SCHOOL OF GRADUATE STUDIES

This is to certify that the thesis prepared

By: Zhaoyang Yang

Entitled: Development and Testing of a Three-dimensional Deepwater Oil Spill Model (DWOSM) to Predict the Transport and Fate of Subsea Blowouts

and submitted in partial fulfillment of the requirements for the degree of

Doctor Of Philosophy (Civil Engineering)

complies with the regulations of the University and meets the accepted standards with respect to originality and quality.

Signed by the final examining committee:

Chair
Dr. Pantcho Stoyanov

External Examiner
Dr. Yi Huang

Arm's Length Examiner
Dr. Mingyuan Chen

Examiner
Dr. Chunjiang An

Examiner
Dr. Ursula Eicker

Thesis Supervisor (s)
Dr. Zhi Chen

Dr. Kenneth Lee

Approved by

Dr. Chunjiang An Graduate Program Director

4 April 2024
Date of Defence

Dr. Mourad Debbabi Dean, Gina Cody School of Engineering and Computer Science

ABSTRACT

Development and testing of a three-dimensional deepwater oil spill model (DWOSM) to predict the transport and fate of subsea blowouts

Zhaoyang Yang, Ph.D.

Concordia University, 2024

Offshore oil exploration and production in deep water are associated with environmental risks to marine ecosystems. Oil spill models have been used for decades to help responders make informed decisions by forecasting the movement and fate of released petroleum fluids. However, few existing tools could capture the sophisticated behaviors of deep-sea spills under extreme ranges of ambient conditions. This study develops a deepwater oil spill model (DWOSM) to predict subsea blowouts' transport and weathering processes. Notably, DWOSM introduces near-field particle tracking to enable a smooth transition between near-field and far-field. It also uses thermodynamic modeling to predict the evolution of petroleum's physicochemical properties in deep water. Furthermore, a state-of-the-art stochastic simulation-based risk assessment framework is improved by embedding the DWOSM and a polycyclic aromatic hydrocarbons (PAH)-related risk evaluation index.

The application of DWOSM is demonstrated in three cases. The first study case is a hypothetical blowout in the offshore waters of East Newfoundland, Canada. The DWOSM and its each module are juxtaposed with other established models. The

verification shows that DWOSM predictions align with other model outputs. Multiple spill scenarios are implemented to investigate the impacts of weathering processes on oil fate, which reveals the vital role of natural dispersion in surface oil mitigation under windy conditions. Second, DWOSM is applied to perform a hindcast of the Deepwater Horizon (DWH) blowout. Primary model outputs are validated through field observations and relevant modeling efforts. A good performance is presented in most validation results, manifesting the reliable capability of DWOSM to simulate deep-sea spill behaviors. Last, the new model is integrated into a risk assessment framework to evaluate the subsea blowout risk in the offshore area of East Newfoundland. Various simulations corresponding to each representative met-ocean condition are conducted to yield oil spill hazard mapping. The results indicate a low-risk level around the nearshore waters of the study area, but PAH exposure can jeopardize the aquatic biota in the oil-infested region. In conclusion, this research contributes a novel modeling toolkit for predicting the complex behaviors of deep-sea blowouts and an improved stochastic simulation-based risk assessment methodology to quantify the subsea spill risk.

ACKNOWLEDGMENTS

Foremost, I would like to sincerely thank my supervisor, Prof. Zhi Chen, for his patient guidance and financial support throughout my PhD study. It is he who provides me with the valuable opportunity to study abroad, fosters my interest in scientific research, and broadens my research scope. His warm care helped my journey during the dark and chaotic times of the three-year pandemic. I have learned a lot from his patience, academic motivation, and immense knowledge. I am more than fortunate to be his student and grow in the critical four and a half years of my life.

I am grateful to my co-supervisor, a research scientist at Fisheries and Oceans Canada, Dr. Kenneth Lee, who gives me helpful suggestions in academic writing and helps me reach appropriate conclusions according to rigorous scientific analysis.

My thanks also go to all the other members of my committee, Dr. Chunjiang An, Dr. Mingyuan Chen, Dr. Ursula Eicker, and Dr. Yi Huang, for contributing their thoughtful and detailed comments on my research work.

A special acknowledgment goes to an oceanographer at NOAA, Dr. Chris Barker, who gives me invaluable instruction and effortlessly helps me solve many problems about oil spill modeling. Without his insightful and professional advice, my research would not have progressed.

I want to express my heartfelt gratitude to my parents and sister for their unwavering love and a lifetime of support and for laying the foundation for all my achievements.

Last but not least, thanks go to all my talented group fellows: Jingxin Dong,

Zunaira Asif, Lu Chen, Yinying Zhu, Mahsa Motamedi, Kamyar Soleymani, Afzal Ahmed Dar, Saeed Hashemi Halvaei, Chudi Wu, Mingxin Qu, Zhihan Wang, and Yanbin Zhuang, for their help throughout my PhD study.

TABLE OF CONTENTS

LIST OF FIGURES

LIST OF TABLES

LIST OF SYMBOLS

Section 3.2

$\vec{V}_{ajet}$	ambient current component along the plume centerline
$u_{a_t}, v_{a_t}, w_{a_t}$	ambient current velocities in XYZ directions at t time step
g'	reduced gravity
h_t	thickness of a CV at t time step
F_b	net vertical buoyant force for a single-phase plume
F_l	local densiometric Froude number
F_p	buoyant force of the dispersed oil
J_t	momentum of CV at t time step
$M_{p,i}, \rho_{p,i}$	total mass and the density of the i-th particle type in the LE
M_t	mass of CV at t time step
d_{50}	volume median diameter
d_{pipe}	orifice diameter
f_e	entrainment frequency
u'_l, u'_m, u'_n	slip velocities of a particle projected on the LNM directions
u_t, v_t, w_t	velocities of a CV in XYZ directions at t time step
α_s	shear entrainment coefficient
μ_d	oil dynamic viscosity

ρ_d	density of dispersed oil
ΔM_f	incremental mass due to forced entrainment
ΔM_s	incremental mass due to shear entrainment
ΔM_t	incremental mass of a CV at each time step
ΔU	relative jet velocity in the direction of the jet axis
Δt	length of time step
S	distance along with the plume centerline
U	exit velocity
V	magnitude of the CV velocity
$V(d)$	cumulative DSD at given diameter size d
Vi	viscosity number
We	Weber number
b	radius of the plume element
g	gravitational constant
k	buoyancy efficiency coefficient
p	spreading parameter
r	distance between the particle and the plume centerline
x, y, z	conventional Cartesian coordinates
γ	momentum amplification factor
θ	angle between the x-axis and the projection of the jet axis on the horizontal plane
ϕ	angle between jet axis and the horizontal plane

ρ, ρ_a and ρ_r	CV density, ambient density, and reference density
λ, ξ, η	coordinates of local coordinate system
$\vec{\mathrm{I}}$, $\vec{\mathrm{m}}$, $\vec{\mathrm{n}}$	three unit vectors of local coordinate system

Section 3.3

$\vec{S}$	displacement vector of a LE at a Cartesian coordinate system
$\vec{U_c}$	advective velocity vector due to the ocean current
u_s	rise velocity
$\hat{k}$	unit vector in the vertical direction
$\overrightarrow{u'}$	turbulent diffusion velocity
R_x, R_y, R_z	independent random numbers
K_h, K_z	horizontal and vertical diffusion coefficients
$\vec{u}_{sur}$	advective velocity of surface oil
$\vec{U_c}$	current velocity
$\vec{U_w}$	wind speed at the height of 10 meters over the sea
a_c, a_w	current drift factor and wind drift factor
D	transformation matrix

Section 3.4

A_s	exposed area of the slick
Q	minor axis of the ellipse
R	major axis
V_b	initial volume of an oil spill in barrel

t_m	time after spill in minute
W_k	10-meter-elevation wind speed in knot
m_i	mass of i-th PC
Y	water content of the emulsion
M_i	molar weight of i-th PC
P_i	vapor pressure of i-th PC
α_i	wind dependent mass transfer coefficient of i-th PC
W_{10}	wind speed measured at 10 m height in m/s
S_c	Schmidt number
M_w	molecular weight of water
R	universal gas constant
T	water temperature
S_{em}	emulsion stability
A_{em}	exponential of the emulsion density
B_{em}	natural logarithm of the emulsion viscosity
C_{em}	transformed resin content
Res	resin content
D_{em}	transformed asphaltene content
asph	asphaltene content
E_{em}	ratio of asphaltene content to resin content
F_{em}	exponential of A_{em}
G_{em}	exponential of E_{em}

H_{em}	natural logarithm of A_{em}
I_{em}	natural logarithm of B_{em}
J_{em}	natural logarithm of the transformed saturates
$satu$	saturate content
K_{em}	natural logarithm of C_{em}
L_{em}	natural logarithm of D_{em}
M_{em}	natural logarithm of A_{em}
t_{em}	time to emulsion
H_w	wave height
a_{em}, b_{em}	empirical coefficients varying with the emulsion type.
Y_{max}	maximum water fraction
ν_{em}	kinematic viscosity of emulsion
ν_0	initial kinematic viscosity of oil
k_{em}	empirical constant
Q_s	mass reduction in surface oil mass due to entrainment
α	entrainment coefficient
P^*	volume fraction of oil contained in oil droplets smaller than the limiting diameter
D^*	limiting diameter
T_m	mean wave period
WCC	white capping coverage
h_{em}	oil slick thickness

A_d	surface area of oil droplet
β_i	mass transfer coefficient of the i-th PC
$C_{s,i}$, $C_{a,i}$	solubility and ambient concentration for i-th PC

Section 3.5

ρ_{em}	density of emulsion
ρ_0	initial density of oil
ρ_w	density of seawater
C_1, C_2, C_3	empirical constant
f_e	mass fraction lost due to evaporation
v_{em}	kinematic viscosity of emulsion
v_0	initial kinematic viscosity of oil
K_{vis}	constant
Eo	Bond number
Re	Reynolds number
Mo	Morton number
N_D	Best number
d	equivalent spherical diameter
ρ_c, μ_c	density and dynamic viscosity of the continuous phase
$\Delta\rho_{ow}$	relative oil-water density difference
d_r	refined Willmott's dimensionless index of agreement
RI_i	integrated risk index at the *i*-th voxel
$P_{k,i}$	probability of oil occurrence at the *i*-th voxel under the

	k-th met-ocean pattern
K	total number of met-ocean patterns
S_{PAH}, S_{OL}	scaling coefficients for PAH concentration and surface oil loading at the i-th voxel under the k-th met-ocean pattern

Section 5.3

C_I	centroid displacement index
L_{OBS}	length scale of the observed spill area
C_{SS}	centroid skill score
C_T	user-selected tolerance threshold
A_I	area index
A_{PR}, A_{OBS}	predicted and observed slick area
A_{SS}	area skill score
A_{OV}	overlap between observations and predictions
A_{FN}	false negative
A_{FP}	false positive

LIST OF ACRONYMS

2D-MOE	2D Measure of Effectiveness
3D	Three-Dimensional
ADIOS	Automated Data Inquiry for Oil Spills
BAU	Business-As-Usual
CDFs	Cumulative Distribution Functions
CMEMS	Copernicus Marine Environment Monitoring Service
CV	Control Volume
DNS	Direct Numerical Simulation
DOR	Dispersant-To-Oil Ratio
DSD	Droplet Size Distribution
DWH	Deepwater Horizon
DWOSM	Deepwater Oil Spill Model
EMs	Equilibrium Models
GNOME	General NOAA Operational Modeling Environment
GOM	Gulf of Mexico
GOR	Gas-Oil Ratio
HYCOM	HYbrid Coordinate Ocean Model
IFT	Interfacial Tension
LE	Lagrangian Element
LES	Large Eddy Simulation
MAE	Mean Absolute Error

Met-ocean	Meteorology and Oceanography
MRD	Mississippi River Delta
MTs	Metric Tons
NOAA	National Oceanic and Atmospheric Administration
ODEs	Ordinary Differential Equations
OEDA	Oil Emulsion Detection Algorithm
OOSMS	Operational Oil Spill Models
OSM	Oil Spill Modeling
PAHs	Polycyclic Aromatic Hydrocarbons
PBE	Population Balance Equation
PC	Pseudo Component
PCA	Principal Component Analysis
PDMs	Population Dynamic Models
PR-EOS	Peng-Robinson Equation of State
RANS	Reynolds-Averaged Navier-Stokes
RMSE	Root Mean Squared Error
SAR	Synthetic Aperture Radar
SCAT	Shoreline Cleanup Assessment Techniques
SIMAP	Spill Impact Mapping
SSDI	Subsea Dispersant Injection
TAMOC	Texas A&M Oilspill Calculator
TCNNA	Texture-Classifying Neural Network Algorithm

TIR	Thermal Infrared Sensor
VMD	Volume Median Diameter
VOCs	Volatile Organic Compounds
WMFM	Wind-Modified Fay Model
LC_{50}	Lethal concentration 50

Chapter 1 Introduction

1.1. Background and motivation

Growing global energy demand has substantially driven oil and gas production over the last half-century. It was reported that worldwide petroleum production increased from 63,988 million barrels/day in 1980 to 95,703 in 2021 (US EIA, 2023). Meanwhile, advancements in exploration technologies (*e.g.,* the construction and maintenance of shelf and drilling platforms) allow the petroleum industry to cost-effectively access oil and gas reservoirs in deep (1,000-5,000 feet depth) and ultra-deep waters (>5,000 feet depth) (Makarynskyy, 2021). The share of global offshore oil production increased from 13% in 1990 to 30% in 2020, with particular growth of deepwater production from less than 1% before 2000 to nearly 10% in 2020 (Harris *et al.*, 2015). In recent years, many countries and oil producers have cast their attention on primitive regions and become more reliant on production from deep and ultra-deep fields to offset declines in output from shallow waters. Since 2017, over half of the American marine-derived crude has originated from ultra-deep wells (Murawski *et al.*, 2020). Mexico successfully tendered a new round of exploration licenses in 2018, which could bolster deepwater production growth in the long term (IEA, 2018). In 2019, British Petroleum claimed the discovery of two oilfields and an extra billion barrels of oil at an existing field in the Gulf of Mexico (GOM), situated in water depths of over 1,800 meters (Ron, 2019). Two years ago, the Canadian government permitted three fossil fuel firms to proceed with drilling plans in Newfoundland and Labrador offshore (CBC, 2022). More recently, the Guyana government offered fourteen blocks for tender

in Guyana's offshore region (combined shallow and deepwater areas) with an estimated reserve of over eleven billion barrels of oil equivalent (GMNR, 2022). Overall, the share of deepwater in total offshore production is expected to rise from 23% in 2022 to 30% in 2040 (IEA, 2018). Although offshore oil and gas production has matured after decades of practice, deep and ultra-deep drillings are associated with additional environmental risks compared with shallower exploit due to their complex operation and harsh conditions (*e.g.,* immense pressure and low temperature). Notwithstanding these issues, the enormous profitability of ultra-deep wells resulting from their high production rate seems appealing to the oil industry (Murawski *et al.*, 2020). Hence, escalating offshore activities unavoidably pose the potential threat of oil/gas blowouts to the ocean.

As a major environmental issue that has drawn public concern in the last decades, a few early cases of anthropogenic marine petroleum pollution date back to a century ago, such as SS Petriana with spillage of 9,529 barrels in 1903 and Thomas W. Lawson leaked 58,000 barrels in 1907 (Makarynskyy, 2021). Over the last fifty years, it is estimated that more than ten million tons of oil have been released into the global ocean, with multiple spill locations spanning from subsea blowouts to tanker accidents. Among numerous past marine oil spill incidents, the Deepwater Horizon (DWH) oil spill was the first, and to date, only ultra-deep well blowout, causing an unprecedented ecological catastrophe and inestimable socioeconomic losses (Beyer *et al.*, 2016; Murawski *et al.*, 2019). More details on the DWH blowout can be found in Section 5.1. Even though natural and anthropogenic hydrocarbon releases to the ocean occur daily, only very few

oil spills have severe or devastating effects on the marine environment and economy. For example, several million barrels of oil are annually leaked into the GOM through natural seepage from fractures in the seafloor (Board *et al.*, 2003), but never resulted in ecosystem-level damage like the DWH blowout. Nevertheless, the aftermath of oil spills with relatively small leakage can still be disastrous, especially in ecologically sensitive areas. One representative case is the Wakashio oil spill on 25 July 2020: a Japanese-owned cargo ran aground on a coral reef off southeast Mauritius. Around 1,000 tons of fuel were released into the lagoons and coastal areas, leading to 30 km of heavily contaminated shorelines (Degnarain, 2020). More than a hundred carcasses of whales and dolphins were found on the beach after the spill (Rajendran *et al.*, 2022). The quantity of oil leaked from the Wakashio is lower than that of past major spill events; however, ecological damage will be vast and enduring since it occurred in a marine-protected area laden with fragile cold-water corals and sponges (BBC, 2020). Given the consequences of oil pollution on the environment, ecosystems, and economy, it is imperative to minimize the negative impact of oil spills regardless of their size.

The prerequisite of an effective oil spill response is comprehensively understanding the transport and fate of petroleum in various environmental compartments (Yang *et al.*, 2021). Generally, marine oil spills can be categorized into three types according to their sources: surface releases (*e.g.,* tanker spills), subsea leaks (*e.g.,* pipeline cracks and natural seep), and underwater blowouts (*e.g.,* damaged blowout preventers). Deepwater blowouts are more complex than surface releases due to the extended interaction between petroleum and the water column before atmospheric exposure (Murawski *et*

al., 2020). In addition, blowouts have more significant volume fluxes and can generate highly turbulent flows than subsea leaks with weak plumes (Boufadel *et al.*, 2020a). Since oil surfacing from the deep sea will undergo the same transport and weathering processes as oil stemming from a surface spill, only the behaviors of oil and gas emitted from blowouts are depicted here to avoid unnecessary duplication. As shown in Figure 1-1, once petroleum fluids are discharged from a deepwater source, they will break into a spectrum of oil droplets and/or gas bubbles (a collective term that includes oil droplets and gas bubbles) having different sizes because the interface between the dispersed phase and ambient seawater rapidly destabilizes near the release orifice (Yapa *et al.*, 2012; Boufadel *et al.*, 2020a). In the meantime, momentum and buoyancy fluxes lift particles and entrained ambient seawater jointly as single-phase or multiphase jet/plume to higher elevations in the water column. As the plume rises, its momentum and buoyancy are gradually depleted due to crossflows and the entrainment of ambient fluids, which may form intrusion layers of enhanced hydrocarbon content at a neutral buoyancy level. Large oil droplets and gas bubbles may escape from the plume and ascend to the sea surface along different pathways, whereas tiny bubbles and light components of oil droplets may dissolve into ambient seawater. Unlike dispersed oil, gas may be converted to crystalline solids named gas hydrates under high pressure and low temperature. Eventually, droplets reaching the surface may form slicks and are moved by advection and diffusion under the combined influences of currents, winds, and waves. A series of transformation processes will concurrently change the physical and chemical properties of the oil over a broad range of timescales (collectively termed

"weathering"), such as evaporation, emulsification, and spreading (Tarr *et al.*, 2016). In turn, the weathering rate is highly influenced by the variation in oil properties. More details of petroleum weathering processes are introduced in section 2.4.

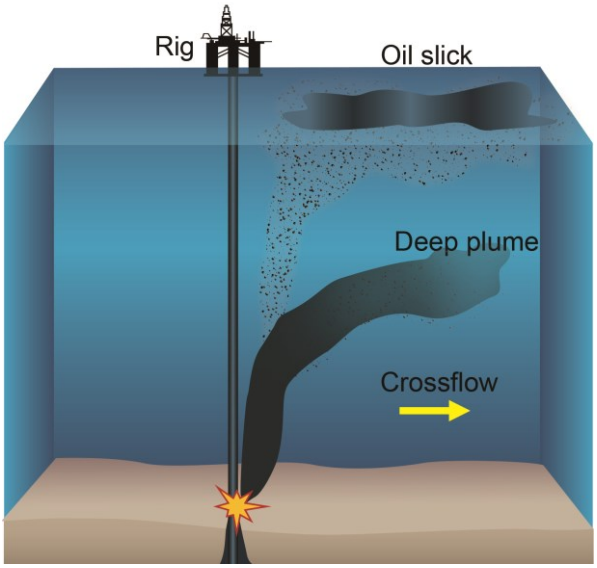

Figure 1-1 Schematic diagram of a deepwater blowout.

After an oil spill incident, knowing where oil is likely to move, what resources will be impacted, and the level of damage that will probably be caused to communities can provide invaluable information for decision-making regarding oil spill preparedness and response (Nelson *et al.*, 2015). To predict the fate and transport of oil spills, researchers developed numerous comprehensive and easy-to-use toolkits, ranging from simple oil fate models to sophisticated three-dimensional (3D) numerical models (Yang *et al.*, 2021). Nevertheless, oil spills are a complex topic involving several scientific specialties, environmental conditions, and extensive dimensional scales, especially for deepwater blowouts with additional complexity (Murawski *et al.*, 2020). When simulating subsea blowouts, oil spill modeling is usually divided into two distinct

domains: near-field with spatiotemporal extent of the order of hours and a few hundred meters above the wellhead, and far-field up to several months and kilometers away from the source (Riazi, 2021). Near-field modeling aims to simulate near-field plume dynamics (*e.g.,* spatial coverage and momentum); far-field modeling focuses on tracking the evolution of particles that exit from the plume region, such as composition and location (Murawski *et al.*, 2020). Some oil spill models only focus on near-field or far-field modeling, which requires coupling with other components to simulate deep-sea oil/gas blowouts. Though a few comprehensive models nearly touch upon every aspect of oil spill modeling (OSM) (*e.g.,* plume model, droplet size distribution (DSD) model, particle tracking, weathering algorithms), they are still not all-inclusive or oversimplify some critical spill behaviors. For example, regarding subsurface oil tracking, due consideration should be given to the evolution of particle sizes and properties owing to fate processes and in situ conditions (Ainsworth *et al.*, 2021). Furthermore, it is seen that the coupling of near- and far-field modeling with spatiotemporal dynamics of oil and water properties needs further investigation. Particularly for supporting regulatory approvals to future offshore oil and gas exploration/production in field conditions, such modeling tools should be examined at sea to develop protocols for environmental impact assessments. Nowadays, what makes the situation more concerning is that ultra-deep wells in the GOM expand to depths nearly twice that of DWH (Murawski *et al.*, 2019). Hence, developing an operational oil spill forecasting system with robust integration of state-of-the-art numerical models becomes an urgent task to tackle potential deepwater blowouts.

1.2. Research objectives

The primary goal of this study is to develop and evaluate a comprehensive deepwater oil spill model (DWOSM) in support of the response to deep-sea blowouts. Specifically, a hypothetical case and an actual past blowout accident are used as the study cases to verify the DWOSM. The specific objectives in line with the primary goal are presented as follows:

1) To develop a 3D operational oil/gas blowout forecasting system by coupling multiple modeling components, including a two-phase flash calculation system, DSD model, jet/plume model, near-field and far-field particle tracking models, and fate algorithms.
2) To assess the applicability of the DWOSM in a hypothetical oil blowout case occurring at eastern Canadian offshore waters by systematically comparing each module and other well-established models.
3) To examine the validity of the DWOSM in a real-world case (*i.e.*, DWH blowout) by comparing the hindcast results with the observation.
4) To combine the deterministic model and the Monte Carlo method for quantitatively conducting an environmental risk assessment of spill-related polycyclic aromatic hydrocarbons (PAHs) in offshore waters of eastern Canada. A deep-sea blowout risk map is also generated based on a new risk assessment framework.

1.3. Outline

This doctoral dissertation contains three research chapters (*i.e.*, 2-6) and concludes in Chapter 7. The detailed research organization is shown in Figure 1-2.

Chapter 1 gives background information on the current status of worldwide deepwater oil production. Some past major oil spills and the behaviors of deep-sea blowouts are also briefed. Finally, we state the present problems with deepwater OSM and specify the research objectives.

Chapter 2 thoroughly reviews the studies regarding most aspects of deepwater OSM. The pros and cons of the commonly used methods in each direction are summarized and discussed, which is conducive to finding the optimal approaches for this study.

Chapter 3 systemically describes the methodology for developing an operational deepwater oil/gas spill forecast system. Each modeling component is introduced in this chapter, including flash calculations, the DSD model, near- and far-field particle tracking models, and fate algorithms. This chapter also presents the integration of those components, the numerical method, and a stochastic simulation-based risk assessment approach.

Chapter 4 depicts a case study of applying the DWOSM to predict a hypothetical blowout in eastern Canadian waters. Multiple well-established oil spill models, such as Spill Impact Mapping (SIMAP) and General NOAA Operational Modeling Environment (GNOME), are used to comprehensively compare with the DWOSM in this case, which aims to evaluate the applicability and validity of this newly developed model. Furthermore, the impacts of serval weathering processes on the oil budget are also numerically investigated in various simulation scenarios.

Chapter 5 presents a real-world application of the DWOSM to the DWH incident.

DWOSM is used to provide the hindcast of transport and fate during the initial stage of the DWH spill. Its model performance in multiple outputs is validated by a series of comparisons, which mainly rely on remote sensing-based data, previous modeling efforts, and field measurements.

Chapter 6 describes a PAH-related risk assessment based on integrating data mining techniques and the DWOSM. An oil spill risk mapping is eventually yielded for the offshore region of East Newfoundland, Canada. The effectiveness of subsea dispersant injection (SSDI) on spill mitigation is also numerically examined and discussed.

Chapter 7 summarizes the conclusions and main contributions and proposes several recommendations for the following research.

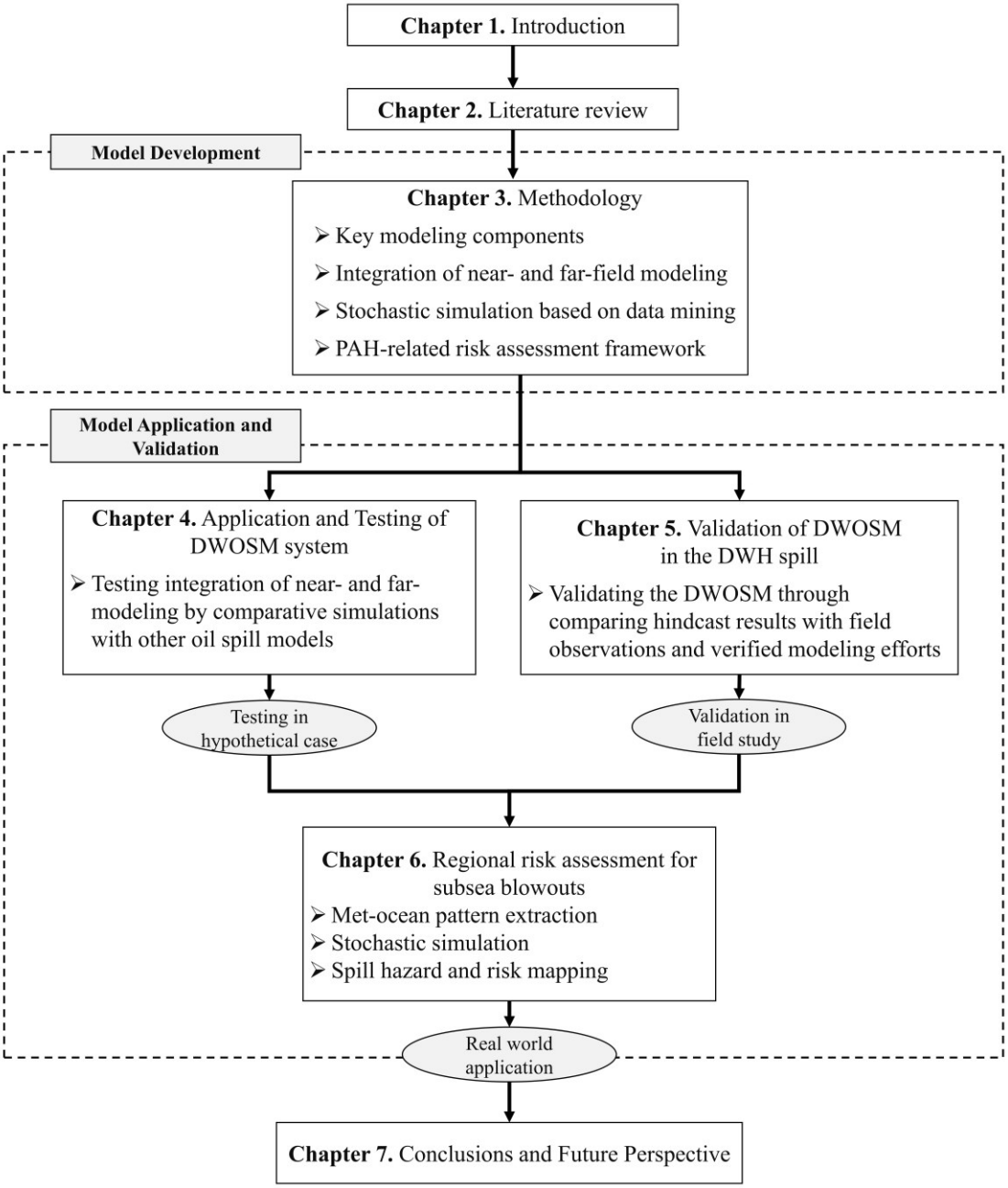

Figure 1-2 Thesis organization.

Chapter 2 Literature Review

2.1. Droplet size distribution models

The size distribution of particles forming near the release point of a deep-sea blowout can significantly impact the transport and fate of petroleum fluids in the ocean, particularly for surfacing time and location in tandem with the rate of dissolution and biodegradation (Murawski *et al.*, 2020). Therefore, the prediction performance of deepwater OSM largely depends on the accuracy of the DSD model. In contrast to numerous DSD-related studies since the DWH, the importance of DSD calculations did not receive sufficient attention from the early oil spill models (Nissanka and Yapa, 2018). It is noteworthy that oil droplets can be generated both in underwater jets/plumes and under breaking wave conditions at the sea surface. Given that most spill response technologies focus on floating and stranded oil and are incapable of tackling submerged oil, the operational response is less concerned with whether oil is sedimented or degraded after the dispersion. Here, we only survey existing DSD models tailored for oil/gas blowouts because the droplet size of wave-entrained oil mainly influences the follow-up propagation and fate of submerged oil, even though these droplets may resurface and form a secondary slick.

The approaches for calculating oil/gas DSDs resulting from subsurface releases can be categorized as equilibrium models (EMs) and population dynamic models (PDMs) (Socolofsky *et al.*, 2015). EMs predict a characteristic quasi-stationary droplet size (typically the volume median diameter VMD) at the end of the primary breakup regime based on semi-empirical relations (Johansen *et al.*, 2003 and 2013; Li *et al.*, 2017).

They cannot generate the DSD from the predicted VMD without the assistance of a predefined statistical distribution (*e.g.,* Rosin-Rammler and log-normal distributions). All the EMs originate from the seminal work by Hinze (1955) that correlates the VMD with turbulent energy and interfacial tension under stationary conditions. Johansen (2003) proposed a method to calculate the maximum oil droplet size at exit conditions of large-volume jets by analogy with droplet splitting in turbulent pipe flow. This study introduced the Weber number into the DSD calculation and has been widely adopted by the follow-up EMs. Hereafter, Boxall *et al.* (2012) developed a function of Reynolds and Weber numbers to predict droplets of water-in-oil emulsions under turbulent flow. Johansen *et al.* (2013) further improved EM by considering the viscosity effect, *i.e.*, the breakup with smaller viscous numbers is governed by Weber number scaling, while Reynolds number scaling is applicable for larger viscous numbers. This modified approach is one of the most recognized EMs and has been adopted by various operational oil spill models (OOSMs) (Sim *et al.*, 2015; Spaulding *et al.*, 2017; Socolofsky *et al.*, 2022). Li *et al.* (2017) proposed a unified droplet size model with a combination of Weber and Ohnesorge numbers, gaining an advantage over other EMs, *i.e.*, it applies to both underwater blowouts and surface wave entrainment by adjusting model coefficients.

PDMs build on a population balance equation (PBE) to emulate two competing processes of breakup and coalescence, which provides the temporal evolution of the size distribution of oil droplets and gas bubbles in turbulent flows (Bandara and Yapa, 2011; Zhao *et al.*, 2014a, b). This physics-based method has its roots in earlier PBE

developed for computing DSD in turbulent fluid columns (Nissanka and Yapa, 2018). Bandara and Yapa (2011) adapted PBE to predict the DSD of particles released from deepwater blowouts for the first time. Zhao *et al.* (2014a) used a discrete form of PBE to develop a DSD model (VDROP). Subsequently, Zhao *et al.* (2014b) combined it with an empirical jet model as VDROP-J to predict oil/gas DSDs at different times and downstream distances from the exit. Likewise, Nissanka and Yapa (2016) integrated Oildroplets, a PBE-based DSD model from their previous work, with a Lagrangian integral jet and plume model.

Compared to EMs derived from empirical relations, physics-based PDMs seem more theoretically plausible because of their ability to simulate particle dynamics within the breakup region of multiphase jets/plumes (Cooper *et al.*, 2021). PDMs also have the advantage over EMs of directly providing evolving DSD along the jet/plume trajectory without choosing a heuristic distribution. Nevertheless, a relatively heavier computational burden and additional specifications about ambient turbulence limit the application of PDMs to field conditions (Makarynskyy, 2021). The uses of EMs beyond the tested ranges are doubtful as their coefficients are obtained from given experiments. Yet, they have been well-validated through numerous laboratory experiments covering extensive release conditions (Nissanka and Yapa, 2018). Considering their practicability and simplicity, EMs are suitable for rapidly estimating DSD during a spill incident and have become the most popular choice in current oil spill models.

2.2. Buoyant plume models

Similar to methods of DSD prediction, there are two widely used techniques for

simulating buoyant plume dynamics at the field scale (Murawski *et al.*, 2020). The first method is 3D computational fluid dynamics models that numerically solve a particular form of Navier-Stokes equations, which can be further grouped into three types based on their scales and grids: Reynolds-averaged Navier-Stokes (RANS) model, large eddy simulation (LES), and direct numerical simulation (DNS). Compared with the other two methods, LES is a promising approach for modeling practical multiphase flow scenarios as it combines the advantages of the RANS and DNS (Boufadel *et al.*, 2020a). Despite improvement in understanding the near-field plume behaviors since DWH, for instance, Daskiran *et al.* (2021) captured oil DSD and jet dynamics similar to experiment observation through LES, it is inherently less capable of characterizing flows requiring parameterization of sub-grid-scale processes (*e.g.,* coalescence and breakup) (Boufadel *et al.*, 2021). Furthermore, computational fluid dynamics modeling is always computationally costly; thus, most comprehensive toolkits designed to guide operational oil spill response rely on integral models (Murawski *et al.*, 2020).

Based on the assumption that the multiphase plume is of self-similarity, integral models resolve the cross-sectional averaged flow quantities (*e.g.,* volume, momentum, and buoyancy) along the plume pathway. In the groundbreaking work of Morton *et al.* (1956), the concept of a buoyant plume and its governing equations were proposed and became the fundamental of follow-up studies on integral models. To date, two major integral models are available to predict the dispersed phase separation and the intrusion layer formation, *i.e.*, double-plume models and a Lagrangian approach. The former uses an Eulerian framework to solve for an upward-rising inner plume and a separate,

annular outer plume in still waters. The round bubble plume model proposed by Milgram (1983) is commonly adopted to simulate the inner plume, while various studies use different algorithms for computing flux exchange between the inner and outer plumes. This approach can effectively predict multiple sequences of intrusion layers but is only appropriate in a quiescent environment, as crossflows will asymmetrize the outer plume to invalidate its equations (Dissanayake *et al.*, 2018). The latter establishes a Lagrangian framework for modeling the behaviors of the inclined buoyant plume in the presence of crossflow. It is prevalently taken as the near-field modeling approach among subsea oil spill models, such as BLOOSM and Texas A&M Oilspill Calculator (TAMOC). Lee and Cheung (1990) developed the earliest Lagrangian jet/plume model for underwater blowouts and introduced control volume (CV) analysis for blowout simulations. Under such a scheme, a conceptual volume consisting of oil, gas, and entrained water is treated as a generalized entity analogous to an independent cylindrical, cross-sectional plume segment (Sim, 2015). At each step, the property change of the CV is driven by the entrainment of the ambient water and the crossflow, which may decelerate the jet motion and expand the CV volume until momentum and buoyancy vanish. Recent improvements to integral models include the physicochemical and thermodynamic equations to handle oil-gas mixtures and the particle tracking algorithm to quantify the contributing buoyancy of dispersed phases to the plume (Dissanayake *et al.*, 2018; Boufadel *et al.*, 2020a; Wang *et al.*, 2022). It is worth noting that both integral models are only applied to solve the steady-state solution.

2.3. Transport models

Spill trajectory forecast is one of the most decisive problems for oil spill preparedness and response since decision-makers need to prioritize protecting sensitive resources and shorelines (Yang *et al.*, 2023). As a result, the module aiming for oil spill transport simulation becomes a critical component of OOSMs. In addition to a few new attempts, like applying the lattice Boltzmann method in oil spill trajectory modeling (Maslo *et al.*, 2014), most studies adopt the Eulerian or Lagrangian approaches (Keramea *et al.*, 2021; Yang *et al.*, 2021). By boiling down the mathematics of oil transport to solving the advection-diffusion equation, the Eulerian method treats the particle phase as a continuum and simulates temporospatial variations of oceanographic fields (Makarynskyy, 2021). It mainly benefits from the three features: a) available to add empirical formulas describing the local changes/interactions of the oil with the environment; b) configuring a high-resolution mesh may capture more realistic details (*e.g.,* coastlines and sea ice); c) the ability to reflect the impact of spill volume changes on the diffusion area of oil spills. In practice, this method is less effective than the Lagrangian representation in oil transport simulation because it requires generating numerical grids of the studied domain. Particularly for 3D partial differential equations, it is computationally intensive as the equation must be solved at every grid point regardless of whether oil exists.

The Lagrangian method discretizes oil as a finite number of particles assigned with an initial location and mass to simulate the trajectories of each particle independently. This technique may effectively avoid numerical diffusion in an Eulerian framework and

has a lower computational cost since it only solves the system of ordinary differential equations (ODEs). Furthermore, a random walk scheme is often coupled with a Lagrangian framework to simulate oil displacement due to turbulent diffusion. Most spill models face common problems when they implement the Lagrangian method: a) lack the capability of EMs to mirror the impact of spill volume changes on the diffusion area; b) no criteria for the selection of particle number, while insufficient particles cannot accurately characterize horizontal oil dispersion and excessive particles will increase the unnecessary computational burden.

Regarding subsea blowout releases, the algorithms for particle rise velocity are additionally required under a Lagrangian scheme. The commonly used methods in spill models include the two-equation approach (Zheng and Yapa, 2000) and the correlation formulations for fluid particles (Clift *et al.*, 2005). The former adopts Stokes' law to calculate the terminal velocity of small droplets (less than 1 mm) and integrate the drag coefficient for large droplets (typically greater than 10 mm). Some studies use interpolation for intermediate droplets to smooth the gap, while others apply the same methods with small or large droplets. Compared to the former, correlations offered by Clift *et al.* (2005) not only consider the oil properties and ambient conditions but also define the rise velocity under different regimes of particle shapes.

2.4. Weathering algorithms

Understanding the impacts of weathering processes on oil mass loss and characteristics after a spill can strongly support decision-making about what cleanup options should apply, as each countermeasure has its applicable conditions. For

example, aerial spraying of oil dispersant chemicals will miss the operational window of opportunity when the slick becomes too viscous due to weathering. Many modeling approaches tailored for individual fate processes are reviewed in the following sections.

2.4.1. Spreading

When oil appears on the sea surface, horizontal expansion of slicks immediately occurs under the gravitational action regardless of the presence of winds and currents. This process plays a crucial role in the early stage of weathering from two dimensions: the thickness of a slick becomes thinner, and the oil-contaminated area expands (Fingas, 2017). Most oil spill models treat spreading as a driver of other weathering processes (*e.g.,* evaporation and dispersion), which focus more on reasonably estimating the exposed surface area caused by spreading than itself.

To date, the most widely accepted theory is still based on Fay's regimes that divide the spreading into three separate phases: gravity-inertial, gravity-viscous, and interfacial tension (Simecek-Beatty and Lehr, 2017). The first phase represents that the oil extends laterally under the balance between the driving force of gravity and the retarding force from inertia. As it is transient (typically lasts for a few minutes) compared to the timescale of weathering, the area at the end of this stage acts as the initial condition of gravity-viscous spreading for practical purposes. A slick can be assumed to be an elliptical formation with the central axis oriented toward the downwind. In the second phase, the viscous shear of the water underlying the surface layer substitutes inertia as the retarding force. The last phase begins when the effect of gravity on the oil attenuates, and the interfacial tension continues to spread the oil. This

stage is often ignored because it only occurs when a slick becomes sheen (thinner than 0.1 mm) and reaches terminal thickness (the minimum thickness of an oil slick). Notwithstanding that Fay spreading can capture the physics of an oil film on a quiescent water surface, its formulas underperformed in many reported cases due to the elongating slick (Simecek-Beatty and Lehr, 2017). To correct the underestimation for a slick area of an elongating oil film, Lehr *et al.* (1984) developed a wind-modified Fay model (WMFM) by separately calculating the major axis along the downwind direction and the minor axis. Simecek-Beatty and Lehr (2017) further modified the WMFM to simulate the thickness and length of oiled windrows by incorporating Langmuir circulation models and correcting surface area due to Langmuir effects.

Apart from the Fay-type formulation, Geng *et al.* (2016) investigated the effect of waves on the propagation of oil droplets at sea. It suggested that Lagrangian transport models could overestimate the turbulent diffusion of surface oil. In sum, most spreading algorithms emphasize approximating the surface area and thickness of a slick depending on oil properties and sea state. The research regarding the impact of wave action and Langmuir circulation on oil spreading is insufficient because the data required by rigorous solutions to those problems are less obtainable in the emergency spill response (Keramea *et al.*, 2021). Another issue is the uncertainty brought by the Lagrangian element (LE) number choice. The thickness is usually defined by the ratio of oil volume to surface area, while using different particle numbers may lead to discrepancies in the predicted mass of each LE.

2.4.2. Evaporation

As the most critical removal mechanism for surface oil, evaporation usually dominates the volumetric reduction of slicks during the first few days after a spill, accounting for a 20% to 40% loss of oil mass corresponding to volatile hydrocarbon components (Afenyo *et al.*, 2016). Lighter compounds enter the atmosphere, while heavier components remain at sea with higher density and viscosity. Presently, three representative methods are available to simulate the evaporation of hydrocarbon mixtures: the pseudo component (PC) evaporation model, empirical formulas, and the analytical approach (Fingas, 2017). As a widely used method in earlier oil evaporative works, the analytical approach treated oil as a single component to estimate its evaporation rate based on a dimensionless group, *i.e.*, evaporative exposure that depends on time, wind speed, and spill area (Stiver and Mackay, 1984). Such an assumption is incompatible with the fact that the chemical compounds of the oil evaporate disproportionately. Taking advantage of its reliability and flexibility, the PC evaporation model currently replaces the analytical approach in the mainstream OOSMs. It assumes oil as a mixture of non-interacting components defined by distillation curve cuts, allowing each PC to evaporate disproportionately and independently (Sim *et al.*, 2015). Vapor pressure and mass transfer coefficient are used to calculate the evaporation rate for individual components. The evaporative loss of a hydrocarbon mixture is the sum of evaporated mass or volume from each PC. Distinct from the two physics-based methods above, Fingas (2017) developed many statistical correlations from experimental data to predict the evaporative loss for specific oil types.

Instead of being air-boundary layer regulated, Fingas states that oil evaporates differently from water and is controlled by diffusion through the mass. In Fingas's empirical formulas, evaporative fraction loss of petroleum fluids is time-dependent and relies on oil type and water temperature. Despite substantial equations given by Fingas (2017), those relations correspond to certain oil types and are less valid to predict any petroleum beyond the tested categories. Their application to operational spill response is also questionable because laboratory-derived correlations have not been extensively verified in field conditions. Overall, compared with approaches that only provide the big picture of oil evaporation, the PC model is still the most widely recognized solution to predict the evaporative loss of hydrocarbon since it involves the more detailed chemical composition of the oil.

2.4.3. Natural dispersion

As a second major weathering process, natural dispersion (wave entrainment) can determine how long oil will remain on the sea surface. It occurs when wave action or turbulence creates tiny oil droplets and transfers them into the upper water column (Makarynskyy, 2021). Microdroplets with different definitions, ranging from <20 μm in Fingas (2017) to <100 μm in Boufadel *et al.* (2020b), are somewhat stable in water and will last for more extended periods. Larger droplets tend to surface rapidly and will not stay in the water column for over seconds. The entrainment rate primarily depends on the amount of wave energy and oil properties (*e.g.,* viscosity and interfacial tension). Given the varying sea states and oil types, wave entrainment can either be insignificant to oil mass balance (*e.g.,* heavy crude under calm waters) or the dominant removal

mechanism from surface oil (*e.g.,* light oil during storm events).

In the modeling of natural dispersion, the entrainment rate is usually explicitly or implicitly coupled to oil DSD (Makarynskyy, 2020). Delvigne and Sweeney (1988) conducted an experimental investigation on oil droplet formation by breaking waves, which is still the basis for modeling natural dispersion in most studies (Johansen *et al.*, 2015). This study developed an empirical formulation of the entrainment rate as a function of the dissipated wave energy per unit area, white capping coverage, oil viscosity, droplet size, etc. The original work did not give the total entrainment rate, which requires performing the integration over droplet size intervals. This experimentally derived method has several issues, particularly the overestimation of the dispersion rate. Fingas (2017) substituted the upper limit of droplet diameter with 20 μm, allowing the entrained oil to be stable in the water rather than surfacing immediately. Some corrections were also made regarding the oil constant and the threshold of the onset of breaking waves. Other studies simulated the rate of natural dispersion based on the explicit prediction of entrained oil DSD generated by breaking waves. Johansen *et al.* (2015) developed a semi-empirical DSD model by introducing Weber and Reynolds numbers and formulated the first-order decay equation as an entrainment rate. Zeinstra-Helfrich *et al.* (2017) modeled the consequence of natural and chemical dispersion for the size of surface oil over time, using a function of wind speed, oil properties, and dispersant application. This work also combined slick properties and environmental conditions into a newly defined indicator ("dispersibility factor"), which can be used to evaluate the favorability of natural dispersion and

chemical dispersants. As mentioned in section 2.1, the model proposed by Li *et al.* (2017) also applies to the sea with breaking waves. Although it stated that the DSD prediction agreed with the experimental data, the entrainment rates predicted from new models are even significantly faster than that of Delvigne and Sweeney's method under high-speed wind conditions. Hence, more field observations are expected to be used to validate recently developed dispersion algorithms, especially at open sea with intensive wave actions.

2.4.4. Emulsification

Wave action can disperse water droplets into slicks, forming water-in-oil emulsions (sometimes called "mousse") with distinct properties from non-emulsified oil. This process can considerably increase the volume and properties (*e.g.,* viscosity and density) of floating oil, thereby decelerating many critical weathering processes (*e.g.,* evaporation and dispersion) by orders of magnitude. Thus, emulsification significantly impacts the effectiveness of spill response technologies on surface oil removal. The most widely used modeling approach for emulsification originates from the first-order rate law model developed by Mackay *et al.* (1980), which assumed that the water fraction of the emulsified oil monotonically increases with wind speed to a specific threshold. Lehr *et al.* (2002) modified this work by introducing the effect of viscosity on the water fraction of emulsion. De-emulsification sometimes occurs when emulsions have lower stability. Xie *et al.* (2007) added a term to consider emulsion water loss for unstable and meso-stable emulsions. Except for the studies on forecasting emulsification rate, Fingas (2017) made noticeable progress in classifying emulsions

and their time to formation. According to oil properties and chemical constituents, the stability index is proposed to group the water-in-oil into four types: stable, mesostable, entrained, and unstable. Nonetheless, an emulsification model based on environmental conditions and oil properties is still anticipated, as the emulsion formation mechanism is poorly understood.

2.4.5. Dissolution

Water-soluble hydrocarbons can dissolve into the surrounding fluid, primarily controlled by the solubility of those compounds and the surface area of the oil-water interface (Tarr *et al.*, 2016). For most surface releases, the dissolution is insignificant to the mass balance of an oil spill compared with other weathering processes, as only a small amount of oil components (*e.g.,* lower-molecular-weight aromatics) might be lost to the water. Conversely, this process can be critical to deep-sea blowouts because deepwater-released oils are usually "live oils" containing significant amounts of dissolved gases (*e.g.,* methane and ethane) (Murawski *et al.*, 2020). The larger surface-area-to-volume ratio of fluid particles is another factor that makes dissolution more impactful to the fate of deep-sea blowouts than that of surface spills. Despite barely measurable mass variation caused by dissolution for "dead oils" (oil that does not contain dissolved gases), soluble aromatic compounds are particularly toxic to aquatic life and should not be ignored in environmental impact assessment. Current dissolution models are similarly dependent on the calculation of the mass transfer rate. Cohen *et al.* (1980) used an oil-water partition coefficient and the water-phase transfer velocity to estimate the transfer rate of the soluble oil component. Zheng and Yapa (2002)

simulated the dissolution rate for a gas bubble using the bubble surface area, ambient concentration of solute, solubility, and mass transfer coefficient. In general, the differences among dissolution models mainly stem from the different methods used to compute mass transfer coefficients and solubility.

2.4.6. Biodegradation

Marine microbial communities can decompose petroleum hydrocarbons into simpler organic compounds, regarded as one of the most significant long-term natural processes to mitigate the environmental impact of oil spills. Since microbes only degrade hydrocarbons at the water-oil interface, diluted oil in the water column has a shorter half-life of a few orders of magnitude than floating or stranded oils (Prince *et al.*, 2017; Makarynskyy, 2021). In addition to the water-oil interface area, influencing factors to the biodegradation rate include ambient temperature, nutrients (*e.g.,* nitrogen and phosphorus) and oxygen availability, the nature of hydrocarbons, microbial population, and the degree of weathering (Fingas, 2017; Keramea *et al.*, 2021). As biodegradation is typically considered less critical to the short-term fate of spilled oil, most OOSMs ignore it or simplify it as a first-order decay process primarily depending on oil composition (Dissanayake *et al.*, 2018; Galagan *et al.*, 2018; Keramea *et al.*, 2021). Component-specific decay coefficients are adopted to represent the biodegradation rate of each group of petroleum compounds. A few studies endeavor to incorporate a more realistic description of biodegradation kinetics into oil spill models, such as the surface area of the oil-water interface (Thrift-Viveros *et al.*, 2015), lag phase for the onset of biodegradation (Prince *et al.*, 2017), and the Monod kinetics

(Spanoudaki, 2016). Overall, the first-order decay equation is the only widely accepted approach for modeling hydrocarbon biodegradation in the maritime environment.

2.4.7. Oil-shoreline interactions

Compared to well-established modeling approaches of oil transport and fate in the marine environment, methods available to predict the behaviors and fate of spilled oil on seashores are limited because oil-shoreline interactions are poorly understood (Yang *et al.*, 2021). Previous studies are primarily limited to focusing on individual processes of natural attenuation and translocation; only a few have attempted to characterize oil-shoreline interactions (sometimes termed beaching) comprehensively. For instance, multiple oil-shoreline interactions are considered in the COZOIL model in the simulation of natural oil removal onshore for the first time; however, some essential processes to the mass balance of beached oil, such as biodegradation, are not included (Reed *et al.*, 1989). A fate model is developed to investigate the mechanisms by which oil spills naturally dissipate from a beach by storms, tides, and weathering for stranded oil, which is based on the experiments of subsurface oiling conditions on coarse sediment (Humphrey, 1993). Its drawbacks include the insufficient predictive ability for how long stranded oil remains on the beach and limited applicability to other shoreline types than coarse pebble beaches (Humphrey *et al.*, 1992). More recently, Geng *et al.* (2015) coupled the Monod kinetic model with a groundwater model to simulate the subsurface aerobic biodegradation of low-solubility hydrocarbons in a coastal environment. Although relevant fieldwork and applications have been conducted, excessive input parameters constrain its practicability in operational

response. Half-life values and oil-holding capacity are two methods commonly incorporated in OOSMs, which are simple and practical to estimate oil-shoreline interactions empirically. The former describes the adhesiveness of the oil to the different beach types; the latter delineates the maximum accumulation of oil stranded onshore (Etkin *et al.*, 2008; Zelenke *et al.*, 2012; Samaras *et al.*, 2014).

2.5. State-of-the-art of OOSMs

Over the past few decades, three generations of oil spill models have been developed to deepen the understanding of oil behaviors and impacts (Berry *et al.*, 2012; Nelson and Grubesic, 2019). The first generation comprises empirical transport models with simple fate algorithms; the second consists of two-dimensional hydrodynamics and fate algorithms; and the latest is 3D multi-component subsea blowout models with a fate module and a transport module (Berry *et al.*, 2012). Both modules are the core parts of the most developed oil spill models: the former aims to simulate the movement of dispersed oil; the latter is tailored to estimate various weathering processes (Yang *et al.*, 2021). Table 2-1 summarizes some state-of-the-art oil spill models and their features. Despite some overlap in terms of functionality, these modeling toolkits can be categorized into two groups pursuant to their aimed marine spill incidents: subsea oil/gas blowouts (TAMOC, SIMAP, and BLOOSM) and surface oil release (GNOME, MEDSLIK-II, and OpenDrift). The major difference between the two model types is whether to include a near-field model for simulating the jet/plume behavior. Unlike most blowout models that characterize the buoyant plume by a stack of conceptual volumes of mixed oil, gas, and entrained water, TAMOC has a unique capability that

tracks fluid particles within the main plume to account for the contributing buoyancy of dispersed phases to the plume. For surface spill models, the evident discrepancy is the choice of weathering processes in the fate module. Several processes (*e.g.,* dissolution, biodegradation, and sedimentation) are only crucial to the long-term spill mass balance and are thus usually neglected by OOSMs for short-term forecasting. Compared to treating oil/gas compounds as a single entity, the PC approach is more accepted in fate modeling due to its flexibility and realistic representation, especially for evaporation and dissolution. Trajectory simulation methods adopted by most operational models are almost the same, but SIMAP additionally considers the wind-induced drift angle when Ekman flow is not involved in current data.

Table 2-1 A summary of some widely used OOSMs and their features

Model names	Transport module	Weathering module							Programming languages
		Spreading	Evaporation	Dispersion	Emulsification	Dissolution	Biodegradation	Sedimentation	
TAMOC	Lagrangian	-	-	-	-	✓	✓	-	Python, Fortran
GNOME	Lagrangian	✓	✓	✓	✓	✓	✓	✓	Python, C, C++
SIMAP	Lagrangian	✓	✓	✓	✓	✓	✓	✓	Java, C++
BLOOSM	Lagrangian	✓	✓	✓	✓	✓	-	-	C++
MEDSLIK-II	Lagrangian	✓	✓	✓	✓	-	-	-	Fortran, Python
OpenDrift	Lagrangian, Eulerian	✓	✓	✓	✓	-	-	-	Python

Particle evolution	Gas component	DSD model	Buoyant plume model	Near-field particle tracking	Subsurface model	Surface model	Beaching	Oil database	Pseudo components	Coriolis effect
multi-properties	✓	✓	✓	✓	✓	-	-	-	✓	-
✓	-	✓	-	-	✓	✓	✓	✓	✓	-
✓	✓	✓	✓	-	✓	✓	✓	-	✓	✓
✓	✓	✓	✓	-	✓	✓	✓	✓	✓	-
-	-	-	-	-	-	✓	✓	✓	-	-
✓	-	✓	-	-	✓	✓	✓	✓	-	-

2.6. Oil spill risk assessment

As a practical approach to help minimize the negative impact of hydrocarbon pollution, oil spill risk assessment aims to quantitatively estimate the potential harm of released petroleum on the marine ecosystem. Regardless of the difference in definitions of oil spill risk, most emphasize a function of the likelihood of incident occurrence and the severity of environmental and socioeconomic impacts led by corresponding spills for a particular region (Nelson and Grubesic, 2018; Chiri *et al.*, 2020). The most commonly used method of oil spill risk assessments is based on stochastic or probabilistic modeling (*i.e.,* the combination of deterministic simulations), which builds numerous hypothetical spill scenarios composed of various features of spill incidents, such as release location, oil type, and their corresponding likelihood. Meteorology and oceanography (met-ocean) variables, particularly for wind and currents, are the most critical contributing factors amidst the inputs of oil spill models. Spilled oil is advected by subsurface crossflows and surface winds and currents; its rates of weathering processes (*e.g.,* evaporation and dispersion) are also highly affected by wind speed and wave mixing. Thus, stochastic OSM needs to be implemented under specific met-ocean conditions that can comprehensively characterize the historical variability of maritime environments in areas of interest. Such a methodology postulates that past regional met-ocean conditions statistically resemble future atmospheric and oceanic patterns (Liubartseva *et al.*, 2021). Most previous stochastic simulation-based spill risk assessments randomly selected the environmental background data from a specific period and the number of model runs (Al Shami *et al.*, 2017; Guo, 2017; Nelson and Grubesic, 2017; Niu *et al.*, 2017; French-McCay *et al.*, 2017 and 2018; Amir-Heidari *et al.*, 2019; Amir-Heidari and Raie, 2019; Wang *et al.*, 2020;

Liubartseva *et al.*, 2021; Zhu *et al.*, 2021). However, they did not address a persistent problem in stochastic modeling: specifically, how many times or scenarios should run? Intuitively, the credibility of simulation output increases with more runs, but related computational resources and time can be unaffordable for emergency spill response.

Another common issue is the interpretability of met-ocean pattern choice, *i.e.,* can randomly selected current and wind datasets represent local atmospheric and oceanographic variabilities? Some studies above take environmental data during a limited period, like a few weeks, as the input of velocity fields. Since the chosen dataset may insufficiently capture the temporospatial variability of regional met-ocean patterns, whether those assessment results are instructive of future strategic response operations in areas of concern is doubtful. While using the long-term dataset as the input data is a straightforward solution to OSM, it means coping with a tremendous amount of data and computationally demanding numerical simulations, making stochastic simulation-based risk assessment extremely time-consuming. To tackle this challenge, Chiri *et al.* (2020) introduced statistical data mining techniques in 3D stochastic modeling for subsea oil blowouts. Through dimensionality reduction and pattern extraction, the feasibility and efficiency of stochastic simulation are significantly improved by minimizing its computational costs. This method is limited by only using a binary indicator to express the presence or absence of oil, which might be inadequate to delineate the spill hazard in the region.

2.7. Summary

This chapter presents an extensive overview of widely used approaches in almost every aspect of OSM, OOSMs, and spill risk assessment methods. Despite numerous existing OSM toolkits, many of them are not all-inclusive for forecasting complex deep-sea spills since

thermodynamic behaviors of fluid particles are usually simplified. It is seen that the coupling of near- and far-field Lagrangian schemes with spatiotemporal dynamics of oil and water properties currently needs further investigation, particularly for field conditions. An adequate investigation and comparison provide a basis for selecting the most appropriate methods from various OSM approaches, enabling us to integrate them for the development of the DWOSM system seamlessly. Furthermore, most studies about stochastic simulation-based spill assessment did not tackle the trade-off between the computational burden and the credibility of simulation results. Hence, the newly developed oil spill model is expected to capture the sophisticated physicochemical and thermodynamic processes of deep-sea spills. Further improvement in spill risk assessment is also required to involve a more comprehensive risk evaluation system.

Chapter 3 Methodology

3.1. The framework of DWOSM

DWOSM is fundamentally built on 3D Lagrangian particle tracking, which apportions spilled oil and gas to a certain amount of LEs subjected to transport by local hydrodynamic processes. For the dispersed phase within the water column, a LE represents a cloud composed of identically sized particles; it emulates a slick when a LE (only for oil droplets) reaches the sea surface. Since the thermodynamic and hydrodynamic processes occurring within a hundred meters above the wellhead and kilometers away from the release point are distinct, modeling of a deep-water blowout can be conducted separately as two stages: 1) near-field modeling is to simulate plume dynamics and to identify petroleum fluids escaping from the plume region; 2) far-field modeling aims to track the trajectory and fate of dispersed oil beyond the near-field (Murawski *et al.*, 2020). Therefore, a deep-sea blowout simulation requires a system of models to deal with various processes, including droplet/bubble breakup and coalescence, buoyant plume dynamics, oil/gas transport, weathering processes, etc.

Specifically, DWOSM comprises multiple interlinked modeling components: two-phase flash calculations, DSD model, buoyant plume model, near- and far-field particle tracking models, and weathering algorithms (Figure 3-1). Those components constitute three modules through a holistic coupling: DWOSM-DSD, DWOSM-Nearfield, and DWOSM-Farfield. The workflow of the DWOSM can be generalized as follows: initially, flash calculation algorithms are employed to compute gas-liquid equilibrium compositions at the specified temperature, pressure, and overall compositions (see details in Appendix B). Its output defines oil and gas composition, supplying the data essential for thermodynamic modeling and oil fate simulation.

The DWOSM-DSD then predicts the diameters and volume fractions of droplets and bubbles as input to the DWOSM-Nearfield, mainly consisting of the plume model and the near-field particle tracking algorithm. Once particles escape from the plume region, their simulation results are used to provide initial conditions with the DWOSM-Farfield. Subsequently, dispersed-phase oil/gas is tracked in the water column and/or at the sea surface regarding the locations and the evolution of chemical composition and bulk properties.

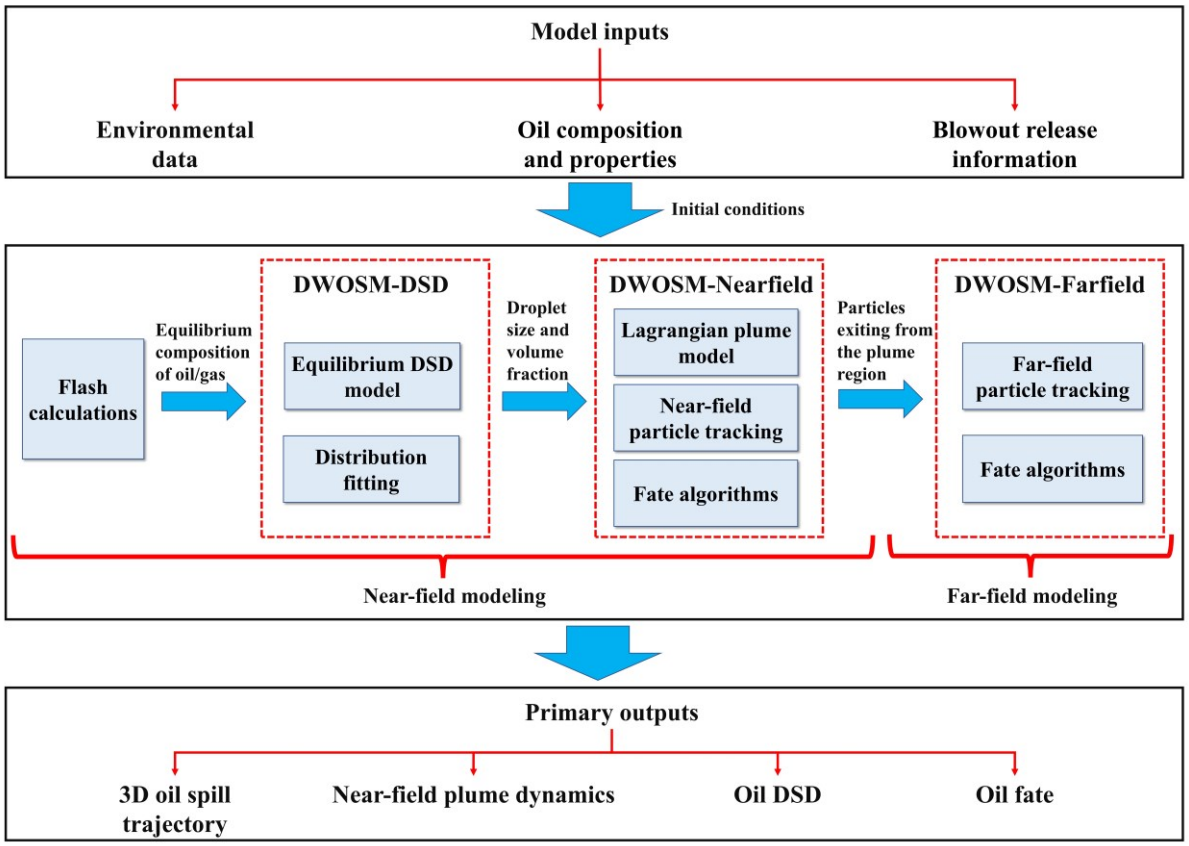

Figure 3-1 The framework of the DWOSM.

To present a detailed picture of the composition of petroleum fluids in the output of oil fate modeling, this study adopts a PC approach that splits oil into multiple chemical groups having independent properties. DWOSM requires various model inputs to define initial conditions for the subsea blowout simulation, mainly including 1) 3D velocity fields of ocean current and

wind for far-field modeling, 2) vertical profiles of salinity, temperature, and crossflow for near-field modeling, 3) spill information such as release flow rate and spill site location, 4) physicochemical properties of the released oil. The DWOSM model output directly towards helping decision-making in oil spill response majorly contains 1) a 3D oil spill trajectory; 2) the height of an intrusion layer and the plume trajectory; 3) oil and gas DSDs; 4) the evolution of the composition and properties of dispersed petroleum.

In terms of numerical implementation, this study mainly involves two types of approaches: interpolation and numerical methods for ODEs. Computing spill trajectory requires continuous velocity fields, while output from hydrodynamic and atmospheric models is discrete (Yang *et al.*, 2023). As a multivariate interpolation method on a 3D regular grid, trilinear interpolation is utilized to interpolate current and wind data in time and space, which can retrieve the velocity of current and wind information at arbitrary locations and times within the data range. The details of trilinear interpolation are depicted in Appendix A. Most formulas for the computation of OSM are a coupled system of ODEs, and stiffness sometimes arises when the system has widely varying eigenvalues. As one of the most popular tools for finding the numerical solution of stiff ODEs, the fifth-order backward differentiation formula (BDF5) with adaptive time step control is used in the DWOSM to ensure numerical accuracy and stability (Süli and Mayers, 2003; Shim *et al.*, 2011). The details of BDF5 and the adaptive time-stepping procedure are shown in Appendix A. The Python programming language is utilized to develop DWOSM and perform parallel computing via the built-in multiprocessing module.

3.2. Near-field modeling

3.2.1. Droplet size distribution model

Johansen *et al.* (2013) improved an EM by considering the viscosity effect found by Wang and Calabrese (1987), *i.e.*, the breakup with smaller viscous numbers is governed by Weber number scaling while Reynolds number scaling is applicable for larger viscous numbers. It is hypothesized that the VMD d_{50} from a jet can be estimated based on the orifice size and modified Weber number as follows:

$$\frac{d_{50}}{d_{pipe}} = AWe^{-3/5}[1 + BV_i(d_{50}/d_p)^{1/3}]^{3/5} \quad (3\text{-}1)$$

where $We = \frac{\rho_d U^2 d_{pipe}}{\sigma}$ and $Vi = \frac{\mu_d U}{\sigma}$ are the Weber number and the viscosity number, respectively. d_{pipe} is the orifice diameter (m), A and B are two empirical coefficients ($A = 24$ and $B = 0.06$ in Johansen *et al.* (2013)), ρ_d and μ_d are the density (kg/m^3) and dynamic viscosity (kg/m/s) of dispersed oil, and U is the exit velocity (m/s).

Though there is debate about which distribution is better for delineating DSD statistically, the Rosin-Rammler distribution is often more widely accepted due to its computational simplicity and extensive applications (Makarynskyy, 2021). Hence, the median droplet size predicted from the above EM and the Rosin-Rammler distribution are combined to estimate the final DSD in the DWOSM. The cumulative DSD at given diameter size d is calculated below (Nissanka and Yapa, 2018):

$$V(d) = 1 - \exp\left[-\ln 0.5 \left(\frac{d}{d_{50}}\right)^p\right] \quad (3\text{-}2)$$

where spreading parameter $p = 1.8$ in Johansen *et al.* (2013).

3.2.2. Buoyant plume model

This study uses a Lagrangian approach developed by Lee and Cheung (1990) to simulate

the near-field plume at a steady state because of its capability to handle realistic crossflows in the deep sea. As shown in Figure 3-2, the blowout duration is equally divided into a series of intervals, and each time interval corresponds to a non-interfering CV. The main properties of jet/plume CV are calculated at every time step using the equations as follows (Lee and Cheung, 1990):

Mass: $$M_{t+1} = M_t + \Delta M_t \tag{3-3}$$

Locations: $$\frac{dx}{dt} = u_t \Delta t \quad \frac{dy}{dt} = v_t \Delta t \quad \frac{dz}{dt} = w_t \Delta t \quad \frac{dS}{dt} = V_t \Delta t \tag{3-4}$$

Momentum: $$J_{x_{t+1}} = J_{x_t} + \Delta M_t u_{a_t} \quad J_{y_{t+1}} = J_{y_t} + \Delta M_t v_{a_t} \tag{3-5}$$

$$\frac{dJ_z}{dt} = F_b + F_p + \Delta M w_a \tag{3-6}$$

Thickness: $$h_{t+1} = V_{t+1} \Delta t \tag{3-7}$$

Orientation: $$\sin\phi = \frac{w}{V} \quad \cos\phi = \frac{\sqrt{u^2+v^2}}{V} \quad \sin\theta = \frac{v}{\sqrt{u^2+v^2}} \quad \cos\theta = \frac{u}{\sqrt{u^2+v^2}} \tag{3-8}$$

where M_t and J_t denote the mass (kg) and momentum (kg m/s) of CV at t time step, respectively. Δt is the length of time step used in the near-field model (s). The location of a CV can be expressed in a 3D-coordinate (x, y, z) (m). S is the distance (m) along with the plume centerline. ($u_t = J_{x_t}/M_t$, $v_t = J_{y_t}/M_t$, $w_t = J_{z_t}/M_t$) are the velocities (m/s) of a CV in XYZ directions at t time step. $V = (u^2 + v^2 + w^2)^{1/2}$ is the magnitude of the CV velocity (m/s). The vertical momentum J_z (kg m s^{-1}) is modified by adding the buoyant force of the dispersed oil $F_p = \frac{-g}{\gamma \rho_r} \sum \left[\left(\rho_a - \rho_{p,i} \right) \frac{\rho M_{p,i}}{\rho_{p,i}} \right] k$ (Dissanayake *et al.*, 2018); $k = (\frac{b-r}{b})^4$ is the buoyancy efficiency coefficient between 0 and 1 based on the distance r (m) between the particle and the plume centerline (see details in the next section). The momentum amplification factor γ accounts for turbulent kinetic energy production by the dispersed phase (default to 1.1). The radius of the plume element is b (m), and g is the gravitational constant (9.81 m/s^2). $M_{p,i}$ and

$\rho_{p,i}$ are the total mass the density of the i-th particle type in the LE. The net vertical buoyant force for a single-phase plume is expressed as $F_b = \frac{-g}{\rho_r}[M(\rho_a - \rho)]$. The CV density, the ambient density, and a reference density (kg/m^3) are denoted by ρ, ρ_a and ρ_r (kg/m^3). (u_{a_t}, v_{a_t}, w_{a_t}) are the velocities (m/s) of ambient current in XYZ directions at t time step. The thickness of a CV at t time step is h_t (m). The jet axis makes an angle of ϕ with the horizontal plane, and θ is the angle between the x-axis and the projection of the jet axis on the horizontal plane.

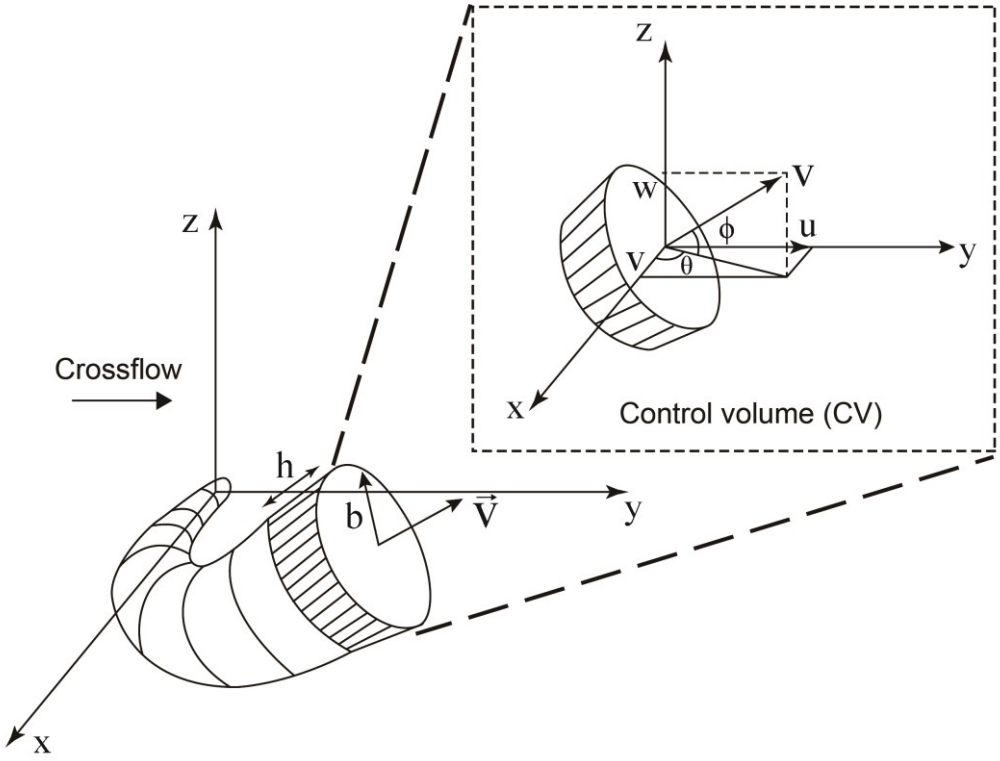

Figure 3-2 Schematic diagram of the Lagrangian plume and a CV,

(modified from Lee and Cheung (1990)).

The incremental mass ΔM_t (kg) of a CV at each time step, which consists of two components: the shear entrainment ΔM_s (kg) due to the difference between the plume element

velocity and the ambient velocity in the direction of the jet axis and the forced entrainment ΔM_f due to the ambient crossflow. For the modeling of jet entrainment (*i.e.*, the addition of ambient fluid into the plume), the maximum between ΔM_s and ΔM_f is adopted to determine the mass of entrained water at each time step. The formulation of entrainments is presented below (Lee and Cheung, 1990).

1. Shear Entrainment

$$\Delta M_s = 2\pi\alpha_s bh\Delta U\Delta t\rho_a \tag{3-9}$$

$$\alpha_s = \begin{cases} 0.055 + 0.6\sin\emptyset\,/F_l^2, & \left|\frac{F_l^2}{\sin\emptyset}\right| > 21.43 \\ 0.055 + 0.00131F_l^2/\sin\emptyset\,, & \left|\frac{F_l^2}{\sin\emptyset}\right| \le 21.43 \end{cases} \tag{3-10}$$

where α_s and $F_l = \Delta U/(\mathrm{g}'b_g)^{1/2}$ are the shear entrainment coefficient and the local densiometric Froude number, respectively. $\Delta U = \left|\vec{V} - \vec{V}_{ajet}\right|$ is the relative jet velocity in the direction of the jet axis. $\vec{V}_{ajet}$ is a component of the ambient current projected along the plume centerline. g' is the reduced gravity (m/t^2).

2. Forced entrainment

$$\Delta M_f = \Delta M_{fx} + \Delta M_{fy} + \Delta M_{fz} \tag{3-11}$$

$$\Delta M_{fx} = \rho_a|u_a|[2bh\sqrt{1-\cos^2\emptyset\cos^2\theta} + \pi b\Delta b|\cos\emptyset\cos\theta| + \frac{\pi b^2}{2}|\Delta(\cos\emptyset\cos\theta)|]\Delta t \tag{3-12}$$

$$\Delta M_{fy} = \rho_a|v_a|[2bh\sqrt{1-\cos^2\emptyset\sin^2\theta} + \pi b\Delta b|\cos\emptyset\sin\theta| + \frac{\pi b^2}{2}|\Delta(\cos\emptyset\sin\theta)|]\Delta t \tag{3-13}$$

$$\Delta M_{fz} = \rho_a|w_a|[2bh|\cos\emptyset| + \pi b\Delta b|\sin\emptyset| + \frac{\pi b^2}{2}|\Delta(\sin\emptyset)|]\Delta t \tag{3-14}$$

where ΔM_{fx}, ΔM_{fy}, and ΔM_{fz} are the forced entrainments ΔM_f (kg) in the XYZ directions. A term with a prefix Δ denotes the difference of this property between the previous and current

CVs.

In this study, most initial conditions for solving the plume model originate from Lee and Cheung (1990). The plume Froude number method is additionally employed to correct the initial volume flux by estimating the entrainment at the plume source (Wüest *et al.*, 1992).

3.2.3. Near-field particle tracking

Due to the buoyancy-driven motion, subsurface particles have a slip velocity relative to their surrounding fluid. They may not follow the same trajectory around the plume centerline when a buoyant plume bends over in the presence of crossflows. As a result, some particles may exit through the periphery of the included plume and rise upward in the water column. It reduces their buoyancy contribution to the plume as particles move away from the plume centerline (Dissanayake *et al.*, 2018). With such a loss of buoyancy from the plume, the ambient stratification will eventually trap the uprising plume to form intrusion layers (Johansen, 2003). Since the conservation of vertical momentum depends on whether particles are in the plume region, particle tracking should be implemented simultaneously with the solution of the plume element. We use the particle tracking algorithm developed by Dissanayake *et al.* (2018) to calculate the particle position relative to the plume centerline and the buoyancy efficiency of particles to the plume. The local coordinate system is defined at the base of a plume element (λ, ξ, η) with unit vectors: $\vec{\mathrm{l}}$ along the plume centerline, $\vec{\mathrm{m}}$ orientating to the curvature center, and $\vec{\mathrm{n}}$ normal to $\vec{\mathrm{l}}$ and $\vec{\mathrm{m}}$ (Figure 3-3).

$$\frac{d\vec{X}}{dt} = (V + u_l')\vec{\mathrm{l}} + (u_m' - f_e\xi)\vec{\mathrm{m}} + (u_n' - f_e\eta)\vec{\mathrm{n}} \tag{3-15}$$

where $f_e = \Delta M/(2\pi b^2 h\rho_a)$ is the entrainment frequency (s^{-1}); (u_l', u_m', u_n') are slip velocities of a particle projected on the LNM directions (m/s).

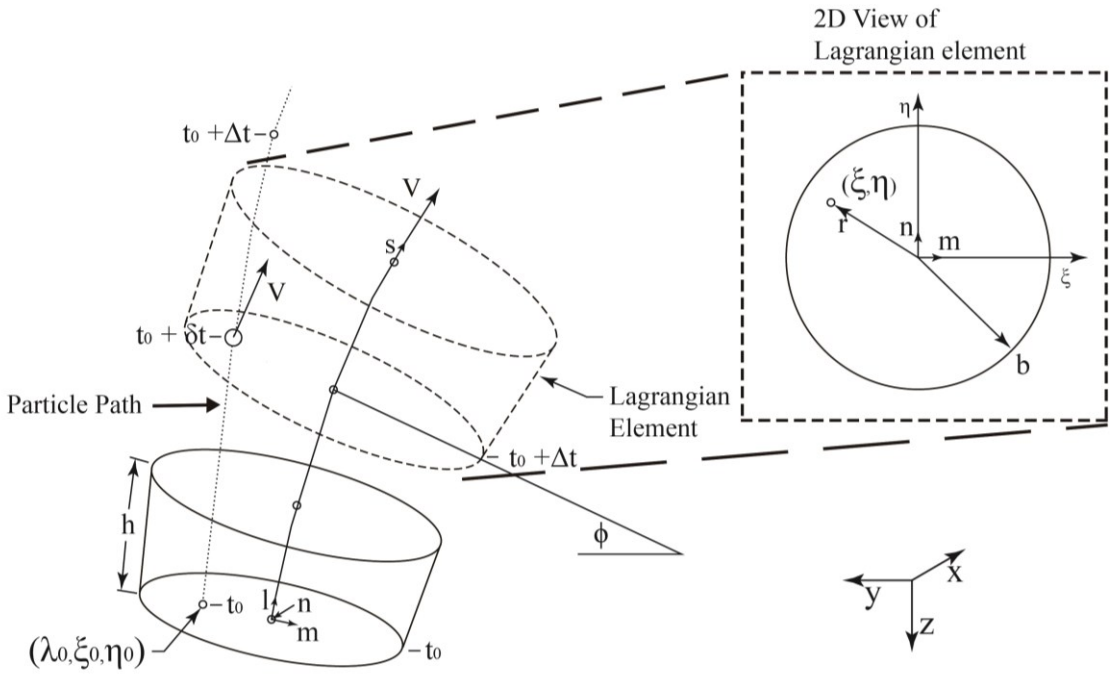

Figure 3-3 Schematic diagram of the local coordinate system in near-field modeling, (modified from Dissanayake *et al.* (2018)).

3.3. Far-field particle tracking

Figure 3-4 illustrates near- and far-field processes of deep-sea spills. Once particles leave the plume region, their transport is predominated by ocean currents, buoyancy, and ambient turbulence. The mass flux of each particle type predicted from the DWOSM-Nearfield is converted into individual particles simulated within the far-field framework. The total number of LEs is determined by user-defined particle release frequency. The Lagrangian particle-tracking algorithm is used to simulate oil/gas movement in the advection-diffusion stage, expressing the 3D trajectory of a LE in the water column and at the sea surface by the following equation:

$$\frac{d\vec{S}}{dt} = \begin{cases} \vec{U}_c + \overrightarrow{u'} + u_s\hat{k}, & z < 0 \\ \vec{u}_{sur} + \overrightarrow{u'}, & z = 0 \end{cases} \quad (3\text{-}16)$$

where $\vec{S} = (x, y, z)$ is the displacement vector of a LE at a Cartesian coordinate system; $\vec{U}_c = (u_c, v_c, w_c)$ is the advective velocity vector due to the ocean current; u_s is the rise velocity (m/s) of particles within the water column (see details in Section 3.5.2) and $\hat{k}$ is the unit vector in the vertical direction. The random walk technique is used to simulate the turbulent diffusion velocity $\overrightarrow{u'} = \sqrt{\frac{6}{\Delta t}}(R_x\sqrt{K_h}, R_y\sqrt{K_h}, R_z\sqrt{K_z})$. R_x, R_y, and R_z are assumed to be uniformly distributed independent random numbers ranging from -1 to 1. K_h and K_z are horizontal and vertical diffusion coefficients (m^2/s), respectively.

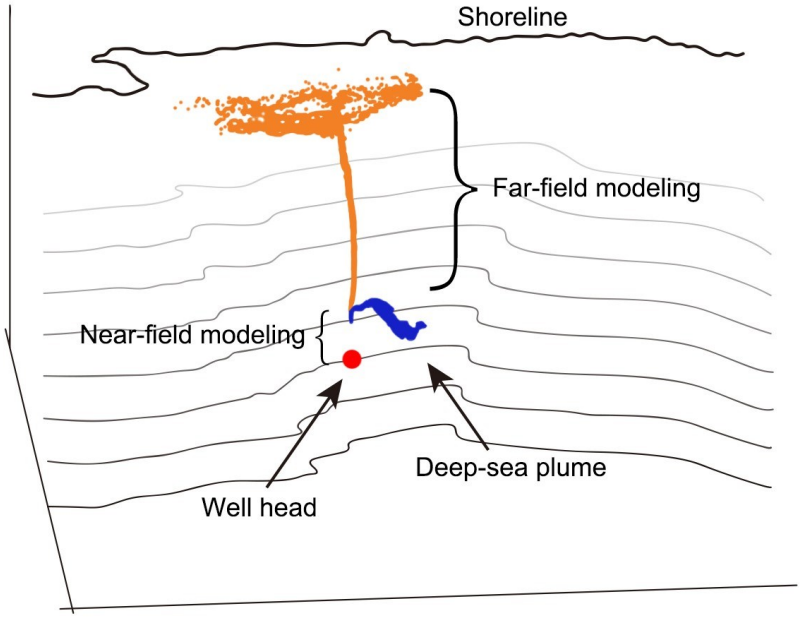

Figure 3-4 Schematic diagram of near- and far-field modeling for a deep-sea blowout, (modified from Chapman *et al.* (2014)).

As mentioned above, oil droplets reaching the sea surface may form a slick, and then the sea surface wind begins to participate in the advection of surface oil. Similar to the particle tracking for subsurface oil, an oil slick is generalized as a LE and undergoes transport and

weathering simultaneously. The advective velocity of surface oil $\vec{u}_{sur}$ can be expressed as a linear combination of current velocity $\vec{U}_c = (u_c, v_c)$ and wind speed $\vec{U}_w = (u_w, v_w)$ at the height of 10 meters over the sea surface.

$$\vec{u}_{sur} = a_c \vec{U}_c + a_w D \vec{U}_w \tag{3-17}$$

where the current drift factor a_c and the wind drift factor a_w default as the commonly used values 1 and 0.03, respectively. $D = \begin{bmatrix} \cos\theta & \sin\theta \\ -\sin\theta & \cos\theta \end{bmatrix}$ is the transformation matrix accounting for the wind deflection due to the Coriolis effect. It is only considered when Ekman flow is not included in the current data supplied to the DWOSM. θ is the deviation angle, which equals to $40° - 8\sqrt{|\vec{U}_w|}$ when $\vec{U}_w < 25$m/s and zero for other conditions.

3.4. Fate algorithms

Particles rising from the deep sea undergo a different weathering pattern than surface slicks because of their extended interaction with ambient seawater. Hence, the fate modeling for subsurface oil/gas and surface oil is implemented at particle and slick-based scales, respectively. From the perspective of practice response, decision-makers are less concerned about the fate of non-surfacing oil because most spill response technologies can only remove floating or beached oil (Murawski *et al.*, 2020). More surface weathering processes are considered in the fate algorithms of DWOSM, including spreading, evaporation, natural dispersion, and emulsification. Dissolution and biodegradation are only included in the fate modeling of subsurface oil and gas because of a larger surface area to volume ratio of droplets and bubbles than slicks. Oil-shoreline interactions are simplified here for brevity, as none of the current methods can realistically describe the natural attenuation and fate of beached oil. DWOSM-Farfield will cease to track LEs once they contact or traverse the boundary defined by the

shoreline geometry data.

3.4.1. Surface weathering

1. Spreading

As the improved performance than traditional Fay's formulas, the WMFM is applied here to calculate the slick surface area required by the evaporation model (Simecek-Beatty and Lehr, 2017). The exposed area of the slick (A_s) (m^2) is expressed as:

$$A_s = (\frac{\pi}{4})10^{-3}QR \tag{3-18}$$

where $Q = 1.7(\frac{\rho_a - \rho_o}{\rho_o})^{\frac{1}{3}} V_b^{\frac{1}{3}} t_m^{\frac{1}{4}} 10^{1.5}$ is the minor axis of the ellipse (m), $R = Q + 0.03 W_k^{\frac{3}{4}} t_m^{\frac{3}{4}} 10^{1.5}$ is the major axis. ρ_o is the oil density (kg/m^3), V_b is the initial volume of an oil spill (barrel), t_m is the time after spill (minute), W_k is the 10-meter-elevation wind speed (knot).

The thickness of an oil film will not be infinitesimal as spreading proceeds in actual cases. The spreading process will terminate once it reaches the minimum thickness of an oil slick. Slick terminal thicknesses with initial kinematic viscosity greater than 10^{-4} m^2/s or smaller than 10^{-6} m^2/s are set as 10^{-4} m and 10^{-5} m, respectively (Reed, 1989). Linear interpolation is used to obtain the terminal thickness of oil with intermediate viscosity.

2. Evaporation

The PC model is used to predict the evaporative loss of surface oil mass given its good extendibility and is depicted below:

$$\frac{dm_i}{dt} = -(1 - Y)\frac{A_s \alpha M_i P_i}{RT}(\frac{m_i/M_i}{\sum m_i/M_i}) \tag{3-19}$$

where m_i is the mass of i-th PC (kg), Y is the water content of the emulsion (%), M_i is the molar weight of i-th PC (kg/mol). P_i is the vapor pressure at the water temperature of i-th PC

(Pa), which is estimated by the modified Antoine equation (Yang *et al.*, 2017). $\alpha_i = 0.0048{W_{10}}^{0.78}{S_c}^{-\frac{2}{3}}$ is a wind dependent mass transfer coefficient (m/s) of i-th PC, W_{10} is the wind speed measured at 10 m height (m/s). $S_c = 1.38(\frac{M_w}{M_i})^{\frac{1}{3}}$ is Schmidt number, M_w is the molecular weight of water (0.018 kg/mol). R is the universal gas constant (8.3144 J/(K mol)), T is the water temperature (K).

3. Emulsification

This study first adopts methodology formulated by Fingas (2017) to determine the emulsion stability S_{em} and the time to form a specific water-in-oil state. Once the emulsion stability is obtained, its corresponding category of the emulsion can be found in the relation given by Fingas (2017). In this study, the unstable water-in-oil emulsion is regarded as non-emulsified oil because its density and viscosity barely change due to emulsification. The time to emulsion in minutes (t_{em}) is calculated as:

$$t_{em} = a_{em} + b_{em}/{H_w}^{1.5} \tag{3-20}$$

where H_w is the wave height (cm), a_{em} and b_{em} are the two empirical coefficients varying with the emulsion type. Specifically, $a_{em} = 27.1$ and $b_{em} = 7520$ if the emulsion is "stable", $a_{em} = 47$ and $b_{em} = 49100$ if the emulsion is "meso-stable", $a_{em} = 30.8$ and $b_{em} = 18300$ if the emulsion is "entrained", as given in Equation 3-21. Otherwise, there will be no formation of emulsion.

The emulsification only begins in the fate simulation when slicks are exposed to the atmosphere for over t_{em}. Then, the water content of oil slicks is estimated by a first-order relation as (Lehr *et al.*, 2002):

$$\frac{dY}{dt} = k_{em}\frac{\nu_0}{\nu_{em}}W_{10}^2\left(1 - \frac{Y}{Y_{max}}\right) \tag{3-21}$$

where Y_{max} is the maximum water fraction (%) derived from a function of the asphaltene/resin ratio in the study of Fingas and Fieldhouse (2004), ν_{em} is the kinematic viscosity of emulsion (m^2/s), v_0 is the initial kinematic viscosity of oil (m^2/s), k_{em} is an empirical constant between 1×10^{-6} and 2×10^{-6}.

4. Natural dispersion

Considering an excellent fit to observational data from a full-scale experimental oil spill with a wide testing range of oil viscosities, the first-order decay equation formulated by Johansen *et al.* (2015) is used to simulate the reduction in surface oil mass Q_s (kg) due to entrainment by breaking waves:

$$\frac{dQ_s}{dt} = -\alpha Q_s \tag{3-22}$$

where $\alpha = P^* WCC/T_m$ is an entrainment coefficient (s^{-1}), P^* is the volume fraction (%) of oil contained in oil droplets smaller than the limiting diameter D^* (mm), $T_m = 0.812\pi W_{10}/g$ is the mean wave period (s). The white capping coverage WCC (%) is expressed using an empirical correlation (Callaghan, 2008):

$$WCC = \begin{cases} 3.18\times10^{-3}(W_{10}-3.7)^3, & 3.7 < W_{10} < 11.25 \\ 4.82\times10^{-4}(W_{10}+1.98)^3, & 9.25 < W_{10} < 23.1 \end{cases} \tag{3-23}$$

Johansen *et al.* (2015) also provided a semi-empirical model to calculate the characteristic droplet size D (m) resulting from surface entrainment:

$$\frac{D}{h_{em}} = 2.251We^{-3/5}\left[1 + 0.027Vi^{3/5}\right] \tag{3-24}$$

where h_{em} is the oil slick thickness (m).

Similar to the routine in the DWOSM-DSD, the droplet sizes presumably follow a predefined statistical distribution determined by D and other parameters (here is a lognormal distribution). Eventually, P^* can be found in the newly derived DSD through a distribution

fitting. Different oil fractions are presumed to be entrained equally owing to wave entrainment acts on the slick with well-mixed components.

3.4.2. Subsurface weathering

1. Dissolution

The mass loss of each PC due to the dissolution is calculated by a first-order decay equation:

$$\frac{dm_i}{dt} = -A_d \beta_i (C_{s,i} - C_{a,i}) \tag{3-25}$$

where A_d is the surface area of oil droplet (m^2), β_i is the mass transfer coeffeicent of the i-th PC (m/s), $C_{s,i}$ and $C_{a,i}$ are the solubility (kg/m^3) and the ambient concentration (kg/m^3) for i-th PC. The details of calculating the mass transfer coefficient and solubility of PC are introduced in section 3.5.2.

2. Biodegradation

Modeling the mass loss of each PC due to the biodegradation is similar to predicting the dissolution rate:

$$\frac{dm_i}{dt} = -k_i m_i \tag{3-26}$$

where k_i is the first-order biodegradation rate for i-th PC (day^{-1}), which can be found in Galagan *et al.* (2018).

3.5. Particle/slick evolution

The LEs are treated differently in the water column and on the surface by the DWOSM as they exist in distinct forms (*i.e.*, droplets/bubbles in the subsurface and slicks on the surface) and experience different weathering processes. This section elaborates on surface and subsurface oil properties and the methods of calculating their change along with ambient

conditions.

3.5.1. Surface slick properties

Two physical properties are involved in surface oil fate modeling, *i.e.*, viscosity and density. As the model input of fate algorithms, oil properties changed by weathering, in turn, affect weathering processes to varying degrees. Their simulation is implemented based on semi-empirical formulas at a slick-based scale for brevity.

1. Density

Environmental factors and weathering processes jointly contribute to the variation in density, including evaporation, water content, temperature. Buchanan and Hurford (1988) integrated multifactor into a single equation to calculate the density of emulsified oil:

$$\rho_{em} = Y\rho_w + \rho_0(1-Y)(1+C_1 f_e)[1-C_2(T-T_0)] \tag{3-27}$$

where f_e is the mass fraction lost due to evaporation, ρ_{em} is the density of emulsion (kg/m^3) at ambient temperature T (K), ρ_0 is the initial density of oil (kg/m^3) at initial temperature T_0 (K), ρ_w is the density of seawater (kg/m^3). C_1 and C_2 are two empirical constant given by Lehr *et al.* (2002).

2. Viscosity

In contrast to a limited range of oil density variation, the viscosity of emulsified oil can increase from a few centistokes to more than a million. The kinematic viscosity of emulsion v_{em} at T can be expressed as (Pal & Rhodes, 1989):

$$v_{em} = v_0 \exp\left(K_{vis} f_{eavp}\right) \exp\left(\frac{2.5Y}{1-0.65Y}\right) \exp[C_3(\frac{1}{T}-\frac{1}{T_0})] \tag{3-28}$$

where v_0 is the initial kinematic viscosity of oil at T_0, K_{vis} is the constant ranging from 1 to 10 (Mackay *et al.*, 1980), and C_3 is an empirical constant also given by Lehr *et al.* (2002).

3.5.2. Subsurface particle properties

Unlike the sea surface environment, ambient conditions where droplets and bubbles ascend from the deep sea to the surface vary drastically, particularly for the pressure and temperature. Thus, the evolution of subsurface oil and gas properties is simulated at the particle scale using thermodynamic modeling based on the Peng-Robinson Equation of State (PR-EOS) (Lopez-Echeverry *et al.*, 2017).

1. Shape

To precisely characterize the free motion of underwater particles, the shape of the dispersed phase can be categorized into three groups: spherical, ellipsoidal, and spherical-cap. Several dimensionless quantities are introduced to predict the particle shape collectively, including the Bond number (Eo), Reynolds number (Re), and Morton number (Mo). The criteria for each generalized shape group are listed below: the particle shape is categorized as spherical once the H parameter ($\frac{4}{3}EoMo^{-0.149}(\mu_d/\mu_c)^{-0.14}$) is less than two, indicating that particles are approximated by spheres (μ_c is the dynamic viscosity (kg/m/s) of the continuous phase); it corresponds to ellipsoidal when these conditions are met (Eo < 40 and Mo < 10^{-3} and $Re >$ 0.1 and H < 1000), representing oblate particles with a convex interface around the surface; otherwise, the spherical cap is used to delineate the shape of particles under rest conditions.

2. Surface area and diameter

Empirical correlations for the surface area and diameter of a particle corresponding to different shapes can be found in the book by Clift *et al.* (2005).

3. Rise velocity

Extensive empirical correlations for the rise velocity of fluid particles were proposed by

Clift *et al.* (2005), which accounts for the equivalent diameter, the dynamic viscosity of the continuous phase, the oil-water interfacial tension (IFT), and the density of dispersed phase and ambient seawater. In addition, different modifications for the Reynolds number were correspondingly given to spherical and ellipsoidal particles.

When the particle shape is spherical, Re is expressed as below:

$$Re = \begin{cases} \frac{N_D}{24} - 1.7569 \times 10^{-4} {N_D}^2 + 6.925 \times 10^{-7} {N_D}^3 - 2.3027 \times 10^{-10} {N_D}^4, & N_D \leq 73 \\ 10^{-1.7095 + 1.33438W - 0.11591W^2}, & 73 < N_D \leq 580 \\ 10^{-1.81391 + 1.34671W - 0.12427W^2 + 0.006344W^3}, & 580 < N_D \leq 1.55 \times 10^7 \\ 10^{5.33283 - 1.21728W + 0.19007W^2 - 0.007005W^3}, & 1.55 \times 10^7 < N_D \leq 5 \times 10^{10} \end{cases} \quad (3\text{-}29)$$

where $N_D = \frac{4\rho_c(\rho_c - \rho_d)gd^3}{3{\mu_c}^2}$ is the "Best number", $W = \log_{10} N_D$ is the common logarithm of N_D, d is the equivalent spherical diameter (m), ρ_c and μ_c are the density (kg/m^3) and dynamic viscosity (kg/m/s) of the continuous phase, respectively.

For the particle with an ellipsoidal shape, Re is calculated as:

$$Re = M^{-0.149}(J - 0.857) \quad (3\text{-}30)$$

where $J = \begin{cases} 0.94H^{0.757}, & 2 < H \leq 59.3 \\ 3.42H^{0.441}, & H > 59.3 \end{cases}$.

Both spherical and ellipsoidal particles adopt the same equation for calculating rise velocity:

$$u_s = \frac{\mu_c}{\rho_c d} Re \quad (3\text{-}31)$$

here, the difference in the rise velocity of clean and dirty ellipsoidal particles is ignored, as all the particles are assumed to be contaminated in this study.

A simple empirical relation is used to compute the rise velocity of spherical cap fluid particles:

$$u_s = 0.711\sqrt{gd\Delta\rho_{ow}} \tag{3-32}$$

where $\Delta\rho_{ow}$ is the relative oil-water density difference.

4. Density and viscosity

The density of the fluid particle is computed by the ratio of average molar mass to molar volume using the PR-EOS (see details in Appendix B). We implement the volume shift to correct the density given that cubic EOSs inherently fail to provide a reliable prediction of liquid phase densities (Lin and Duan, 2005). Viscosity simulations of hydrocarbon mixture are based on a corresponding states model, and their calculation scheme is well documented in Pedersen *et al.* (2014).

5. Interfacial tension

An empirical correlation dependent on density difference and temperature is used to express the IFT between the dispersed phase and the continuous phase (Danesh, 1998).

6. Solubility

The solubilities of different PCs are calculated through modified Henry's law, accounting for the dependence of Henry's law constant on pressure, temperature, and salinity (Dissanayake *et al.*, 2018).

7. Mass transfer coefficient

Mass transfer rates can be impacted by whether the phase boundary of a fluid particle is contaminated or not. The oil-seawater interface is commonly regarded as contaminated as clean particles (surfactant-free systems) are rare in the real world (Zheng and Yapa, 2000; Zhao *et al.*, 2017; Pesch *et al.*, 2018). This study predicts the mass transfer coefficient of dirty particles based on the Sherwood Number and particle properties (Clift *et al.*, 2005).

8. Diffusivity

The revised Othmer-Thakar equation is applied to estimate the diffusivities of dissolved substances in aqueous solutions (Gao *et al.*, 2021), which is used to compute the mass transfer coefficient of various components.

It is noticeable that the methods mentioned above need multiple thermodynamic component-specific properties. Nevertheless, most existing oil databases miss relative information, such as critical properties and binary interaction parameters. Gros *et al.* (2018) presented a collection of methods to compute the properties necessary for those simulations utilizing the data obtainable from the commonly used oil library, the Automated Data Inquiry for Oil Spills (ADIOS), developed by the National Oceanic and Atmospheric Administration (NOAA) (accessible at https://github.com/NOAA-ORR-ERD/OilLibrary as of Feb 14, 2024). This novel procedure is employed to provide the parameters for modeling thermodynamic properties.

3.6. Stochastic simulation-based risk assessment framework

A methodological framework presented by Chiri *et al.* (2020) is modified by introducing a new evaluation method to obtain the PAH-related blowout risk. As shown in Figure 3-5, the first step is to choose offshore waters with deepwater wells or reservoirs as a targeted area. Next, environmental field data suitable for the specified region, including ocean currents and wind forcing, need to be determined. Selecting reanalysis products with extended temporal scope and fine spatial resolution is highly recommended (Chiri *et al.*, 2020). The former may guarantee that the database used for retrieving met-ocean variables contains sufficient information on long-term oceanic circulation; the latter is required to capture vital spatial

features within the study area, such as convoluted shorelines or small islands. After acquiring oceanic and atmospheric reanalysis, the unification of their temporal resolutions is necessary, and then datasets are merged into a single matrix (see details in the following paragraph). Since the dimension of the newly assembled matrix can easily surpass tens of thousands, computational complexity and the curse of dimensionality will severely hinder the follow-up procedure, especially for clustering. Principal Component Analysis (PCA), a widely used dimensionality reduction technique via singular value decomposition in machine learning (Kherif and Latypova, 2020), is applied to identify the principal components of the matrix obtained from the previous step. Once the matrix compression is completed, cluster analysis becomes feasible to extract met-ocean patterns from the low-dimensional data generated from PCA. As one of the most popular unsupervised learning, a K-means clustering algorithm is used here for partitioning the dataset into a user-specified number of clusters based on squared Euclidean distances (Sinaga and Yang, 2020). Each cluster represents a 3D spatiotemporal evolution of regional met-ocean conditions during a period. Finally, a collection of new environmental data is available to be the input of current and wind fields for stochastic OSM. Multiple deterministic simulations of a deep-sea blowout are conducted using the DWOSM to predict the oil transport and fate under each met-ocean pattern, providing statistical attributes for spill risk quantification. A series of hazard maps can be produced by averaging superimposed simulation results from all the spill scenarios.

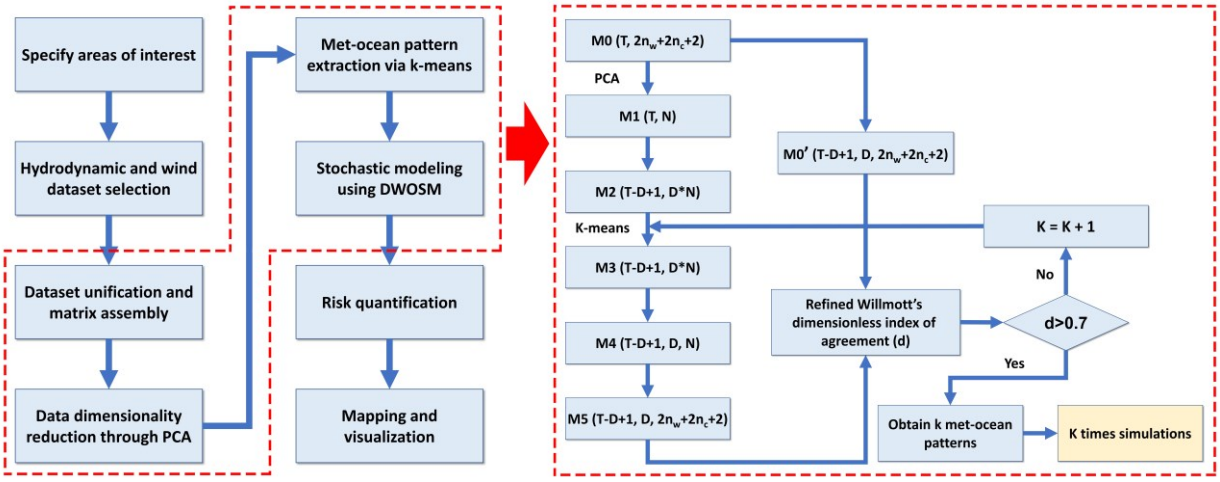

Figure 3-5 The flowchart of an integrated stochastic modeling methodology (left panel) and the workflow of the met-ocean pattern extraction (right panel).

The right panel of Figure 3-5 exhibits a detailed flow diagram for dimensionality reduction and pattern extraction. Before the implementation of PCA, current and wind datasets should be assembled into one matrix $M0$ for convenience. This matrix contains information on three types of velocity fields: surface ocean currents, winds, and depth-averaged subsurface currents. Rather than adopting the original 3D ocean reanalysis product, the current dataset is divided into surface and underwater parts pursuant to the hypotheses stated by Chiri *et al.* (2020): a) in a water column, the rise velocity of oil droplets driven by buoyancy is considerably faster than their horizontal velocity caused by subsurface crossflows; b) no significant velocity gradient exists along the vertical profile of water depth. The first premise implies a limited horizontal displacement of rising droplets, making only subsurface current data near the vertical projection of the release point crucial to oil transport modeling. The second allows using a depth-averaged velocity of subsurface currents to characterize crossflows within the entire water column. Combined with the two premises, the raw datasets are transformed into a

concatenation of wind fields and surface and subsurface current fields as $M0$:

$$\begin{bmatrix} Uw_1^1 & \cdots & Uw_{n_w}^1\ Vw_1^1 & \cdots & Vw_{n_w}^1\ Uc_1^1 & \cdots & Uc_{n_c}^1\ Vc_1^1 & \cdots & Vc_{n_c}^1\ Ud^1\ Vd^1 \\ Uw_1^2 & & Uw_{n_w}^2\ Vw_1^2 & & Vw_{n_w}^2\ Uc_1^2 & & Uc_{n_c}^2\ Vc_2^1 & & Vc_{n_c}^1\ Ud^2\ Vd^2 \\ \vdots & \ddots & \vdots\ \vdots & \ddots & \vdots\ \vdots & \ddots & \vdots\ \vdots & \ddots & \vdots\ \vdots\ \vdots \\ Uw_1^T & \cdots & Uw_{n_w}^T\ Vw_1^T & \cdots & Vw_{n_w}^T\ Uc_1^T & \cdots & Uc_{n_c}^T\ Vc_1^T & \cdots & Vc_{n_c}^T\ Ud^T\ Vd^T \end{bmatrix}_{T\times(2n_w+2n_c+2)} \tag{3-33}$$

where U and V are longitudinal and latitudinal velocity components, respectively. w and v denote winds and ocean currents, respectively. Ud and Vd are the depth-averaged current velocity in the water column. n_w and n_c represent the total node number of the mesh grid for wind and surface current fields at a time step, respectively. T is the maximum time step for both wind and current data. Each row of $M0$ represents the spatial met-ocean condition at a time step.

The dimensions of $M0$ are evidently enormous and cannot be applied directly to the clustering algorithm. PCA is accordingly used to compress the size of $M0$, generating a new matrix $M1$ below.

$$\begin{bmatrix} PC_1^1 & PC_2^1 & \cdots & PC_N^1 \\ PC_1^2 & PC_2^2 & \cdots & PC_N^2 \\ \vdots & \vdots & \vdots & \vdots \\ PC_1^T & PC_2^T & \cdots & PC_N^T \end{bmatrix}_{T\times N} \tag{3-34}$$

where PC_i^t denotes the *i*-th principal component at t time step. N is the total number of principal components.

A rearrangement is required to consider the temporal evolution of met-ocean conditions before employing K-means clustering to $M1$. Assume that the number of time steps of met-ocean patterns within the simulation duration is D. Through repeatedly sliding a window of D rows of principal components along with each column of $M1$, $T - D + 1$ sub-patterns with N data nodes and D time steps are created to represent every possible met-ocean pattern having

consecutive D-steps over the entire time series. A matrix $M2$ is eventually yielded below as a result of reconstruction for $M1$.

$$\begin{bmatrix} PC_1^1 & PC_1^2 & \cdots & PC_1^D & \cdots & PC_N^1 & PC_N^2 & \cdots & PC_N^D \\ PC_1^2 & PC_1^3 & \cdots & PC_1^{D+1} & & PC_N^2 & PC_N^3 & \cdots & PC_N^{D+1} \\ \vdots & \vdots & \ddots & \vdots & & \vdots & \vdots & \ddots & \vdots \\ PC_1^{T-D+1} & PC_1^{T-D+2} & \cdots & PC_1^T & & PC_N^{T-D+1} & PC_N^{T-D+2} & \cdots & PC_N^T \end{bmatrix}_{(T-D+1)\times(D*N)} \quad (3\text{-}35)$$

Here, each row means principal components derived from met-ocean variables during the D-steps period.

Applying the K-means algorithm necessitates a predefined cluster number. We initialized the number of met-ocean patterns as one and determined whether to increase the cluster on the basis of follow-up evaluations (the right panel of Figure 3-5). By using clustering analysis to $M2$, the centroid(s) of each cluster and the label for those sub-patterns will be generated. The labeled rows of $M2$ are then substituted with their cluster centroids that represent the average of data points within that cluster, *i.e.,* build a matrix $M3$ ($(T-D+1)\times(D*N)$). Afterward, $M3$ is rearranged into a 3D matrix $M4$ ($(T-D+1)\times D\times N$)) by splitting up its columns. With the eigenvectors generated by PCA, $M4$ can be further restored as $M5$ ($(T-D+1)\times D\times(2n_w+2n_c+2)$) for comparison with the original dataset. Similar to the reorganization from $M1$ to $M2$, $M0$ is reconstructed as $M0'$ ($(T-D+1)\times D\times(2n_w+2n_c+2)$) by moving a D-steps window. When $M0'$ and $M5$ are of identical size, the next step is to measure the error between the original dataset and extracted met-ocean patterns. In the realm of environmental sciences, various approaches have emerged over the last decades to characterize model performance, *i.e.,* most evaluate the similarity among modeled and observed variables (Bennett *et al.*, 2013). Willmott *et al.* (2015) comparatively examined three commonly used model-performance metrics and found that a refined Willmott's dimensionless

index of agreement ($-1 \leq d_r \leq 1$) has the broadest utility. Hence, this study used this statistical index as an error metric. The agreement index closer to one indicates better agreement between model predictions and observations, yet some discrepancies present in how great the value of Willmott's index can indicate good simulation performance, varying from 0.5 in Willmott *et al.* (1985) to 0.65 in Chiri *et al.* (2020). This study adopted a conservative threshold of 0.7 to ensure a well-accepted result of clustering analysis. If the current index of agreement does not meet the condition (the right panel of Figure 3-5), we step back to implement PCA with the updated cluster number; otherwise, the pattern extraction is completed. Each cluster represents a spatiotemporal evolution of met-ocean patterns within the study area during the simulation period. Hereafter, stochastic OSM corresponding to k patterns becomes achievable.

Instead of employing a binary indicator from the original work for risk quantification, PHA concentration and surface oil loading are used to characterize the level of surface oil contamination. Table C-1 summarizes the thresholds of the two indexes and the rationale for formulating them from the perspective of appearance and ecological impacts. The risk indicator and other oil spill features (*e.g.,* slick area and thickness) are computed by iterating grid cells of a 3D mesh grid encompassing the waters where oil appears. An integrated risk index (RI_i) at the *i*-th voxel is calculated as:

$$RI_i = \sum_{k=1}^{K} P_{k,i} \frac{S_{PAH} C_{PAH,k,i} S_{OL} \delta_{k,i}}{K} \tag{3-36}$$

where $P_{k,i}$ is the probability (%) of oil occurrence at the *i*-th voxel under the *k*-th met-ocean pattern. K is the total number of met-ocean patterns. S_{PAH} and S_{OL} are scaling coefficients for PAH concentration (μg/l) and surface oil loading (g/m^2), respectively. $C_{PAHs\,k,i}$ and $\delta_{k,i}$ are

PAH concentration and surface oil loading at the *i*-th voxel under the *k*-th met-ocean pattern, respectively.

3.7. Summary

This chapter introduces detailed methodologies for developing DWOSM, including the model structure, composition, input data, and numerical methods. The methods used in each modeling component are summarized below:

1) A well-tested EM is used to predict oil and gas DSDs emanating from subsea blowouts, which provides the information required by particle tracking and fate algorithms.
2) A Lagrangian plume model coupled with advanced near-field particle tracking and fate algorithms, collectively termed DWOSM-Nearfield, is applied to simulate the near-field plume dynamics and track the dispersed phase in the plume region. Its output of particles exiting from the plume serves as the input to offer the initial condition of DWOSM-Farfield.
3) Integration of Lagrangian particle tracking and various fate algorithms allow DWOSM-Farfield to forecast the transport and fate of spill oil and gas beyond the near field. Furthermore, empirical correlations and thermodynamic modeling based on the PR-EOS are used to simulate the evolution of particle/slick properties with ambient conditions.
4) A recent stochastic simulation-based risk assessment framework is modified by embedding DWOSM and adding a PAH-related risk evaluation indicator to quantify the risk spatial distribution resulting from subsea oil spills.

Chapter 4 Application and Testing of DWOSM in Eastern Canadian Waters

4.1. Overview of the study site

The study area for testing DWOSM is the offshore waters of eastern Newfoundland, Canada (Figure 4-1). Regulatory approval has recently been granted for offshore oil and gas development in deep waters off the east coast of Canada in the Flemish Pass Basin, about 500 kilometers east of St. John's, Newfoundland (CBC, 2022). This and the Canada-Newfoundland Offshore Petroleum Board's consideration to award new oil and gas leases within the region, including the Northeast Newfoundland Slope Conservation Area (designated a "Marine Refuge" by the Department of Fisheries and Oceans in 2017 to protect fragile cold-water corals and sponges that provide essential habitat for fish), has raised environmental concerns (WWF, 2020). The predictive models developed under this study are applied to a hypothetical test case based on site-specific data to determine potential ecological risks from an accidental subsurface oil release to this region of concern. The hypothetical spill event for model evaluation is based on the following scenario. At 12:00 on 10 October 2021, a ruptured underwater pipeline at 800m depth accidentally released a Canadian east coast crude oil with an American Petroleum Institute (API) gravity of 37.1 in eastern Newfoundland waters at a flow rate of 3,000 barrels per day. This blowout lasted ten days and eventually ceased at 12:00 on 20 October 2021, following the release of 4769.6 cubic meters of crude oil.

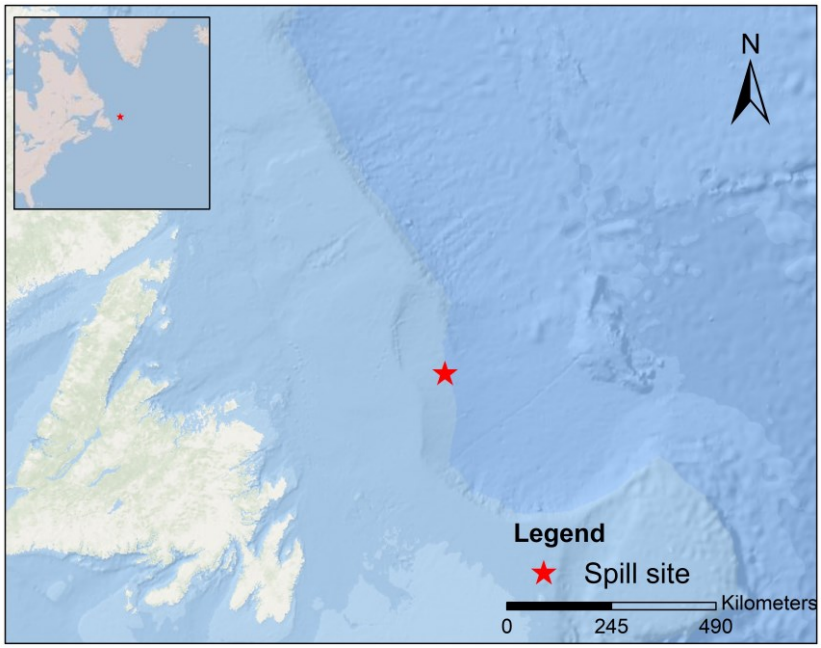

Figure 4-1 The study area of a hypothetical blowout in Eastern Canadian waters.

4.2. Model configurations and data collection

Since the DWOSM is an integrated system composed of multiple individual components, comparisons among each module and established oil spill models are accordingly made to investigate their validity and utility (Figure 4-2). Simulation scenarios for all modules are defined based on the hypothetical blowout case (Table D-1), except for DWOSM-DSD, as an open-source PDM is not found. As a compromise, the DWOSM-DSD module is validated by comparing its output with laboratory observations and simulation results from a previous study. Rest are compared to corresponding spill models employing the same or close configurations. Specifically, the DWOSM-DSD is used to hindcast the observed oil droplet size and its related volume fraction from SINTEF's tower basin experiments. The DSD results from the EM are also compared with the simulation result from a PDM model Oildroplets (Brandvik *et al.*, 2013). Then, the DWOSM-Nearfield module and the TAMOC (version 2.1.0, accessible at

https://github.com/socolofs/tamoc as of Feb 14, 2024) are applied to simulate plume dynamics and particle trajectories within the plume region. Regarding validation of the far-field modeling, oil spill trajectories predicted from the DWOSM-Farfield are respectively compared with the output from two OOSMs, *i.e.*, SIMAP and PyGNOME (an open-source scripting interface of GNOME, version 1.1.3, accessible at https://github.com/NOAA-ORR-ERD/PyGnome as of Feb 14, 2024). Only SIMAP is used for a comparison of oil mass balance as some functionalities of PyGNOME (*e.g.,* coupling between surface oil weathering with underwater blowouts) are presently less well-tested and still under active development. After the verification for near-field modeling, constant and spatiotemporally varying background winds and currents are input to SIMAP and GNOME to examine the far-field particle tracking under different environment fields, respectively. Furthermore, through the presence and absence of each weathering process involved in the DWOSM, various scenarios are formulated to investigate the impacts of different factors on the mass balance of an oil spill.

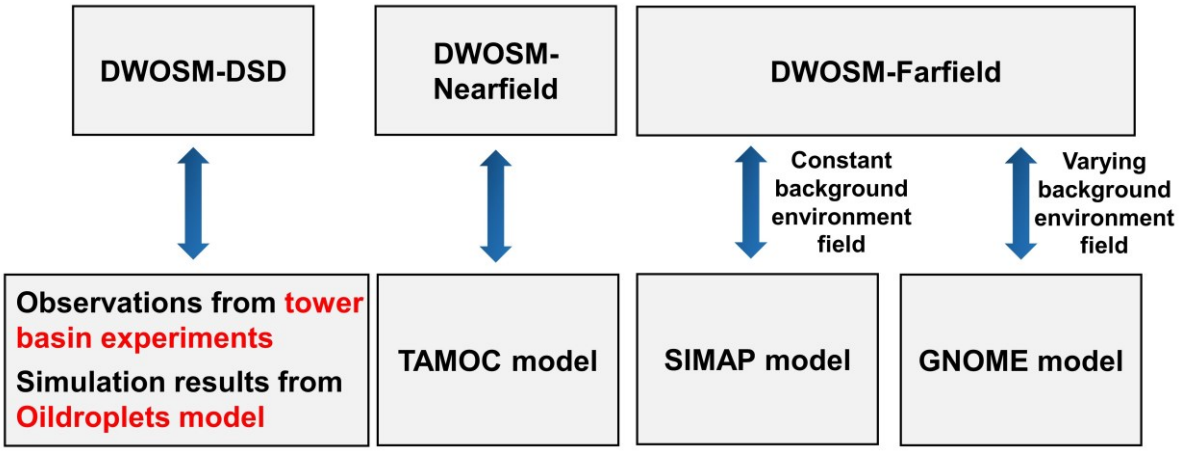

Figure 4-2 Diagram of comparative scenarios designed for model verification.

4.3. Results and discussion

4.3.1. Comparison of near-field modeling

SINTEF performed a series of tower basin experiments to investigate the DSD of underwater oil versus release conditions (*i.e.*, flow rates and nozzle diameters) and physical properties of petroleum (*e.g.,* viscosity, density, and IFT) (Brandvik *et al.*, 2013). The experimental setups for different simulations of subsurface oil releases are shown in Table 1. The nozzle diameter ranged from 0.5 to 3.0 mm, and the initial release velocity varied from 9.4 to 42.4 m/s. More details of SINTEF experiment setups were reported in the study of Brandvik *et al.* (2013) and Brandvik *et al.* (2014b).

Table 4-1 The initial setup of SINTEF laboratory experiments for model validations.

Experiments		Nozzle diameter (mm)	Release velocity (m/s)	IFT (mN/m)	Specific gravity	Viscosity (cP)
Brandvik *et al.*, 2013	Exp1	0.5	17.0	15.5	0.839	10
	Exp2	0.5	42.4			
	Exp3	1.5	9.4			
	Exp4	1.5	14.1			
	Exp5	2.0	26.5			
	Exp6	3.0	11.8			
Brandvik *et al.*, 2014a and b	Exp7	1.5	26.4			
	Exp8	3.0	18.8			

Note: Exp denotes experiment.

Figure 4-3 presents the comparison between observations from tower tank experiments and oil DSD simulated from the DWOSM-DSD and the Oildroplets. Both model results fit the experimental data well in most cases, particularly Exp-1, 3, and 8, with mean absolute error (MAE) and root mean squared error (RMSE) less than 6.6 and 8.5, respectively (see Figure 4-3 a, c, and h). The modeled DSD from the DWOSM-DSD has a larger discrepancy on Exp- 4, 6, and 7 than the results of Oildroplets (EM's MAE ranges from 8.0 to 14.5, and RMSE varies

from 9.5 to 18.0; PDM's MAE ranges from 3.2 to 6.3 and RMSE varies from 3.5 to 6.8), of which tiny droplets (<200 μm) account for a higher fraction compared to the actual value (Figure 4-3 - d1, f1, and g1). The EM model employed by the DWOSM is based on semi-empirical relations derived from given experiments. This study uses coefficients estimated by Brandvik *et al.* (2014) and does not implement calibration of empirical parameters with different release conditions and oil properties. During actual spill incidents, it is commonplace to omit calibration for those coefficients and adopt widely used values due to the urgency of the response. On the other hand, the EM model performs better in some experiments (Exp-1, 2, 5, and 8) than the calibrated PDM and close predictions to observations (Figure 4-3 - a2, b2, e2, and h2), indicating the applicability and validity of empirical coefficients taken in this study.

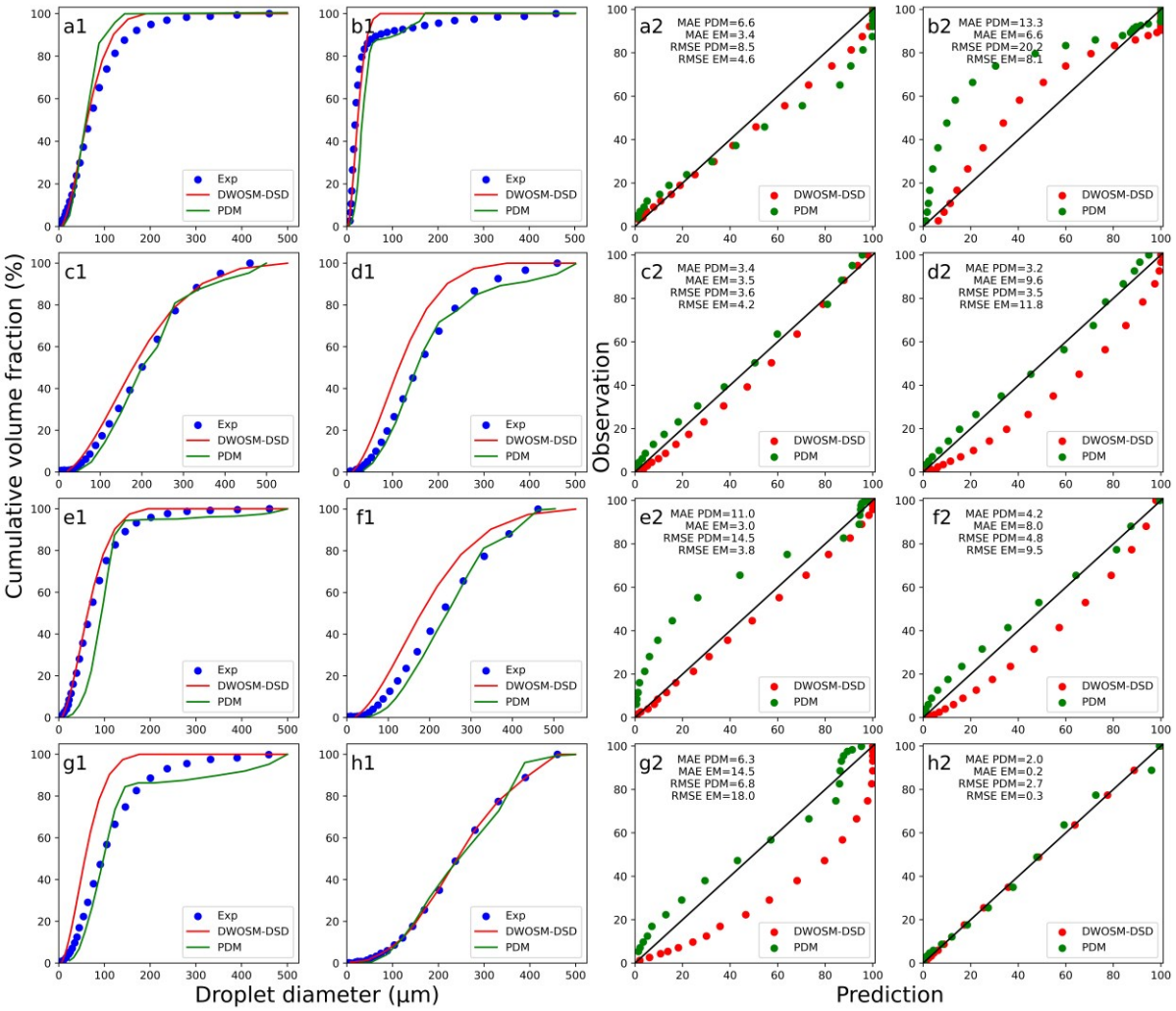

Figure 4-3 The comparison of DSD between SINTEF experimental observations and hindcast results from DWOSM-DSD and Oildroplets: figures a1-h1 are a direct comparison of cumulative volume fraction; figures a2-h2 show evaluation of model performance and error metrics.

Table 4-2 summarizes some essential results of plume dynamics at the near-field termination and droplet evolution within the plume region from the TAMOC and the DWOSM-Nearfield module. In DSD computation, both models assign oil volume fractions into ten logarithmic spaced droplet size bins (numbered from 0 to 9). Generally, two simulations have close predictions except for the mass of oil droplets at the exiting point (Table 4-2). The time

that petroleum fluids travel from the release point over the plume periphery is within a range of 0.01 to 0.12 hours. As shown in Figure 4-4, all the oil droplets are beyond the near-field region when they ascend to a depth of 777.0 meters. The differences in the predicted depth of exiting points are negligible, mirrored by their relative error of less than 0.5%. The rise velocity of oil droplets obtained from DWOSM-Nearfield ranges from 0.03 to 0.15 m/s, slightly faster than that from TAMOC, leading to a shorter time required by droplets to escape from the plume. However, absolute errors for rise velocity and timing of exit are trivial from a practical standpoint, fewer than 0.03 m/s (size bin 5) and 2.4 minutes (size bin 0), respectively. All the size bins simulated from DWOSM have around two times greater droplet mass than that of TAMOC. Although both models adopt the EM to predict oil DSDs, TAMOC performs flash calculations and accordingly produces a certain fraction of gas in its composition output. DWOSM entirely ignores this procedure when the gas-oil ratio (GOR) is zero. Both models use the flow rate of dead oil as an input of the near-field simulation, while the appearance of gas composition enlarges the mass flux of petroleum fluids in the TAMOC simulation. Consequently, the increasing exit velocity reduces the size of oil droplets and thus makes their mass smaller. Likewise, the discrepancies in the predictions of the near-field plume dynamics are caused by the same reason. The enhanced initial momentum drives the buoyant plume to reach further and higher (Figure 4-4). As the rate of shear entrainment is positively correlated to a characteristic velocity in the plume, more entrained ambient waters increase the plume element mass and width from the result of TAMOC.

Table 4-2 A compassion of near-field plume and particles results between TAMOC and DWOSM-Nearfield.

I	The results of near-field particles											
	Rise velocity (m/s)			Timing of exit (hours)			Depth of exiting point (m)			Droplet mass (kg)		
	T	D	R	T	D	R	T	D	R	T	D	R
0	0.02	0.03	0.50	0.12	0.08	0.33	777.0	779.3	0.0	4.4×10^{-7}	9.1×10^{-7}	0.52
1	0.04	0.05	0.25	0.07	0.05	0.29	779.4	782.0	0.0	1.2×10^{-6}	2.6×10^{-6}	0.52
2	0.05	0.07	0.40	0.05	0.03	0.40	780.9	783.4	0.0	3.5×10^{-6}	7.4×10^{-6}	0.52
3	0.07	0.09	0.29	0.03	0.02	0.33	783.4	784.8	0.0	1.0×10^{-5}	2.1×10^{-5}	0.52
4	0.10	0.12	0.20	0.02	0.02	0.00	784.6	785.8	0.0	2.9×10^{-5}	6.0×10^{-5}	0.52
5	0.12	0.15	0.25	0.02	0.01	0.50	785.6	785.6	0	8.1×10^{-5}	1.7×10^{-4}	0.52
6	0.14	0.14	0.0	0.01	0.02	1.00	785.7	785.6	0.0	2.3×10^{-4}	4.8×10^{-4}	0.52
7	0.14	0.14	0.0	0.01	0.02	1.00	785.8	785.7	0.0	6.5×10^{-4}	1.4×10^{-4}	0.52
8	0.14	0.13	0.07	0.02	0.02	0.0	785.9	785.8	0.0	0.0019	0.0039	0.52
9	0.13	0.13	0.0	0.02	0.02	0.0	785.9	785.9	0	0.0053	0.0110	0.52

The results of plume dynamics at the termination								
Depth of intrusion layer (m)			Plume element mass (kg)			Plume width (m)		
T	D	R	T	D	R	T	D	R
785.1	785.0	0.0	302.2	262.9	0.15	11.7	11.0	0.06

Note: T and D denote the result from TAMOC and DWOSM-Nearfield, respectively; R represents relative error, I means index.

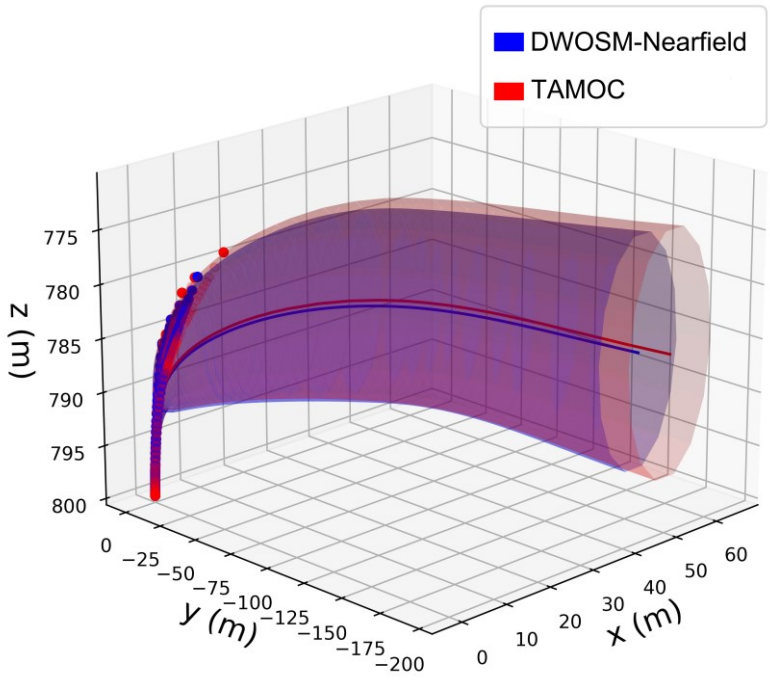

Figure 4-4 The trajectories of the near-field plume and particles predicted from DWOSM-Nearfield (in blue) and TAMOC (in red).

4.3.2. Comparison of far-field modeling

4.3.2.1. SIMAP model

A comprehensive comparison of oil fate modeling between DWOSM-Farfield and SIMAP is carried out in constant and varying environmental fields. When wind conditions are stable, the two models present comparable trends of oil mass in three environmental compartments: sea surface, water column, and atmosphere (Figure 4-5a). The mass of surfaced and evaporated oil increases linearly, and half of the released oil leaves on the sea over ten days; submerged oil is on the uplift during the initial phase (around the first three days in SIMAP and less than one day in DWOSM) and then maintains a relatively low level. More surface oil from DWOSM allows slightly faster evaporation than SIMAP until volatile hydrocarbon components are gone. There is little discrepancy between mass balance predictions from the two models except for submerged oil. Ten days after the spill, nearly 250 metric tons (Mts) and 50 Mts of oil remain in the upper water column from SIMAP and DWOSM, respectively. This disagreement is caused by different algorithms of wave entrainment taken by the two spill models since similar approaches are applied to simulate evaporation and dissolution. Compared with the mass balance under stable and weak-wind conditions, surface and subsurface oil trends are substantially altered in varying wind fields (Figure 4-5b, c, and d). Submerged oil from SIMAP fluctuates and rises to 1,186 Mts at ten days, 143 Mts greater than that of DWOSM (Figure 4-5c); both predicted surface oils unsteadily climb to about 1300 Mts despite the inconsistency prior to the last two days (Figure 4-5b). The effect of wind forcing on oil evaporation is less significant than other processes, causing parallel tendencies of oil entering the air in the two simulations (Figure 4-5d).

Similar to the scenario using steady background fields, the discrepancy in surface and subsurface oil is attributable to different dispersion algorithms employed in the two models. It was reported that the difference in entrainment rates between Li's algorithm and Delvigne and Sweeney's model could be considerably amplified as the wind speed increases from 4 to 10 m/s (Li *et al.*, 2017). In particular, the fraction of dispersed oil in the SIMAP is five times greater than that of the traditional method at a wind speed of 10 m/s. The derivation of Li's entrainment model is based on several individual processes, including white capping coverage, wave energy dissipation, and significant wave height, to obtain a natural dispersion rate as a function of wind speed. Those processes are positively related to wind speed and can increase energy dissipation rate but are not independent. Such integration double counts the effects of high winds/waves as its multiple parameters rely on wind speed, likely leading to an overestimated entrainment rate. Overall, evaporation dominates the mass balance of oil spills without the wind-wave effect, while natural dispersion becomes predominant under strong winds. Given the wide variations in entrainment models, further study is required to examine the accuracy and validity of the two methods in various environmental conditions.

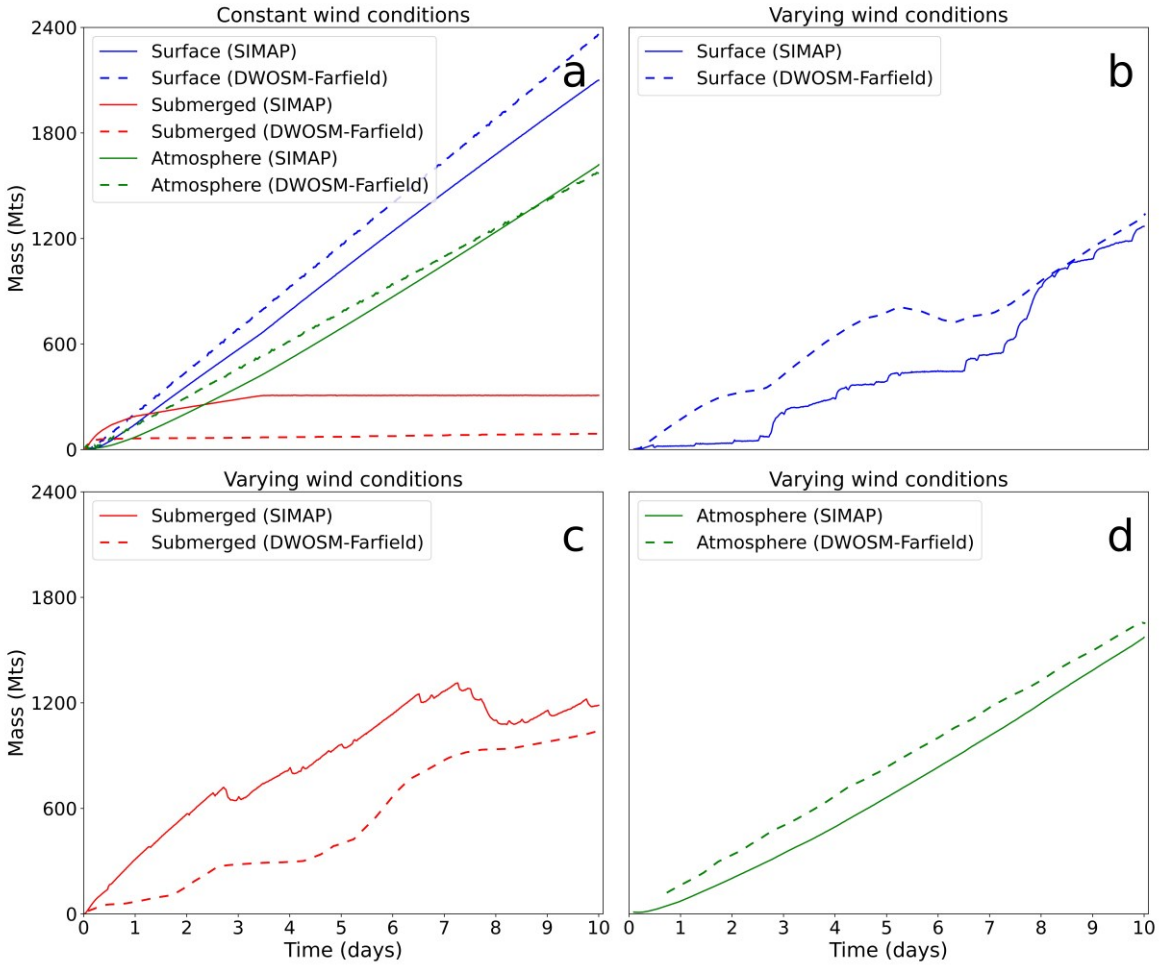

Figure 4-5 The mass balance from SIMAP and DWOSM-Farfield at ten days: a) under constant wind conditions; b) surface, c) submerged, and d) evaporated oil under varying wind conditions.

Cross-sections of the trajectories of subsurface droplets and surfaced oil under steady environmental fields illustrate that spill trajectory forecasts obtained from the two models are primarily consistent (Figure 4-6). Large oil droplets rise rapidly in the water column, and smaller droplets are progressively carried farther downstream by subsurface currents as they eventually reach the sea surface; afterward, the surfaced oil is deviated by the steady northeast wind and drifts toward the downwind direction without curvature. Multiple spill sources appear on the sea since oil droplets surface at different times and locations owing to their distinct rise

velocities. Those droplets from the smallest size bins move underwater for an extended time compared to large droplets, thus surfacing south away from the initial spill sources. The most significant difference in the spatial distribution of LEs is that the subsurface oil from SIMAP widely disseminates south, beyond the surface oil (Figure 4-6 c and e). It may be attributed to the following reasons: 1) the DSD predicted from the Vdrop-J has a minor fraction of microdroplets and is supplied to SIMAP simulation as input for the near-field modeling; 2) diffusion coefficients in SIMAP were assumed differently for above and below the depth of the surface mixed layer (pycnocline), allowing more intensive horizontal turbulent diffusion in the upper water column; 3) different algorithms are used to predict the rise velocity in the two models. In the SIMAP model, the rise velocities of small droplets (<1 mm) and large droplets ($\geqslant$1 mm) are calculated by Stokes' law and the method using the drag coefficient of ambient fluid, respectively. As described in section 3.5.2, this study applies empirical correlations proposed by Clift et al. (2005) to compute the terminal velocity of rising particles. Importantly, microdroplets from the SIMAP simulation have remarkably slower rise velocity than millimeter-scale droplets; hence, droplets tend to stay in the water column for an extended period and spread widely underwater. Nevertheless, those tiny oil droplets account for a negligible fraction of the total spill volume. Thus, the discrepancy between subsurface oil distributions from the two simulations is far less significant than what appears visually on trajectory mapping.

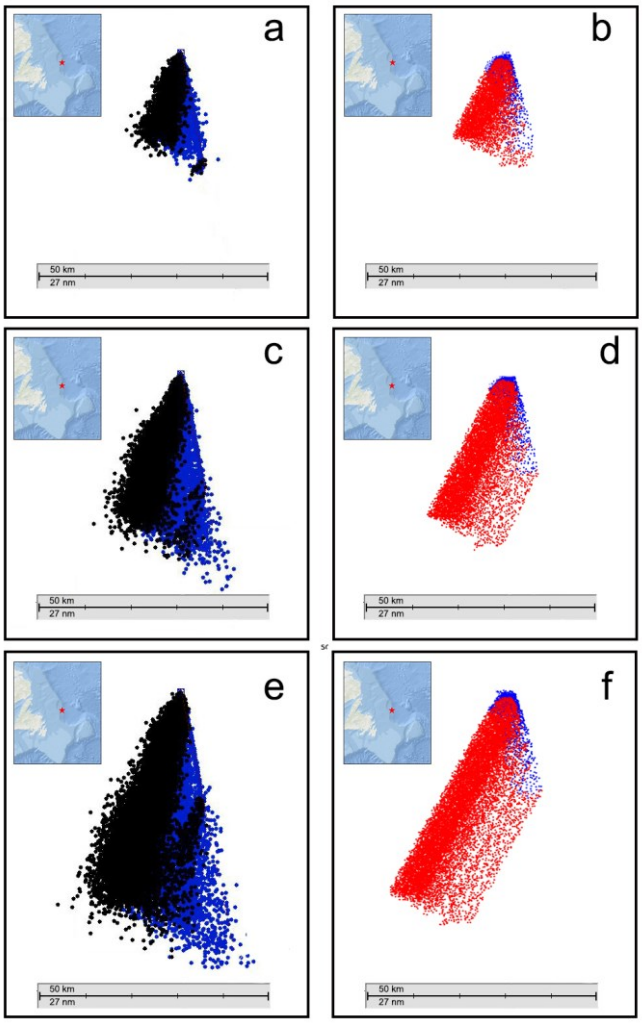

Figure 4-6 The oil trajectory from SIMAP (left panels, surface oil in black and subsurface oil droplets in deep blue) and DWOSM-Farfield (right panels, surface oil in red and subsurface oil droplets in deep blue): a-b) at four, c-d) seven, and e-f) ten days.

4.3.2.2. GNOME model

Snapshots of the oil distribution from GNOME and DWOSM-Farfield at three moments show that surface and subsurface oil trajectories predicted from the two models largely overlap and drift toward the same direction (Figures 4-7 and 4-8). The paths of rising droplets barely change with time as subsurface currents are close to steady flows (Figure 4-9). Initially, large oil droplets reach the sea surface within a half day, and both simulated slicks drift 50 km off

the east during the first two days and form an L-shaped oil band (Figures 4-7c and 4-8). The distance between the far end of the trajectory from DWOSM and the release point is slightly further than the results of GNOME. Afterward, surfaced oil stretches toward the southeast seven days after the spill, forming two bend-shaped films crossing 140 km from the release point to the end of the trajectory (Figures 4-7f and 4-8). The two predictions are consistent until a discrepancy appears at the far end of the oil slicks. Ten days later, oil stripes drift towards the south monolithically and have significant curvature caused by the south current and wind (Figure 4-9). They extend 160 km from north to south and 140 km from west to east (Figures 4-7i and 4-8). Similar to previous moments, most predicted trajectories overlap despite a few slicks distancing from the release point not matching well.

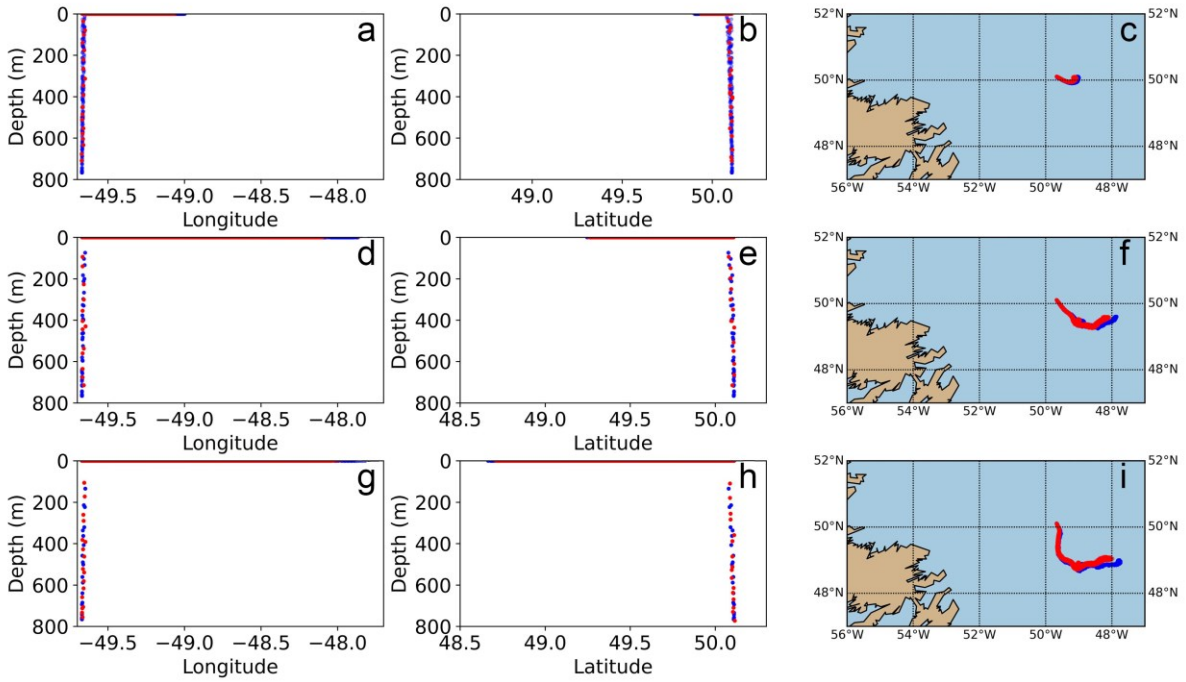

Figure 4-7 A comparison of oil trajectories between DWOSM-Farfield and GNOME simulations.

Note: The first row shows oil trajectories at two days (a - c); the second row is at seven days (d - f); the third row is at ten days (g - i). The first column denotes oil trajectories from the Longitude-Depth view

(a, d, g); the second is from the Latitude-Depth view (b, e, h); The third is from the Longitude-Latitude view (c, f, i) (DWOSM-Farfield in blue; GNOME in red).

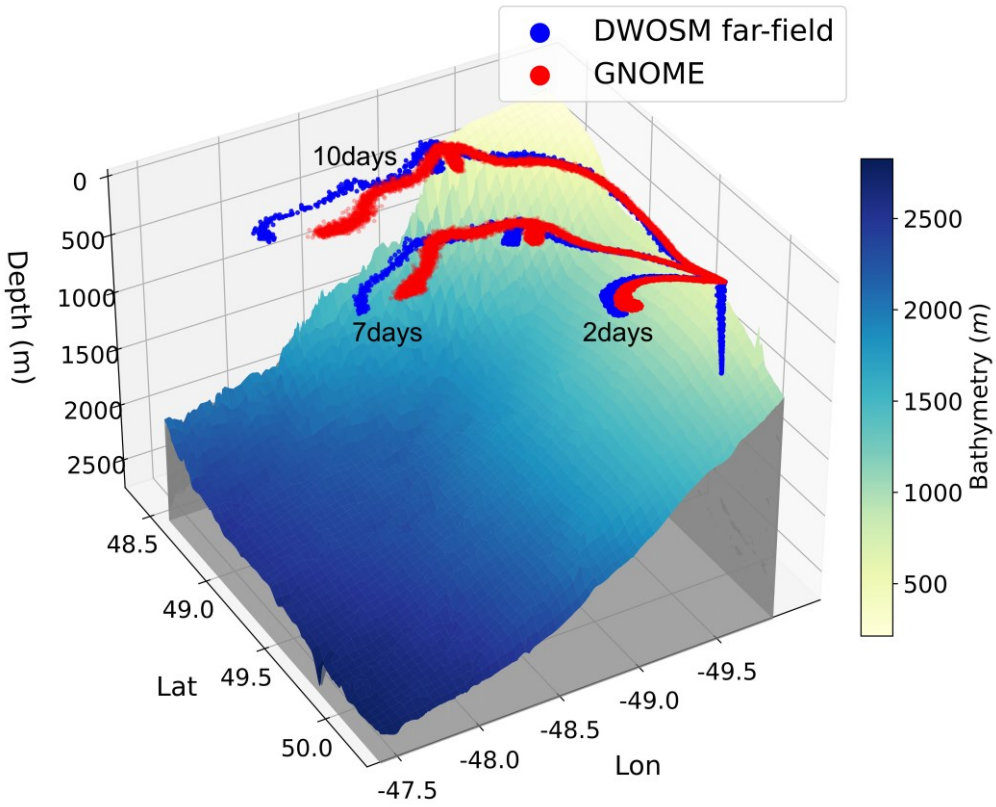

Figure 4-8 The bathymetry around the spill site and the 3D oil trajectories from DWOSM-Farfield at two, seven, and ten days.

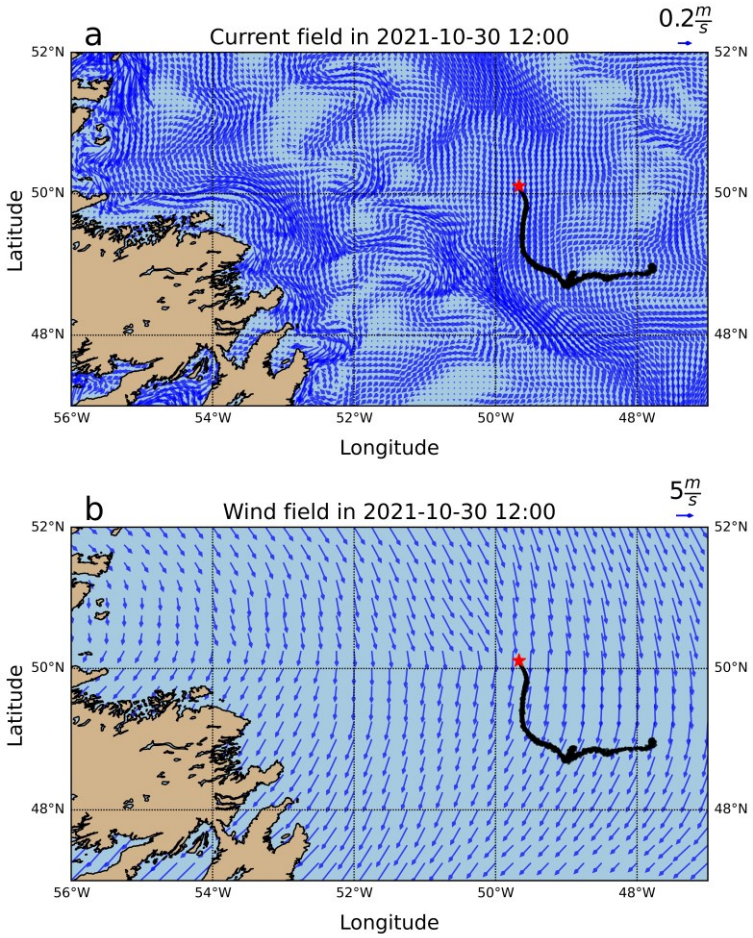

Figure 4-9 A snapshot of current and wind fields and the oil spill trajectory predicted from DWOSM-Farfield at 12:00, on 30 October 2021.

To qualify the difference between the simulation results, the output is visualized by histograms based on the spatial distribution of surfaced oil (Figure 4-10). It is obvious that the distributions of simulated slicks from the two models are generally close. The latitudinal ranges of predicted oil slick distribution from DWOSM are nearly 0.05◦ broader than from GNOME at two days (Figure 4-10a), basically equal at seven days (Figure 4-10b), and 0.05◦ more expansive at ten days (Figure 4-10c). Likewise, the longitudinal extents of DWOSM results are 0.05 wider than GNOME and 0.24◦ broader at seven and ten days. The difference in the trajectory prediction of the two models is mainly because of different methods to calculate the

rise velocity of oil droplets, which makes rising droplets take different pathways and have different timing to reach the sea surface.

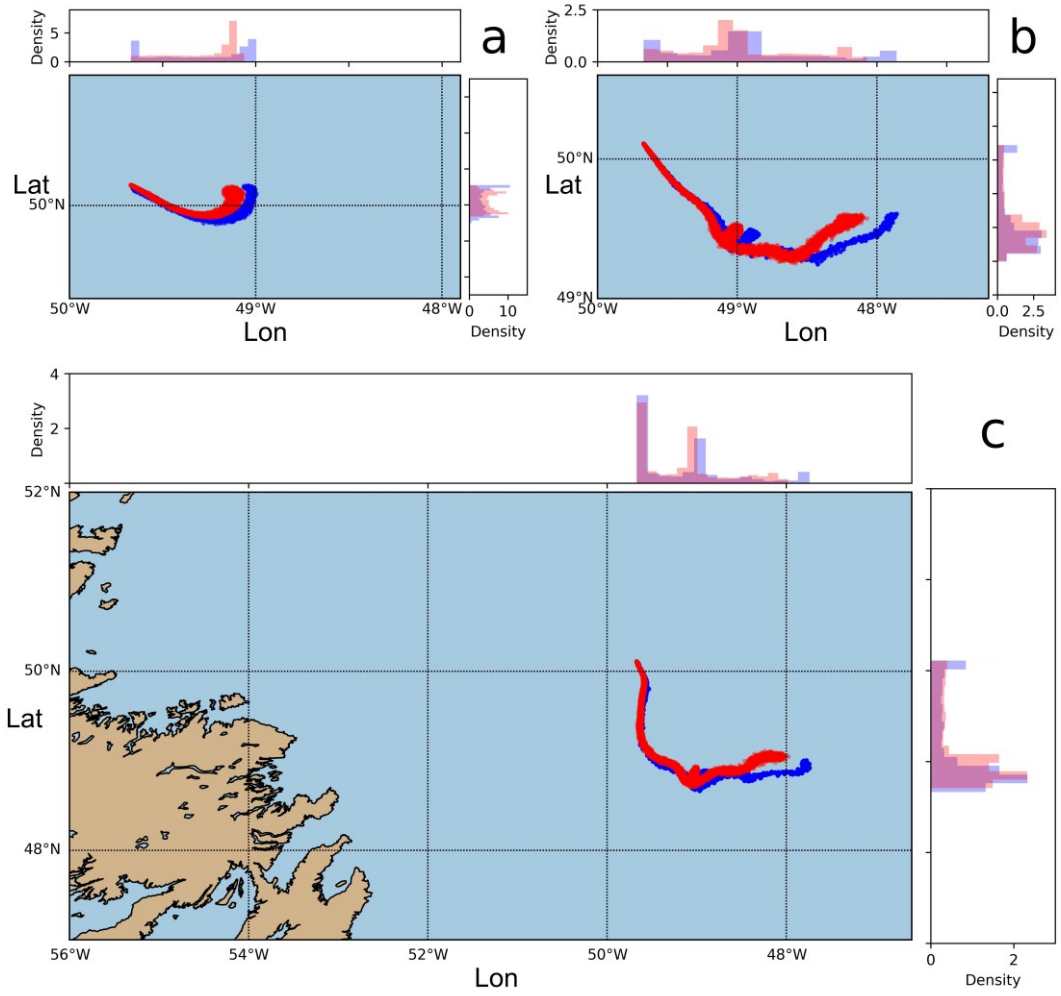

Figure 4-10 Distribution and histograms of simulated oil trajectories from GNOME and DWOSM-Farfield: a) at two, b) seven, c) ten days.

Note: The top and right sub-panels show the longitudinal and latitudinal distributions (DWOSM-Farfield in blue, GNOME in red).

4.3.3. Impacts of weathering processes on oil fate

The effects of weathering processes and changes in oil properties on spill mass balance are investigated by including or not those factors in modeling scenarios (Figure 4-11). As shown in Figure 4-11a, whether or not the emulsification is taken into account, there is little change

in the oil budget before the first five days. Subsequently, the lack of emulsification increases the subsurface oil mass by 141 Mts on average and marginally reduces the oil entering the air compared to the business-as-usual (BAU) scenario. The mass of surfaced oil begins to decline at the same period and decreases by 74 Mts at ten days. In contrast to a minor variation in mass balance brought by water uptake, evaporation and entrainment substantially alter the mass fraction of surface and subsurface oil (Figure 4-11 b and c). Without the involvement of the evaporation process, surfaced oil mass fluctuates severely and only remains at 526 Mts after ten days, roughly half of the value in the BAU scenario (Figure 4-11b). At the same time, submerged oil soars to 3,501 Mts under an evaporation-related scenario, 1,290 Mts greater than the level in the BAU scenario. More dramatically, excluding natural dispersion entirely reverses the proportion of mass distribution between surfaced and submerged oils (Figure 4-11c). Under the BAU scenario, submerged oil dominates the mass balance and rises to 2,211 Mts within ten days, while evaporated and surfaced oils maintain similar increasing trends and approximately account for less than half of subsurface oil. Once wave entrainment effects on slicks are ignored, surfaced and evaporated oils increase from 21.5 % (BAU) to 58.6 % and 23.6 % (BAU) to 39.0 %, respectively. Conversely, simulated oil mass drops from 54.9 % (BAU) to only 2.4 % in the water column. When oil properties remain unchanged in the fate modeling, a similar trend with the result of an emulsification-related scenario appears: the variation in oil properties does not initially change the mass balance (Figure 4-11a and d). It is also found that the variation caused by constant oil properties is slightly greater than that owing to emulsification.

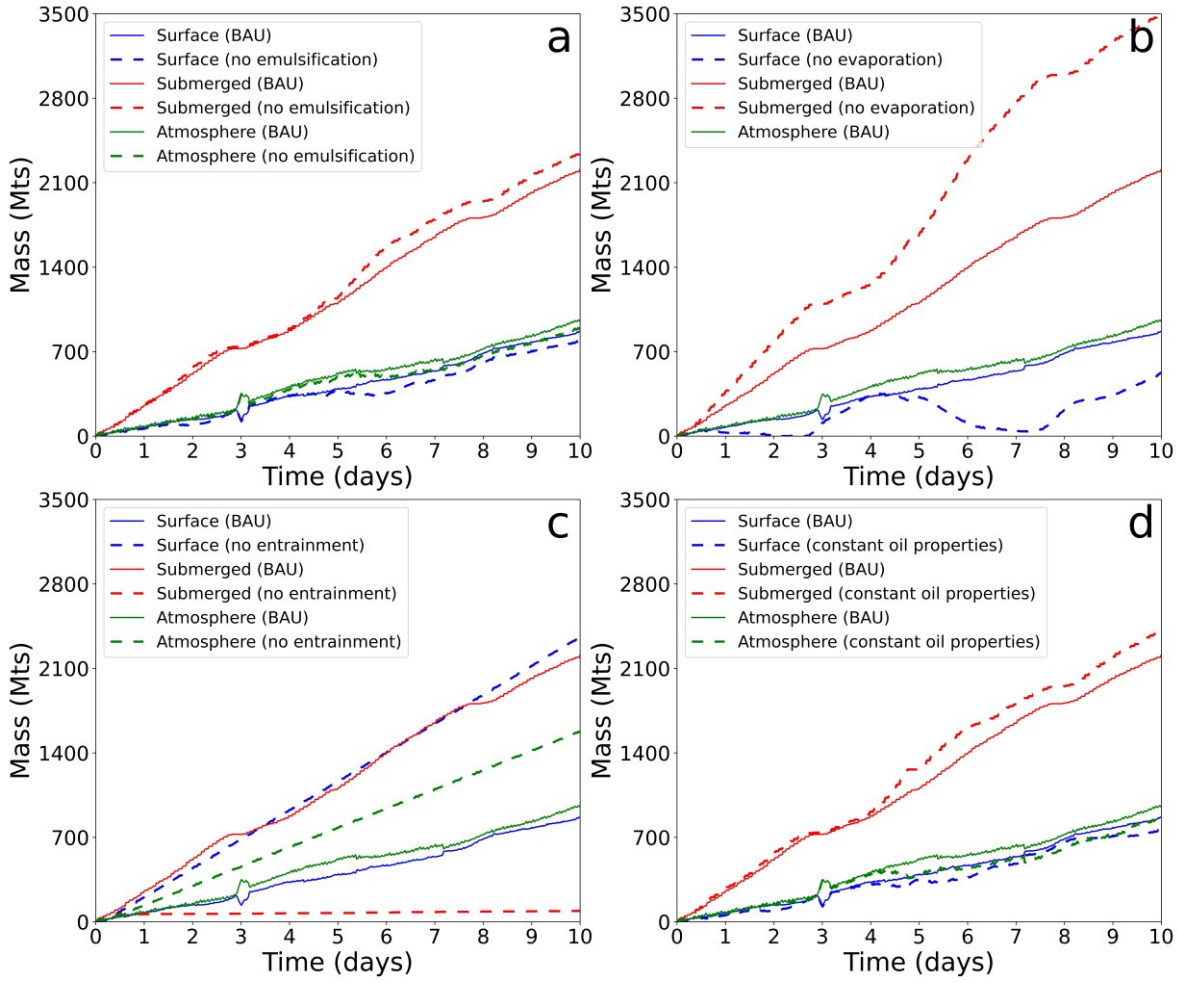

Figure 4-11 Effects of the absence or presence of various weathering processes and oil property variation on oil mass balance in DWOSM: a) emulsification, b) evaporation, c) entrainment, and d) oil viscosity and density.

Emulsification can substantially contribute to the volumetric increase in slicks, whereas the fate modeling of DWOSM only involves the mass of oil rather than the emulsion; therefore, the predicted slick mass does not change due to water uptake. Once no water-in-oil emulsion forms, more surface oil is transferred underwater as a low-viscosity slick is easier to disperse naturally (Figure 4-11a). As a consequence, the mass of evaporated hydrocarbons is also reduced when the exposed surface area of slicks decreases. Obviously, the change in the mass

balance owing to evaporation is more prominent than that caused by emulsification (Figure 4-11b). Compared with surface oil in the BAU scenario, it seems counterintuitive that its mass does not increase but falls by ignoring evaporation. The evaporative loss of volatiles in the oil mixture also makes weathered oil more viscous, impeding the natural dispersion of oil. In turn, not including evaporation decelerates the rise of oil viscosity, indirectly facilitating dispersion to entrain more surface oil into the water column. Due to the lack of evaporation, natural dispersion becomes the only primary process reducing surface oil. Meanwhile, high-speed winds prevail in the spill zone of this study case (Figure 4-9b), amplifying wave heights and the fraction of the sea surface covered with breaking waves. In addition to no evaporative loss in the exposed area of slicks, these factors jointly enhance the entrainment rate and thus allow natural dispersion to dominate the oil spill budget without evaporation.

Comparable mass balance trends are presented from the simulation results of the spill in the stable and weak-wind conditions (Figure 4-5a) and the no-entrainment scenario (Figure 4-11c). Wind speed plays a determining role in the dispersion algorithm since no entrainment occurs once it is lower than the threshold for onset of breaking waves. As natural dispersion is omitted, only a limited amount of dissolved hydrocarbons and droplet clouds ascending in the water column constitute submerged oil. Unlike soaring dispersed oil mass in the no-evaporation scenario (Figure 4-11b), evaporative loss of oil increases steadily (Figure 4-11c) because this process basically ceases as volatile components are gone. Furthermore, the simulation with constant oil properties provides a result close to the no-emulsification scenario (Figure 4-11 a and d). The reason is straightforward: non-weathered (scenario using constant properties) and less weathered (no-emulsification scenario) oils have a lower viscosity than weathered oil,

leading to less entrained surface oil and more dispersed oil. In summary, natural dispersion is the most impactful weathering process for the spill mass balance resulting from the DWOSM, followed by evaporation. It is worth noting that this conclusion is only valid for the specific spill scenario as the wind speed is exceptionally high, and the tested oil type is a light crude in the case study. A systematic sensitive analysis is required for more generalized conditions to obtain the importance of factors in model formulation despite a tremendous computational burden.

4.4. Summary

In this chapter, DWOSM is applied to a hypothetical blowout at 800 meters in eastern Newfoundland waters for model verification by comparing the integration of three OOSMs. Firstly, oil DSDs generated from a DWOSM-DSD are compared with experimental observations and outcomes from a PDM. It indicates that prediction in DWOSM-DSD primarily agrees with experimental and modeling results under different release conditions. Then, the comparison for spill trajectory shows considerable similarity in surface slicks under the constant wind and current fields. Specifically, the two models have the same drift direction, but underwater oil is less widely disseminated downstream in DWOSM simulations than SIMAP. The two models adopt different methods for the vertical velocity of oil droplets in the water column, resulting in different surfacing times and locations. Regarding oil mass balance, the two simulation results have similar trends: surface oil is predominant in spill mass balance under weak-wind conditions, and submerged oil prevails in high-speed winds. The discrepancy is that SIMAP's results have more oil mass in the water column since entrainment algorithms taken by the two models are distinct. Last, spill trajectories between DWOSM and GNOME

are compared to examine the validity of the simulation under actual environmental fields. Not surprisingly, the two predicted oil trajectories largely agreed due to the same algorithms for oil transport apart from rise velocity. In sum, the DWOSM performs well in modeling deepwater blowouts compared with other established toolkits, proving that the newly integrated system can forecast deep-sea spills and is all-inclusive for OSM on different scales and processes.

Chapter 5 Model Validation through a Hindcast of the DWH Blowout

5.1. Overview of the study site

The GOM is a semi-enclosed marginal sea situated in the west of the North Atlantic Ocean, which connects the tropical and North Atlantic and serves as the inception point for the North Atlantic's western boundary current, *i.e.*, the Gulf Stream (Liu, 2011). It possesses abundant oil and gas storage underneath the seafloor, rich fisheries resources in the water column, and valuable wetlands along the coast. The DWH was a semi-submersible offshore drilling rig at the Macondo Prospect (88.367°W, 28.740°N) in Mississippi Canyon Block 253 of the north-central GOM (Beyer *et al.*, 2016) (Figure 5-1). An explosion due to misconduct and blowout preventer failure occurred on the oil platform at around 7:45 pm center daylight time (CDT) on April 20, 2010. After a 36-hour fire, the charred superstructure collapsed and sank into the sea floor of 1,522 m at 10:22 (CDT) on April 22, 2010, resulting in the damaged riser pipe that connected the wellhead to the drilling platform. A large oil slick was observed at the former drilling site soon after the platform fell. During this unprecedented environmental catastrophe, an estimated 3.19 to 4.90 million barrels of crude oil, along with several hundred thousand tons of hydrocarbon gases, were released into the subsea until the damaged well was capped three months later (Shultz *et al.*, 2015; Beyer *et al.*, 2016). Various response activities were conducted to mitigate the negative impacts of this disastrous accident, such as in-situ burning, mechanical recovery, and surface dispersant application. It is worth noting that the chemical dispersant Corexit® 9500 was massively deployed for the first time during the deep-sea oil spill (Paris *et al.*, 2018). From the end of April to mid-July 2010, 771,000 gallons of dispersant

were intermittently injected at the Macondo Prospect wellhead to prevent the oil from rising to the sea surface (Kujawinski *et al.*, 2011; French-McCay, 2021a).

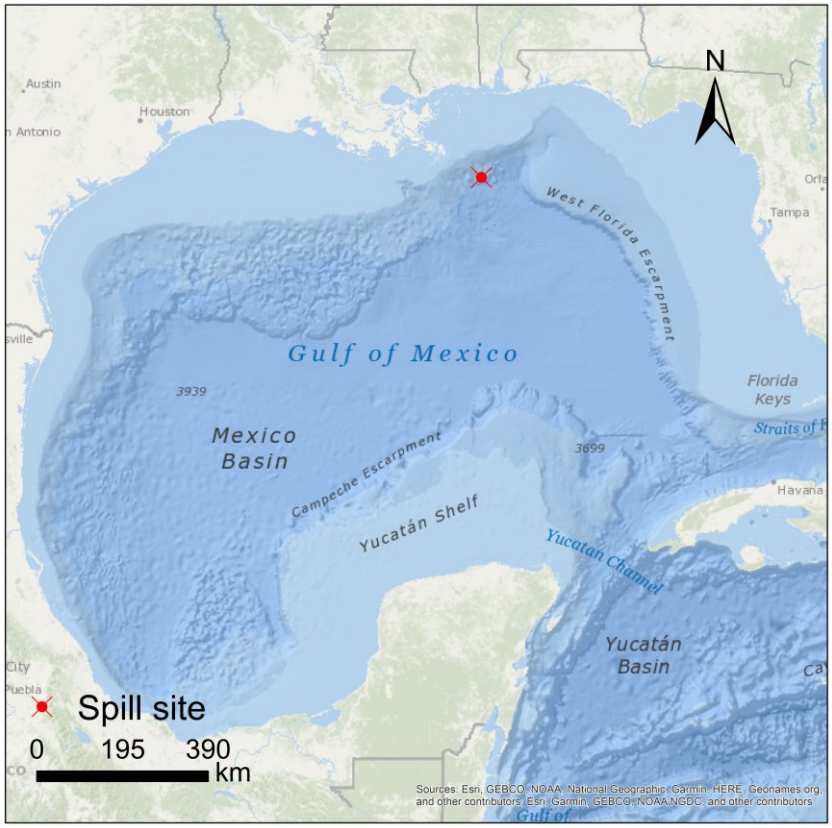

Figure 5-1 The location of the sunk DWH drilling rig.

5.2. Model configurations and data collection

The data supplied to this modeling effort mainly originate from reanalysis products generated by hydrodynamic and atmospheric models in tandem with oil spill information from other relevant studies. Some key model inputs and their related source can be found in Table E-1. Current and wind data are the two most crucial inputs for Lagrangian trajectory modeling as they jointly move drifting objects at the water surface. Several current and wind reanalyses are publicly available with varying temporospatial resolutions and coverages (French-McCay *et al.*, 2021b). This study selects the two freely accessible datasets with the finest resolution,

i.e., HYCOM + NCODA Gulf of Mexico 1/25° Reanalysis (accessible at https://tds.hycom.org/thredds/catalogs/GOMu0.04/expt_50.1.html?dataset=GOMu0.04-expt_50.1-2010 as of Feb 14, 2024) and 10-meter-elevation wind from ERA5 (accessible at https://cds.climate.copernicus.eu/cdsapp#!/dataset/reanalysis-era5-single-levels?tab=overview as of Feb 14, 2024). The former is tailored for GOM and generated from the HYbrid Coordinate Ocean Model (HYCOM), which has 1/25° spatial resolution and three hourly time steps. The latter stems from the fifth-generation European Centre for Medium-Range Weather Forecasts (ECMWF) reanalysis for the global climate, with 1/4° spatial resolution and hourly temporal resolution. Given the lack of DWH measurements for Conductivity, Temperature, and Depth (CTD) required by near-field modeling, the water column data is retrieved by interpolating related variables in the current reanalysis near the sunk rig. To forecast the locations of stranded oil on the coastline, a high-resolution geography database extracted through NOAA's GNOME Online Oceanographic Data Server (accessible at https://gnome.orr.noaa.gov/goods/tools/GSHHS/coast_subset as of Feb 14, 2024) is used to define the boundary of the computational domain. The daily averages of GOR and oil flow rate are adopted for brevity despite the GOR and the flow rate of the damaged wellhead fluctuating during the DWH (McNutt *et al.*, 2012; Reddy *et al.*, 2012). Oil information fed into the fate algorithms comes from the ADIOS Oil Database. SSDI, a response technology for preventing subsurface oil from reaching the sea surface, was applied to a major blowout for the first time and began at the end of April (Ramírez-León, 2012). A ten-fold reduction in IFT for treated oil and gas is employed in this model configuration to mimic the effectiveness of SSDI (Zhao *et al.*, 2015). The gas-water IFT presumably cannot be reduced below 40 mN/m (Kashefi *et al.*,

2016). Rest input data and model configuration referred to previous studies and modeling investigations (Table E-1). It is worth noting that only the first two weeks of the DWH are simulated instead of the entire three months. Large-scale response activities were implemented a few days after the spill; for instance, aerial dispersant applications started on April 25, and in-situ burning began on May 5 (Boufadel *et al.*, 2021). They artificially changed the oil trajectory and mass balance, whereas most information about the consequences of mitigation events remains unknown. This study only conducts a short-term hindcast to minimize the uncertainties in OSM.

This study mainly compares six primary outputs from the DWOSM hindcast with remote sensing-based estimates, field measurements, and previous modeling works (Table 5-1). Knowing the overall DSD is crucial to evaluating the transport and fate of oil droplets and gas bubbles following a subsea spill. In practice, only a local DSD is measurable for a deepwater blowout, which will likely cause overestimating or underestimating the overall DSD based on the measurement location (Daskiran *et al.*, 2021). A few distributions were observed through the two dives at a water depth of 702-1,198 m during the M/V Jack Fitz 3 (JF3) cruise in mid-June 2010 (Davis and Loomis, 2014). Since the absence of DSD measurements through the DWH incident (Zhao *et al.*, 2015), the oil/gas DSD result is validated by comparing hindcast results with other simulations and a few observed median droplet diameters and local DSDs. Detailed airborne chemical measurements conducted by Ryerson *et al.* (2012) during the DWH are used to examine whether the modeled gaseous hydrocarbon mass reaching the sea surface agrees with observation. Comparatively, verifying surface oil location is the most achievable task in validating the oil spill model results because satellite imagery data provides reliable

information about the spatial distribution of slicks over a period. A daily compilation of texture-classifying neural network algorithm (TCNNA) outputs generated from Synthetic Aperture Radar (SAR) images collected from the DWH is used to validate modeled surface oil trajectories (accessible at https://response.restoration.noaa.gov/gulf-mexico-erma as of Feb 14, 2024). Considering the short simulation time and the limitation of DWOSM, only the vertical distribution of the intrusion layer is compared with the detected extent of the deep plume, as the horizontal scale (tens of kilometers) of trapped subsurface plumes greatly exceeded the vertical scale (~100 m) (Camilli *et al.*, 2010; Hazen *et al.*, 2010). Shortly after the DWH spill, large-scale field surveys are conducted through the Shoreline Cleanup Assessment Techniques (SCAT) to collect data on coastline oiling conditions (Santner *et al.*, 2011). It can offer helpful information for verifying the modeled distribution and timing of beached oil. Research related to validating the simulated oil fate is challenging because of a scarcity of accurate observations that quantitatively depict the amount of released oil distributed in each environmental compartment (*i.e.*, sea surface, water column, shore, and atmosphere). Only some remote sensing-based estimates of surface oil volume derived from satellite-borne sensor data are found, including SAR, MODIS Visible, and MODIS Thermal Infrared Sensor (TIR) (French-McCay *et al.*, 2021a and b). The rest of the hindcasts of oil fate in DWOSM are compared with simulation results from the SIMAP.

Table 5-1 The information used for the validation of DWH hindcast.

Modeled objects	Validation data	Description
Oil and gas DSDs	Simulations of oil/gas DSD and observed volume median droplet diameter from related studies	Simulations from Zhao *et al.* (2014 and 2015), Spaulding *et al.* (2017); observational data from Davis and Loomis, (2014), Spaulding *et al.* (2017), and French-McCay *et al.* (2021b).
Chemical composition of surfaced bubbles	Simulations and airborne atmospheric chemical data	Gros *et al.* (2017) made TAMOC simulations for the DWH blowout; airborne chemical measurements were obtained by Ryerson *et al.* (2012) in May and June 2010.
Surface oil distribution	TCNNA SAR Potential Oiling Footprints	This product was created from surface anomalies identified from satellite-borne SAR using a TCNNA (Garcia-Pineda *et al.*, 2013).
Subsurface plume and intrusion layer	Observation from related studies	Underwater measurements from Camilli *et al.* (2010) and Hazen *et al.* (2010).
Stranded oil locations	Mobile SCAT maximum oiling	Field observations obtained by SCAT (accessible at https://erma.noaa.gov/gulfofmexico as of Feb 14, 2024)
Oil mass budget	Hindcast from related studies and remote sensing-based estimates of surface oil volume	Simulated mass balance from French-McCay *et al.* (2021a and b).

5.3. Selection of error metrics for spill trajectory modeling

As the most important output of OSM, the accuracy of spill trajectory forecast must be demonstrated through a good performance mirrored by error metrics instead of only a simple visual comparison. Three error measures suitable for validating Lagrangian model output against satellite imagery are selected here to quantitatively evaluate the performance of spill trajectory modeling from different perspectives, including the centroid skill score, the area skill score, and a 2D measure of effectiveness (2D-MOE) (Dearden *et al.*, 2021).

The centroid skill score is designed to indicate how close the predicted oil trajectory is to the observed spill region. First, the spatial difference between the geometric centers of observed

and modeled trajectories is gauged by a centroid displacement index C_I below:

$$C_I = \frac{\Delta x}{L_{OBS}} \tag{5-1}$$

where Δx is the distance between the centroids of the observed slick and the predicted oil at a given moment, and L_{OBS} is the length scale of the observed spill area. Specifically, L_{OBS} is the distance along the diagonal of a bounding box enclosing the observed oil-contaminated waters. In short, C_I measures the absolute error in the predicted centroid location, normalized by the length scale of the observed oil geometry.

The centroid skill score C_{SS} can then be defined based on C_I as:

$$C_{SS} = \begin{cases} 1 - \frac{C_I}{C_T}, & C_I < C_T \\ 0, & C_I \geq C_T \end{cases} \tag{5-2}$$

where C_T is a user-selected tolerance threshold. A C_T value equaling one means that a comparison has any skill score only when the distance between the locations of the observed and predicted centroids must not exceed the magnitude of the observed length scale. A C_{SS} of one corresponds to perfect overlap between observed and predicted centroids, whereas zero indicates no "skill".

The area skill score is tailored to complement the weakness of the centroid skill score by measuring the size of the predicted spill area relative to the observed region. The area index A_I is introduced in a manner analogous to C_I below:

$$A_I = \frac{|A_{PR} - A_{OBS}|}{A_{OBS}} \tag{5-3}$$

which is the normalized magnitude of the difference between predicted and observed slick areas at a given moment.

The area skill score A_{SS} is then defined based on A_I as

$$A_{SS} = \begin{cases} 1 - \frac{A_I}{A_T}, & A_I < A_T \\ 0, & A_I \geq A_T \end{cases} \quad (5\text{-}4)$$

where A_T is a user-selected tolerance threshold. Similarly, an A_T value of one implies that the error in the predicted area should range within the magnitude of the observed spill area; otherwise, it equals zero. An A_{SS} of one means a perfect agreement between predicted and observed areas.

As A_{SS} does not involve any discrepancy in the shape of the predicted spill trajectory relative to the observation, a 2D-MOE is used to measure how much the modeled area overlaps with observations. It is expressed as:

$$MOE = (x, y) = \left(\frac{A_{OV}}{A_{OB}}, \frac{A_{OV}}{A_{PR}}\right) = (1 - \frac{A_{FN}}{A_{OB}}, 1 - \frac{A_{FP}}{A_{PR}}) \quad (5\text{-}5)$$

where A_{OV} is the overlap between observations and predictions; A_{OB} and A_{PR} are observed and predicted slick areas, respectively. A_{FN} is the false negative (the area where oil appears but is not predicted), and A_{FP} is the false positive (the region where oil is predicted but neglected). A perfect 2D-MOE score of $(x, y) = (1,1)$ represents a complete overlap between observations and predictions. A value of x close to one and y close to zero indicates that the result has a significant false positive (*i.e.*, the spill coverage is overestimated). Conversely, a low x value with a high y value shows the predominant false negative led by underestimating the oil spill region.

Likewise, the 2D-MOE also has a limitation as the agreement regarding the spill size and shape is not considered. This could result in low or even zero MOE values, especially when the two trajectories are in close proximity but have less overlap. A poor performance will be unnecessarily indicated for forecast cases with little or no overlap caused by a minor offset despite the simulation accurately capturing the shape and size of observed slicks (Dearden *et*

al., 2021). As in this study, such misleading results can be minimized by complementing C_{SS} and A_{SS} into adopted error metrics.

5.4. Results and discussion

5.4.1. Oil/gas droplet size distribution

DWOSM-DSD module provides the hindcast of the VMD of untreated oil as 3.24 mm. Its DSD yielded from the Rosin-Rammler distribution fitting indicates that the oil droplet size ranges from 0.46 to 10.06 mm before applying dispersants (April 22 to 29) (Figure 5-2a). Droplet sizes in the VDROP-J simulations vary from 1.01 to 7.94 mm, with a median of 3.85 mm marginally greater than the size of VDM from this hindcast. Two studies produce close simulation results of VMD of oil droplets despite adopting distinct initial setups and modeling approaches. A comparatively apparent discrepancy yet appears in the gas DSD: bubble sizes given by DWOSM-DSD are somewhat evenly distributed in size bins from 3.01 to 17.96 mm; in the study of Zhao *et al.* (2014), over 73% of gas bubbles had diameters ranging from 7.60 to 10.06 mm, and the rest were within 1.46 to 7.60 mm (Figure 5-2b). Unlike the steady VMD provided by an EM, Zhao *et al.* (2014) used a PDM, VDROP-J, to predict the DSD of droplets/bubbles 200 m away from the wellhead. Relatively high IFT at the seawater-gas interface allows less turbulent breakup, resulting in gas bubbles with a larger diameter than oil droplets and increased volume fractions corresponding to larger bubbles (Gros *et al.*, 2017; Zhao *et al.*, 2017).

All the modeled oil/gas DSDs decrease significantly after SSDI application, and their VMDs are reduced by a factor of 2 to 3 on average (Figures 5-2c and d). DWOSM and VDROP-J simulations generate close cumulative distribution functions (CDFs) of oil droplet sizes and

nearly identical VMD. In contrast, a bimodal DSD from Spaulding *et al.* (2017) had a dual peak at 0.16 and 2.50 mm, presenting a curve of CDF with an obvious inflection point around 0.16 mm. The two peaks in DSD were led by the partial treatment of the riser release: one represents smaller chemically dispersed droplets, and the other refers to larger untreated droplets. Compared with Holocam measurements from the two dives, all three simulations yield oil droplet sizes over an order of magnitude larger, especially for the VDROP-J result that is entirely even out of the observed size range (Figure 5-2c). The VMD for the dives was reported to range from 0.07 to 0.25 mm, which differs from multiple observations that most surfaced droplets were millimeter-sized even after applying SSDI (Ryerson *et al.*, 2012; Reddy *et al.*, 2012; French-McCay, 2021 a and b). Large-sized oil droplets rising rapidly in the water column were not captured by deep dives, thereby obtaining a local DSD with a substantially smaller size range than those modeled overall DSDs. Among three simulations, the VMD from the bimodal DSD is closer to the in-situ measurement of median droplet diameters (~2-3 mm) from the riser pipe (French-McCay *et al.*, 2021b). Nonetheless, VMDs of treated oil from DWOSM-DSD and VDROP-J (~1.31 mm) are also an acceptable approximation (absolute error of 0.69-1.69 mm) from the perspective of operational response. The sizes of chemically dispersed gas bubbles range from 1.88 to 6.37 mm with VDMs of 3.72 mm from DWOSM-DSD and 2.60 mm for VDROP-J outputs (Figure 5-2d), which are generally agreed regarding the trend of CDFs. A threshold of minimal gas-water IFT adopted in this study enables an extended size range compared to VDROP-J simulations.

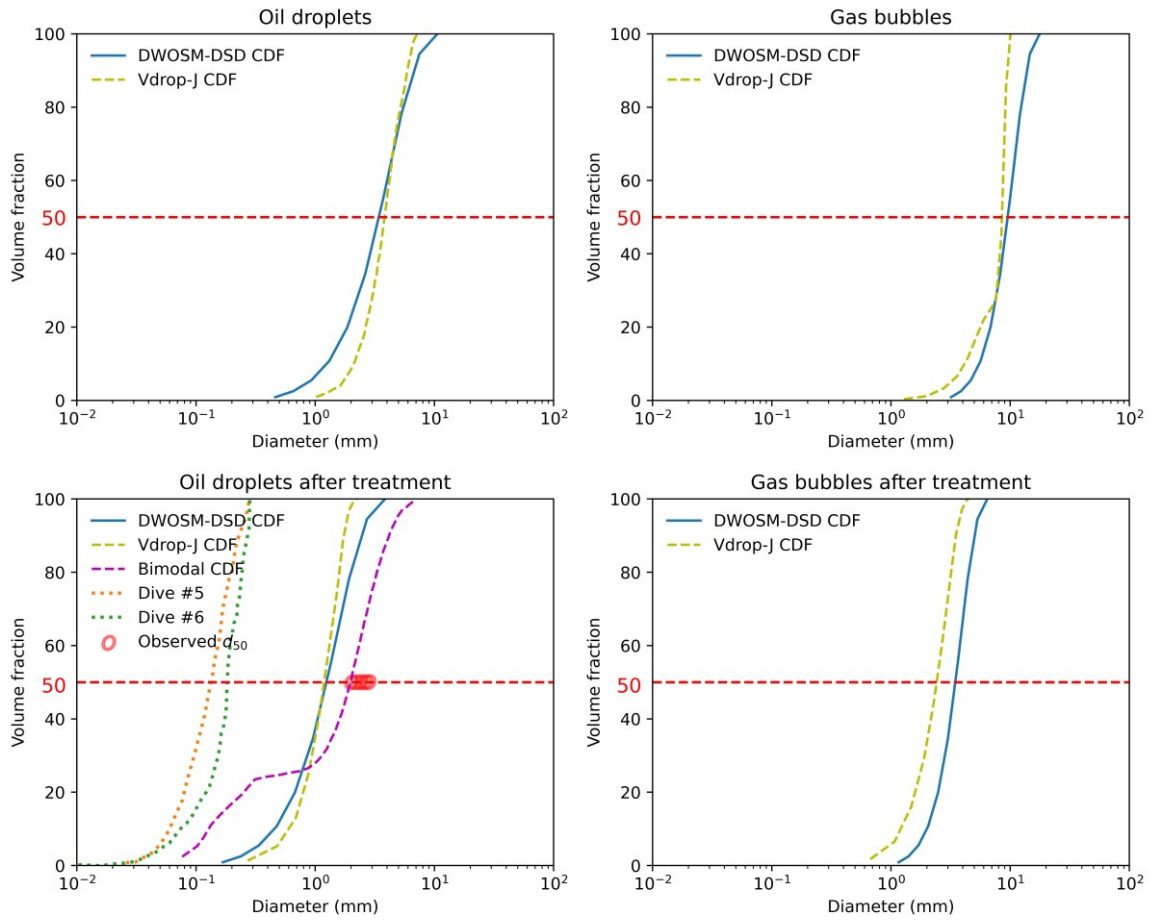

Figure 5-2 Comparison of the cumulative volume size distributions of untreated a) oil and b) gas, treated c) oil and d) gas.

Note: The red line represents 50% of the volume fraction; the VDM can be found in the x-coordinate of the intersection between a curve of CDF and the red line; the CDF at 200 m downstream distance in Vdrop-J simulations is derived from Zhao *et al.* (2014); bimodal CDF is from Spaulding *et al.* (2017); observations from the two dives (#5 and #6) in the Holocam measurements during the JF3 cruise.

Incomplete records of oil/gas overall DSDs before and after dispersant treatment challenge the validation of the hindcast of the DWH spill (Zhao *et al.*, 2015). Nevertheless, considering a minor discrepancy between modeled VMDs and field measurement, we surmise that the DSD hindcast from DWOSM-DSD is adequate to characterize the size distribution of spilled

petroleum fluids and further serve as the input of subsequent simulation. On the other hand, microdroplets (<100 μm) generated by the turbulent release constituted the deepwater intrusion layers. The smallest droplet size in this study is still larger than a typical microdroplet but is smaller than the minimal binned size in VDROP-J results, irrespective of applying SSDI. Hence, oil DSDs yielded from DWOSM-DSD may be more representative than the result of VDROP-J.

5.4.2. Plume trajectory and intrusion height

Figure 5-3 shows the plume region and its centerline provided by the DWOSM-Nearfield. The buoyant plume ascended to the water depth of 1,046 meters and then descended to 1,106 meters with a radius of 99.2 meters as its momentum and buoyancy dissipated. The location where the plume trajectory eventually ceases is approximated as the trap height and the width of the plume element at the final simulation step as the extent of the dominant intrusion layer. Two observational records of the DWH deep plume are found: Hazen *et al.* (2010) detected a deep-sea oil plume from 1,099 to 1,219 m at distances of 10 km from the wellhead from 25 May to 2 June 2010; Camilli *et al.* (2010) indicated the presence of a continuous plume of oil, over 35 kilometers in length, at approximately 1,100 meters depth during 23-27 June 2010. The modeled heights of stable intrusion layers appear from 1,000 to 1,197 m, close to an observed primary deep intrusion height with a relative error of 2.49% (Hazen's data) and 0.18% (Camilli's data). Although the time corresponding to the near-field simulation is inconsistent with when a deep plume was detected, most of the microdroplets and dissolved-phase hydrocarbons retained in the intrusion layer barely move vertically in contrast to their significant horizontal movement. It is mirrored well by the limited change in the two plume

center heights within a nearly one-month interval and a huge length-to-width ratio of the detected intrusion. A trap height of 1,015 meters modeled by French-McCay *et al.* (2018) was slightly shallower than in this study, likely due to ignoring the reduced momentum caused by particles exiting from the plume region. Secondary shallower intrusions (800-300 m) are omitted because the DWOSM-Nearfield cannot predict multiple trapping depths (Spier *et al.*, 2013). Yet, a reasonable quantitative estimate of the trap height and diameter of the near-field intrusion is provided in response to the DWH. Furthermore, the modeled plume orientation agrees well with the forensic assessment result of the deep plume with movement to the southwest (Driskell and Payne, 2018; Payne and Driskell, 2018). Since the plume and dispersed-phase particles in the near field will not be further tracked in DWOSM-Farfield once the momentum is neutralized, some measurements obtained from several kilometers off the wellhead, such as water-soluble compound concentration (Reddy *et al.*, 2012; Ryerson *et al.*, 2012), are inappropriate for validating the results from this study. In future research, we will attempt to adjust the formulation of DWOSM to simulate the concentrations of different hydrocarbons in the deep plume.

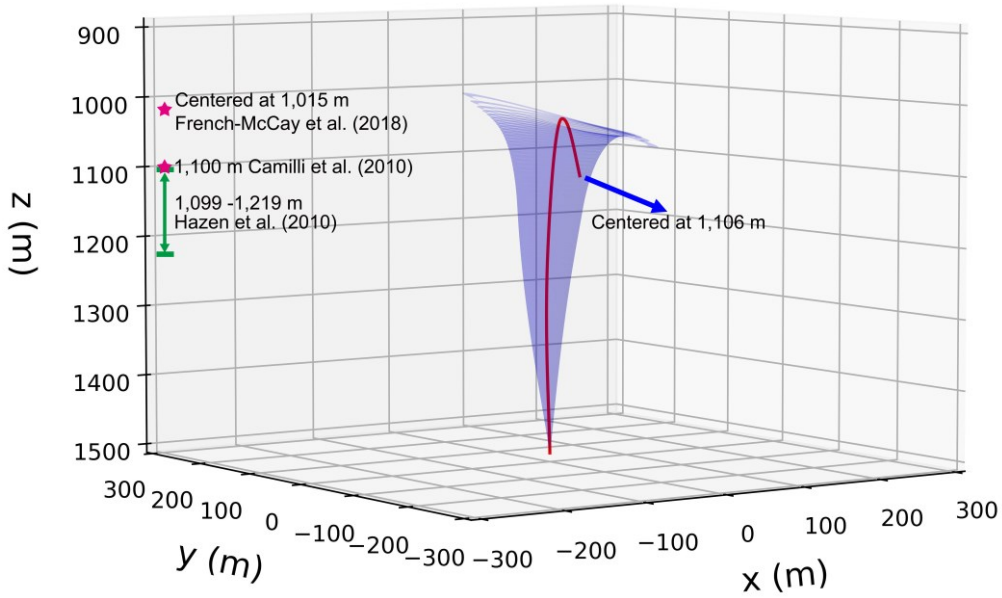

Figure 5-3 The 3D trajectory of the modeled near-field plume from DWOSM-Nearfield.

Note: The red line represents the centerline of the buoyant plume; the shaded blue area denotes the near-field plume region.

5.4.3. Surfacing gas bubble composition

As gas bubbles released from the deep-sea blowout rise in the water column, a substantial mass fraction of low molecular weight hydrocarbons dissolve into the ambient environment and eventually do not reach the sea surface (Figure 5-4). No methane and ethane occur in the modeled chemical composition of surfaced bubbles, consistent with airborne measurements during the DWH spill (Ryerson *et al.*, 2012). Observed petroleum compounds with heavier molecular weight have an increasing mass percent in surfaced fluid particles, fitting with the rule of thumb for hydrocarbon aqueous solubility. The propane and isobutane mass fractions in the DWOSM output are remarkably close to field observations, with a mean absolute error of less than 1.1%. TAMOC and DWOSM simulations somewhat underestimate the remaining percent of n-butane on the sea surface, having absolute errors of 12.2% and 10.0%, respectively.

This is probably due to an overestimated aqueous solubility of n-butane in thermodynamic modeling. The detected composition of surfaced bubbles and simulation results jointly reveal that primary gaseous hydrocarbons (mainly methane) in rising bubbles were dissolved in ambient water instead of entering the atmosphere during the DWH incident.

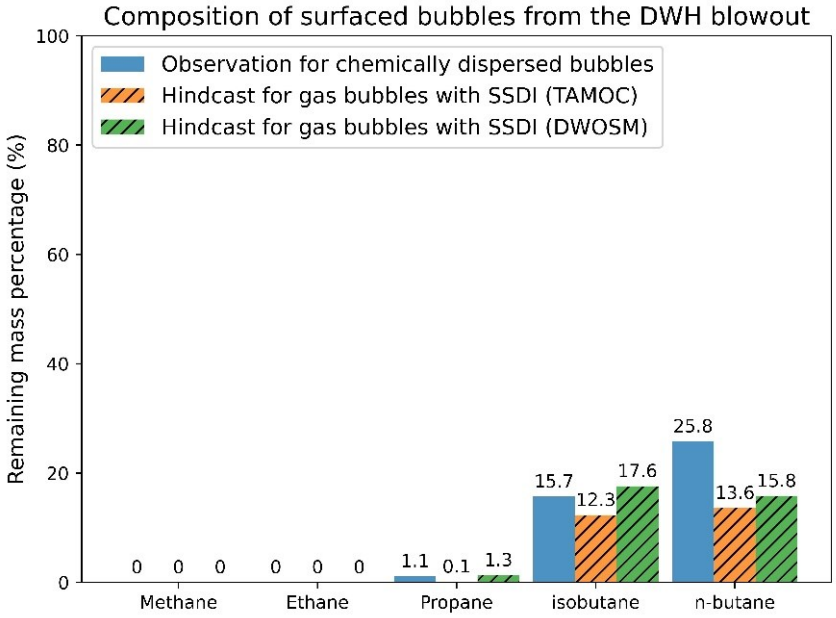

Figure 5-4 Comparison between modeled and observed mass fractions of primary hydrocarbons in surfaced gas bubbles during the DWH blowout.

Note: TAMOC simulations originated from Gros *et al.* (2017); observation is based on airborne measurement by Ryerson *et al.* (2012).

A mass distribution diagram along the water column is approximated by superimposing the relations between the remaining mass fraction of each hydrocarbon in different-size bubbles and their corresponding water depth (Figure 5-5). At the same height, the shaded area adjacent to the red line represents the lingering mass percentage in smaller bubbles with a higher surface-area-to-volume ratio; the region closer to the green line suggests the residual fraction

in larger bubbles. The wide range of remaining mass fractions at most heights demonstrates the importance of particle size to the fate of petroleum fluids released from the deepwater spill. Gaseous compounds with heavier molecular weight appear to have an increasing chance of reaching the sea surface. Methane and ethane in tiny bubbles almost dissolve off around 1,000 m as a higher surface-area-to-volume ratio leads to a faster dissolution rate, while larger bubbles still could transport a small amount of them from the wellhead to near the sea surface. A few propane in microbubbles become wholly dissolved around 834 m; most fractions are transferred into the higher water column (100-800 m depth) and rapidly disperse in the upper 200 m. Unlike faster dissolution rates of other major components, C4 hydrocarbons can be carried by even the minimal bubbles to the upper water column. The remaining fractions of isobutane and n-butane reach over 60% in some surfaced bubbles and average 16.7% for the total released butane. Despite a minor proportion of butane in natural gas, it still may cause toxicological impacts (*e.g.,* asphyxia and cardiac toxicities) on responder personnel exposed to gaseous butane (Vahabzadeh and Megarbane, 2022). Nonetheless, simulation results indicate that the mass of surfaced natural gas components (~0.03% of the released gaseous hydrocarbons) was limited during the first two weeks after the spill. Compared with field measurements that almost methane and ethane and 78% of propane dissolved below 1,100 m (Reddy *et al.*, 2012), the hindcast from DWOSM has less dissolved gaseous fractions, *i.e.*, 61% of methane, 46% of ethane, and 24% of propane. Fluid particles in subsurface plume samples obtained from intrusion layers in June 2010 were mainly dissolved and typically within a micrometer scale. The minimum bubble size modeled by DWOSM-DSD is around 0.2 mm even with treatment and less likely to be trapped in the deepwater plume. Hence, this diagram

is more representative of hydrocarbon mass distribution for millimeter-scale bubbles at various depths.

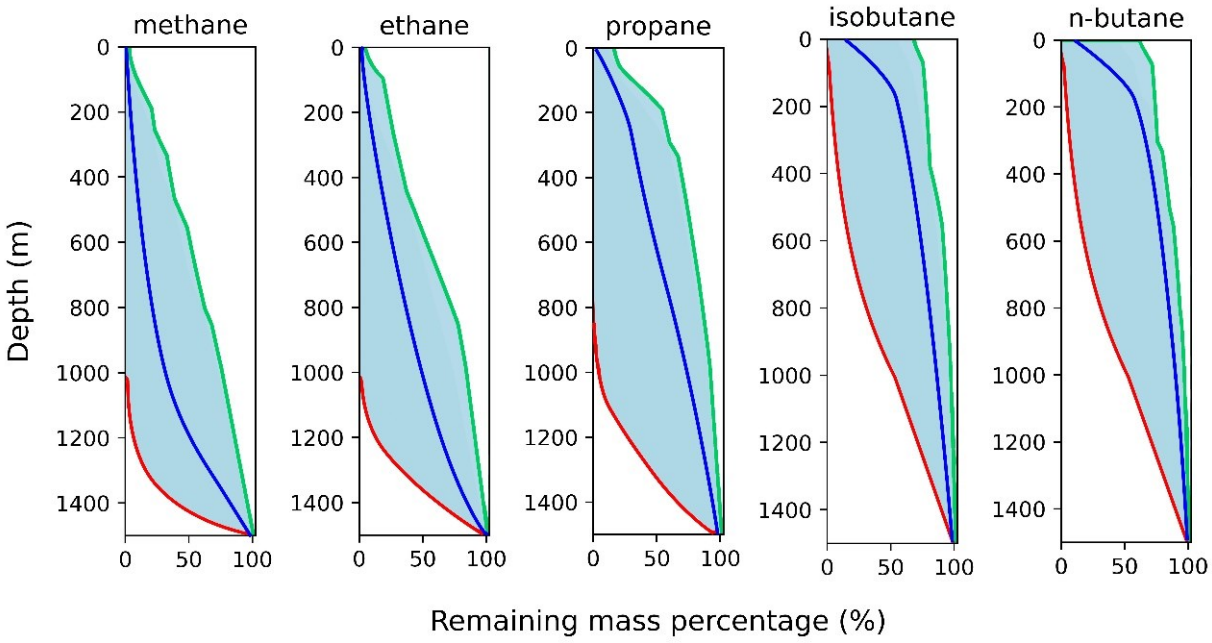

Figure 5-5 The vertical distribution of the remaining mass fraction of primary hydrocarbons in gas bubbles along the water depth from 22 April to 6 May 2010.

Note: The boundary of the shaded area represents the extremum (maximum in the green line and minimum in the red line) of the remaining mass fraction in different-size bubbles at a specific water depth. Blue curves are the mean remaining mass fractions derived from the weighted sum of the volume fraction of each bubble.

5.4.4. Oil spill trajectory

First, a direct comparison between modeled surface oil trajectories and TCNNA outputs in various moments shows a good agreement in terms of spatial distribution (Figure 5-6). Five days after the blowout, a C-shaped oil slick extending 90.4 km east-northeastward from the sunk rig appeared on the water area of 1,558.9 km^2 around 140 km off the coast of Alabama and Mississippi (Figure 5-6a). Local wind measurements and sea surface height records

revealed that three days of northwest winds and anticyclonic eddies to the east jointly determined the slick motion (Liu *et al.*, 2013). Surface oil in DWOSM simulations drifts along the same orientation with observed slicks but does not coincide at the far end, as no significant curvature appears in the modeled trajectory. On April 26, 2010, at 10:85 (CDT), scattered slicks with 2,970.9 km^2 did not move away from the spill site and stretched along the east-west direction with 126.5 km (Figure 5-6b). Wind direction shifting from west to north from April 25 to 26 prevented oil from drifting shoreward (Figure 5-7). Compared with the previous hindcast, the modeled trajectory also appears to elongate horizontally but with a lesser lateral extension of 42.3 km than detected. On April 29, 2010, at 07:09 (CDT), nearly ten thousand square kilometers of nearshore waters close to Garden Island Bay were covered by a vast and unshattered oil patch (Figure 5-6c). Less intensive winds after April 28 allowed a large area of slicks to remain on the sea surface without being dispersed by waves. Southward and southeastward winds were prevalent above oil-infested waters from April 26 to 29 (Figure 5-7), which makes it hard to explain why slicks approached the Mississippi River Delta (MRD) in the past three days. Such motion was likely due to Ekman effects resulting from the impacts of southward and southwestward winds (Liu *et al.*, 2013). A spatial consistency is mirrored by a large overlaid area between the two trajectories despite a prediction miss of 2,497.9 km^2 of oil-covered waters on the west of the release site. At the beginning of May 2010, floating oil became sporadic and formed an inverse triangular-shaped slick with a coverage of 4,479.1 km^2 (Fig. 5d). Amplified northwest winds after April 29 could be one of the causes of shattered surface oil (Figure 5-7). The simulated trajectory is in general agreement with observations; however, clustered particles poorly reflect the discontinuity of detected oil and are closer to the

coastline of the northern Gulf. A Lagrangian approach can only predict the presence or absence of oil, whereas it is hard to visualize the slick thickness satisfactorily. The LEs contact north of the MRD around this time, where the DWH oil was first stranded (Liu *et al.*, 2013). On May 3, 2010, at 18:57 (CDT), surface oil was shaped into a bent band with a width of 46.0 km and a length of 207.3 km and oriented to the northeast of the rig site (Figure 5-6e). Western winds with a reduced speed near May 3 made widespread intact slicks recur (Figure 5-7). A few intermittent slicks beyond the periphery of the oil band approached or even stranded on the Chandeleur Islands. There is a substantial miss by DWOSM hindcast on the west and east sides of oil-infested waters. In comparison with a corresponding oiling footprint, the simulated floating oil trajectory presents a consistent shape yet has a narrower longitudinal dispersion near the spill site and a wider latitudinal extension. On the 13th day after the blowout, a giant slick overlaid 21,430.6 km^2 of offshore waters starting from 44.3 km south of the rig wreck to near the Mississippi-Alabama barrier islands (Figure 5-6d). Less windy conditions do not favor the mitigation of floating oil (Figure 5-7), which facilitates the accumulation of oil continually surfacing from the leak site. Substantial oil traces emerged on the nearshore waters of the MRD and barrier islands.

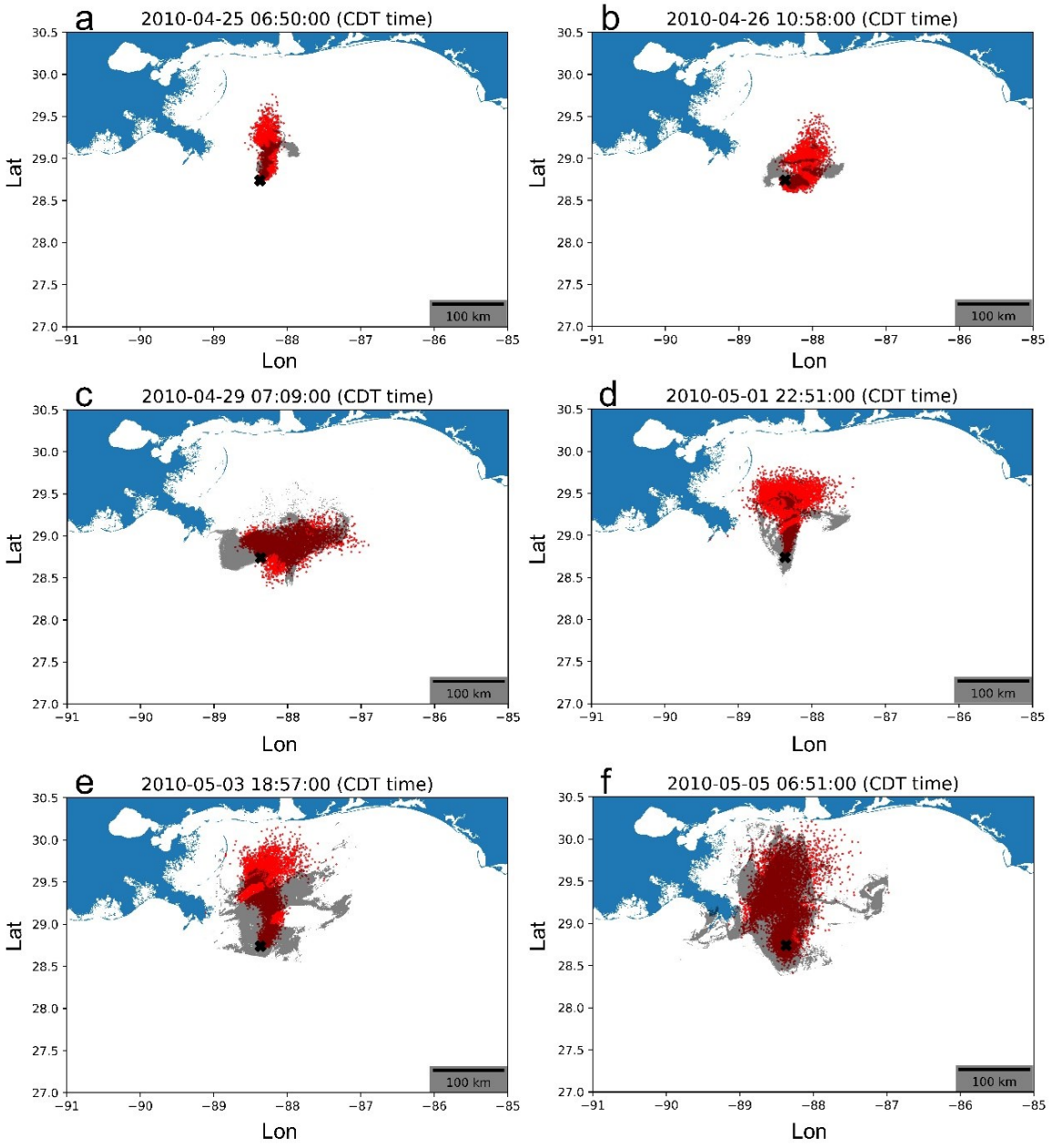

Figure 5-6 The prediction and observation of oil slick trajectory in the DWH spill on a) April 25 06:50, b) April 26 10:58, c) April 29 07:09, d) May 1 22:51, e) May 3 18:57, f) May 5 06:51.

Note: A cluster of red points represents the hindcast of surface oil; the grey shaded area is the TCNNA SAR oiling footprint; the blue patches are the continent of the north GOM; the blank space denotes open waters.

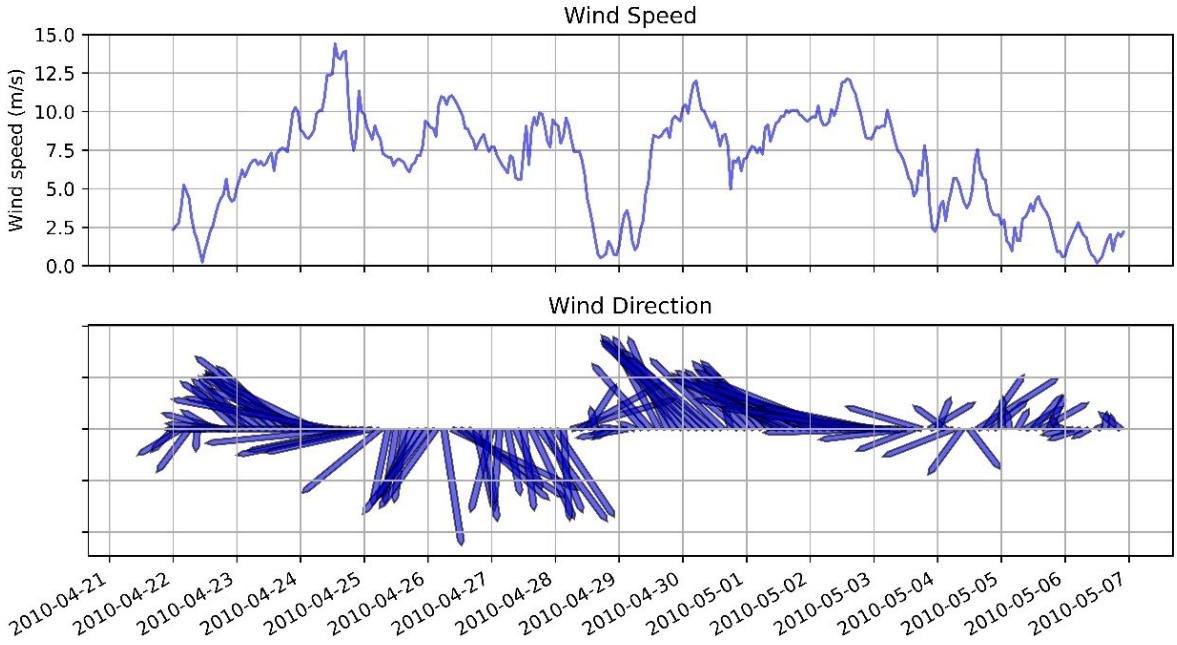

Figure 5-7 Wind record from NOAA stations 42040 from April 22 to May 6, 2010.

Note: It is freely accessible at https://www.ndbc.noaa.gov/station_page.php?station=42040 as of Feb 14, 2024.

In addition to direct comparison, the performance of spill trajectory modeling is quantitatively evaluated by four error measures from different perspectives (Table 5-2). Remote sensing-based observations applied to validate trajectory hindcast is Eulerian data, while the spill movement prediction is based on a Lagrangian framework (Liu *et al.*, 2013). Therefore, the convex hull formed by modeled trajectories is first calculated to facilitate the quantitative comparison. Subsequently, the minimum bounding box is generated to determine the length of each trajectory. As shown in Table 5-2, centroid skill scores ranging from 0.81 to 0.97 imply that the centroid distances of predicted trajectories are always less than the length of the observed slick during the simulation. Centroid distance error on May 1 is more significant than other moments, also directly mirrored by the discrepancy in spatial distribution (Figure 5-6d).

Nonetheless, the distance between the two centroids is further lessened to 16.85 km on May 5, the minimum error among these simulations. Regarding the error of predicted surface oil area, DWOSM simulation results (>0.9 of A_{ss}) are quite close to the observed slick area at 7, 11, and 13 days after the spill. The most apparent errors appear on April 25 (0.49 of A_{ss}) and May 1 (0.41 of A_{ss}) due to overestimating exposure area. Particularly for the modeled trajectory on May 1, neglecting the slick discontinuity resulted in an exaggerated oil area hindcast despite consistent geometry. Furthermore, 2D-MOE indicates the performance of oil trajectory prediction by true positive (x-MOE) and false negative (y-MOE) indexes. All x-MOE indexes are greater than 0.5 apart from the hindcast on May 3, implying that most simulations successfully predict the occurrence of over 50% surface oil at the corresponding moment. Results with higher x-MOE and lower y-MOE mean that the correctly modeled oil-covered area exceeds the region where a hazard was predicted but not observed. Decision-makers usually adopt a minimum regret strategy to identify all floating oil possible, *i.e.*, maximize true positives regardless of the expense of increasing false positives. Hence, this study provides a satisfactory trajectory hindcast from the perspective of the priority of oil spill identification.

Table 5-2 Error metrics for modeled spill trajectory of the DWH blowout.

Time (CDT)	C_{ss}	A_{ss}	Centroid distance error (km)	2D-MOE
2010.04.25 06:50	0.90	0.49	18.36	(0.67, 0.34)
2010.04.26 10:58	0.92	0.71	19.71	(0.51, 0.28)
2010.04.29 07:09	0.96	0.91	22.43	(0.77, 0.72)
2010.05.01 22:51	0.81	0.41	37.36	(0.55, 0.25)
2010.05.03 18:57	0.92	0.99	42.04	(0.47, 0.46)
2010.05.05 06:51	0.97	0.90	16.85	(0.87, 0.82)

This study adopts the heaviest shoreline oiling characteristics observed by field surveys using SCAT to verify the hindcast of stranded oil distribution. The Chandeleur Islands, barring

the MRD, were among the first coastal regions in the northern GOM threatened by exposure to the DHW spill (Kenworthy *et al.*, 2017). As of May 5, the hindcast of stranding locations around the Chandeleur Islands has a good agreement with SCAT-based observations (Figure 5-8). Distances between predicted stranding locations and the maximum oiling spots vary from 2.3 to even 0.1 km, fully capable of providing reliable information for decision-makers to formulate a response plan for tackling nearshore oil pollution. A successive northwestward wind forcing from the end of April to the onset of May probably contributed to oil beaching on the MRD and the Chandeleur Islands (Liu *et al.*, 2013). Hindcast results also provide a few false positives on the Mississippi-Alabama barrier islands but are trivial to decision-making for operational response (Figure 5-7f). It is worth noting that deploying booms prevented substantial floating oil from stranding but is not included in current simulations.

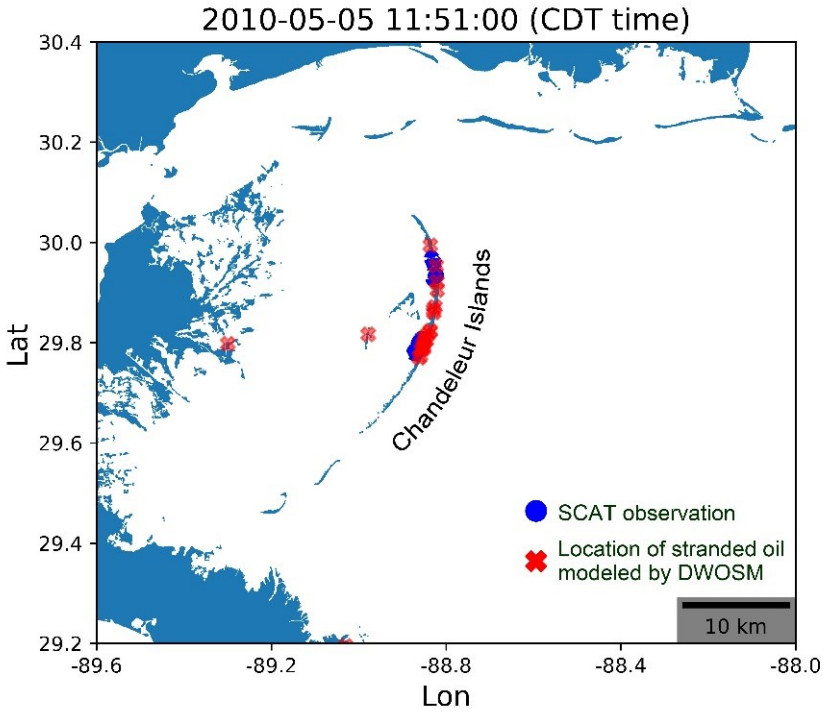

Figure 5-8 The distribution of observed and simulated oil stranding on the Chandeleur Islands as of May 5, 2010.

Note: Blue circles represent the beached oil observed by SCAT shoreline surveys; red crosses denote the modeled location of stranded oil from DWOSM; the blue patches are the continent of the north GOM; the blank space is open waters.

Overall, simulations in DWOSM provide the surface oil distribution analogous to the oiling footprint inferred from satellite imagery and accurately predict the locations of stranded oil during the initial stage of the DWH spill. A comparison between wind data and observed trajectories illustrates that surface oil motion was highly associated with wind speed and direction at most times. Some prediction errors occur to varying degrees because oil spill models naturally inherit the uncertainties from current and wind data supplied to Lagrangian trajectory modeling. A single combination of two background vector fields is used to predict the oil movement, whereas trajectory forecasts stemming from various hydrodynamic and atmospheric reanalysis can be distinct (Liu *et al.*, 2013; French-McCay *et al.*, 2021b). Future studies will investigate the performance of trajectory forecasts driven by varying reanalysis products. On the other hand, the DWOSM model will cease to simulate near-field particles once the buoyant plume is neutralized and cannot track the dispersed-phase oil/gas. Although some measurements of chemistry samples and sensor-based indicators are available to verify the spatial extent of subsea intrusion layers, the current simulation cannot involve deepwater concentrations away from the wellhead and the deep plume beyond the near field.

5.4.5. Oil budget

According to environmental compartments where oil appears and the process of how petroleum fluids are weathered, the released oil is categorized into five groups to uncover the

big picture of an oil budget in the initial stage of the DWH (Figure 5-9). In this study, degraded oil is not counted in the mass balance because the degradation has an insignificant impact on the slick mass in the short term (Galagan *et al.*, 2018). It presumably generalizes the total mass of released oil as the sum of surface and subsurface oil in tandem with evaporated and beached oil. Degraded subsurface oil belongs to the category of submerged oil for this oil budget as it is still retained in the water column. A series of comparisons of the simulated oil budget between DWOSM and SIMAP shows comparable trends in the two models' outcomes (Figures 5-9a and b). For the hindcast results of DWOSM, surfaced oil begins to evaporate rapidly a few hours after the spill (Figure 5-9c). The mass of oil entering the atmosphere almost linearly increases to 6.80×10^4 Mts during the first two weeks, accounting for 57.2% of total released oil as of May 5, 2010. Unlike the fast growth of volatilized hydrocarbons, oil lingering in the water column increases steadily in the first 210 hours and abruptly rises from 1.02×10^4 to 2.70×10^4 Mts in the next two days (Figure 5-9d). Surface oil mass usually grows faster than submerged oil during the first nine days but presents an opposite trend against subsurface mass in the following hindcast, *i.e.*, drops from 1.98×10^4 to 1.26×10^4 Mts (Figure 5-9e). Given that the release condition of this simulation is constant, such a decrease in surface oil is caused by intensified wind-induced breaking waves that facilitate the natural dispersion of surface oil. Ten days after the spill, surface oil resumes increasing at a similar rate as before, implying that the sea state turns stable and unfavorable to surface wave entrainment (Figure 5-9e). An abrupt decline and subsequent rebound in surface oil mass on the tenth day generally fits with NOAA's wind speed record after April 30 (Figure 5-9e). Oil biodegraded in the water column has no fluctuating tendency and climbs to 2.99×10^3 Mts, accounting for only 5.81% of the total mass

(Figure 5-9f). Moreover, the mass of oil stranded on the northern GOM coast is negligible to the oil budget.

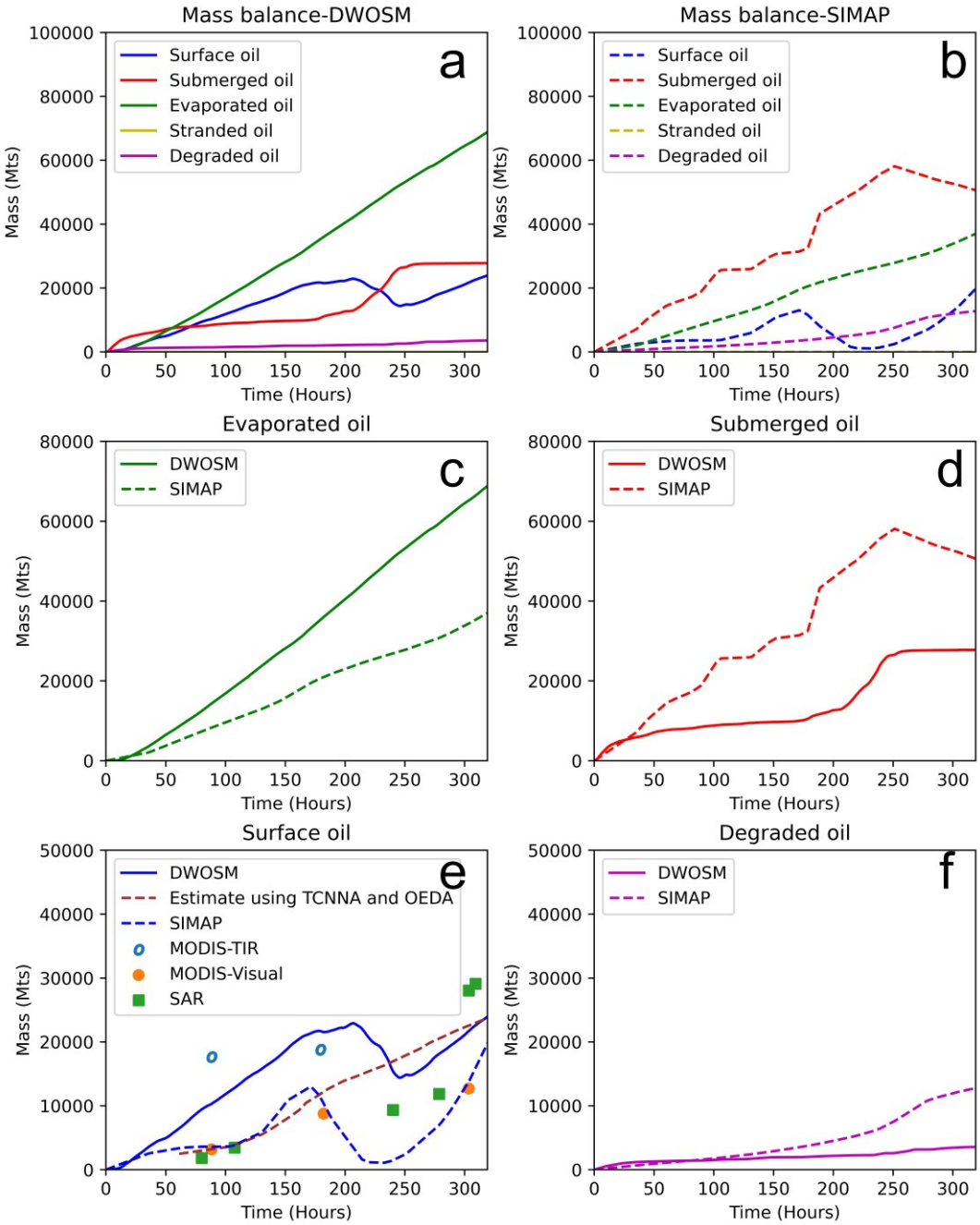

Figure 5-9 The oil budget of the first two-week DWH spill: (a) DWOSM and (b) SIMAP mass balance, (c) evaporated oil, (d) submerged oil, (e) surface oil, and (f) degraded oil.

Note: SIMAP simulations and remote sensing-based estimates originated from French-McCay *et al.* (2021 a and b).

Obviously, more submerged oil and less evaporated oil appear in the oil budget from SIMAP simulation than DWOSM (Figures 5-9 a and b). The evaporated mass has a similar but slower upward trend to the DWOSM result and eventually rises to 3.66×10^4 Mts (Figure 5-9c). As the most significant discrepancy between the two simulations, submerged oil increases rapidly to 3.34×10^4 Mts in the first week, and its uplift even accelerates until 250 hours after the spill (Figure 5-9d). In the following three and a half days, subsurface oil promptly declines from 5.79×10^4 to 5.02×10^4 Mts, eventually taking up 42.5% of the total leaked oil mass as of May 6. Such a reverse is mainly contributed by reduced wave dispersion under low wind conditions after May 3 and augmented biodegradation owing to considerable accumulation of subsurface oil (degraded oil is individually accounted for in the oil budget from SIMAP hindcast). A comparable trend of surface oil with DWOSM results is presented: floating oil steadily increases to 3.93×10^3 Mts during the first 100 hours and rises abruptly to 1.29×10^4 Mts in the next three days, conversely corresponding to the variation in submerged oil mass (Figures 5-9 d and e). From April 29 to May 6, floating oil mass drops to 1.35×10^3 Mts on the noon of May 6 and bounces back to 1.91×10^4 Mts. A trough of surface oil mass from both simulations generally coincides with a wind speed peak observed around May 2 by a moored buoy (Figure 5-7). A slight inconsistency in the timing of turning points from surface oil hindcasts is due to different wind reanalysis data used by the two studies (French-McCay *et al.*, 2021b).

The two oil spill models employ different algorithms to calculate the amount of dispersed surface oil, as discussed in section 4.3.2. This led to remarkably less oil remaining on the sea

surface in SIMAP hindcast as floating oil is almost entrained into the upper water column. However, estimates derived from various remote sensing data demonstrate that surface oil never substantially diminished, even under windy conditions around May 2 (Figures 5-7), to the degree shown in the SIMAP simulation (Figure 5-9e). Notably, data derived from SAR images through processing by TCNNA and Oil Emulsion Detection Algorithm (OEDA) techniques exhibit a monotonic upward trend of surface oil mass. Although the impact of surface dispersant application has not been considered in this study, the hindcast of the oil mass budget provided by DWOSM might be more realistic, given the overestimated surface entrainment rate induced by the double-counting issue. SSDI, barring natural dispersion, may also eliminate the modeled amount of surface oil and yet appear less effective as it could not suppress a surge in floating oil mass even after treatment (Figure 5-9c), as proved by a study of Paris *et al.* (2018).

Building upon a series of coupled algorithms tailored for oil fate forecast and some existing remote sensing data, this study provides and validates the hindcast of oil mass distribution during the initial phase of the DWH spill. A primary challenge to oil fate modeling is a scarcity of information on the oil budget available for validation throughout the spill event, with additional uncertainty led by intensive mitigation activities. Satellite imagery is the sole source of field measurements to verify the modeled oil fate and is only feasible for surface oil. Our hindcast seems to overestimate slick mass in the first week due to the lack of involvement in surface dispersant use for modeling the oil budget. Nonetheless, it is more aligned with estimates than SIMAP simulations afterward. Furthermore, the estimation of floating oil mass requires the observation of slick thickness; however, most of the oil is distributed in the thick

portion of a slick whose thickness ranges over several orders of magnitude (Fingas, 2018). Ambiguity in remotely gauging the thickness regimes of slicks is also manifested by a discrepancy amidst different satellite image-based estimates (Figure 5-9e).

5.5. Summary

In this chapter, DWOSM is applied to perform a hindcast for the transport and fate of oil and gas during the initial period of the DWH spill. A series of vital oil spill simulation results are validated by comparing them with field observations (*e.g.,* remote sensing-based estimates and in-situ measurements) and relevant modeling works. All the comparisons show a good agreement between these simulations and observed data/modeling studies from a practical response point of view: the modeled VMD of treated oil droplets (1.31 mm) has an absolute error of 0.69-1.69 mm; the height of the intrusion layer is exceptionally close to the detection with a relative error of 0.18%; a perfect fit is reflected by none of the methane and ethane appearing in surfaced bubbles from hindcast results and observation; simulated trajectories are consistent with oiling footprints at most moments with a value of C_{ss} and A_{ss} over 0.8 and 2D-MOE exceeding 0.5; the output of surface oil mass generally agree with remote sensing based estimates. Based on comparative analysis among simulated and observed data and wind measurements, it is known that wind speed and direction play an essential role in affecting the spatial distribution of spilled oil and the partition of released hydrocarbons in environmental compartments. In sum, the DWOSM successfully provides a hindcast of the DWH blowout, which exhibits the reliable capacity to forecast the behaviors of large-scale deep-sea blowouts.

Chapter 6 Regional Risk Assessment for Subsea Blowouts in Eastern Canadian Waters

6.1. Overview of the study site

The study area in Chapter 4 is taken as the target region for evaluating regional deep-sea spill risk. As shown in Figure 6-1, a green bounding box covering from 40° N to 55° N latitude and 30° W to 60° W longitude is selected to ensure that the study area includes the main geographical features within East Newfoundland waters, such as the Grand Banks, the Flemish Cap, and marine refuge. Here, hydrodynamic and climate conditions are additionally introduced as follows. The proximity to the continental shelf and the North Atlantic Ocean makes these waters have significant bathymetric variations, with parts to depths over 5,000 meters. The Labrador Current and the Gulf Stream flows are the dominant currents in the Northwest Atlantic, converging at the Grand Banks to create one of the richest fishing grounds worldwide. Most of the Labrador Current is a southeast flowing with roughly consistent magnitude and direction throughout the water column year-round (C-CORE, 2015). The average velocity varies from 0.07 m/s at 1,500 m to 0.2 m/s at 50 m, with a smooth gradient along the water depth. The monthly mean surface current velocity is within the range of 0.22 to 0.32 m/s, double the depth-averaged subsurface velocity. Hence, these statistics indicate that regional hydrodynamic conditions align with the second premise of this methodology. Local wind condition is characterized by strong winds during the winter, with annual mean speeds ranging from 6.15 to 10.44 m/s.

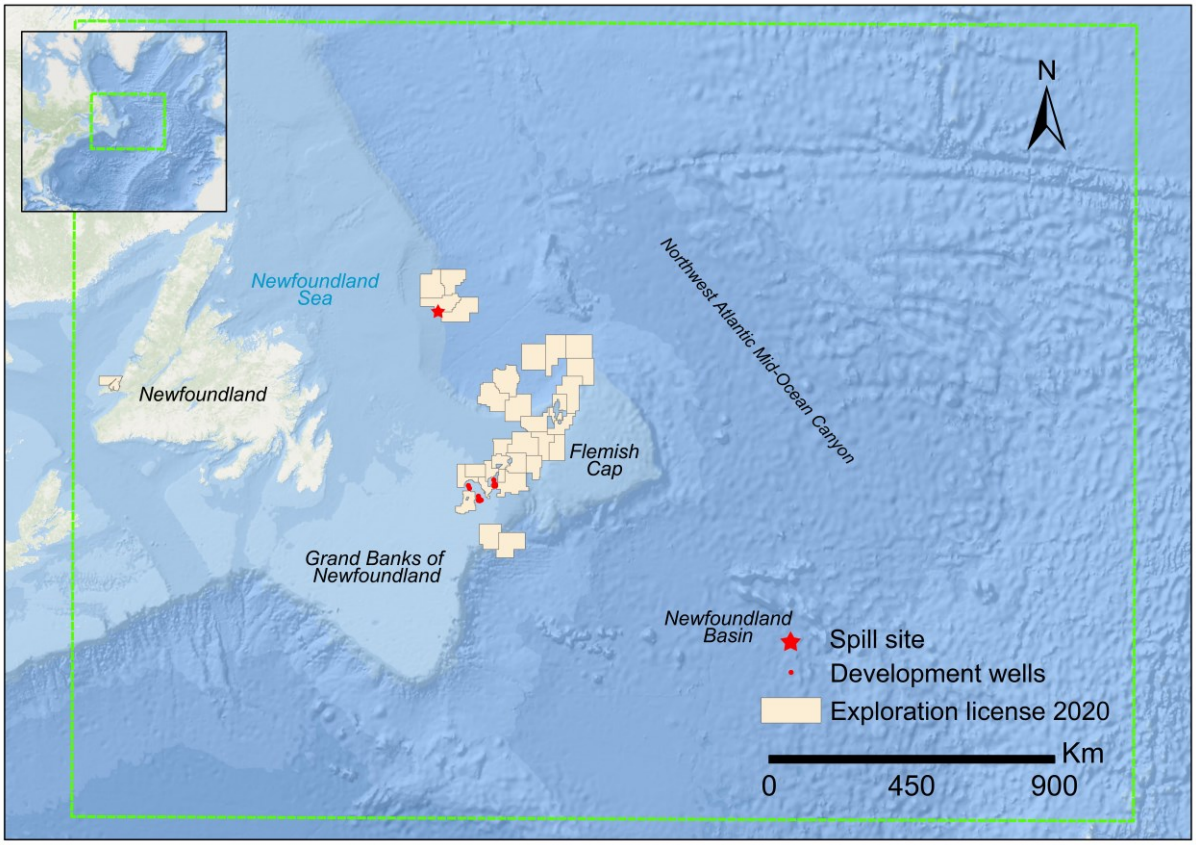

Figure 6-1 Study area of deep-sea spill risk assessment in East Newfoundland waters.

6.2. Model configurations and data collection

A risk assessment framework is thoroughly described in section 3.6 and is implemented in this study case. This study proposes two spill scenarios involving whether or not to apply SSDI (scenarios 1 and 2 in Table 6-1), aimed at investigating the effectiveness of dispersants on subsea spill mitigation. Reducing the input of oil/water IFT can lead to a smaller predicted median droplet size, which implements the modeling of subsurface dispersant application. It is worth noting that the effectiveness of SSDI highly depends on the dispersant-to-oil ratio (DOR). Chemical dispersants typically reduce oil/water IFT by 100 to 200 folds owing to different DORs and oil types (Socolofsky *et al.*, 2015; Brandvik *et al.*, 2021; Socolofsky *et al.*, 2022).

Without considering the effects of DORs on the DSD, this study decreases the oil/water IFT by 100 times for brevity. Considering that DWOSM is tailored for emergency response and ignores weathering processes essential to the long-term oil fate (*e.g.,* biodegradation for surface oil and sedimentation), all the deterministic simulations are conducted within five days, a relatively short duration for large-scale spill accidents like the DWH blowout. The gigantic spill size (>50,000 bbls) is used to evaluate the risk brought by catastrophic blowouts (Holand, 2017). Hibernia crude oil is selected as the spilled substance since its field locations are distributed within the study area. While the computation of the risk index requires PAH concentration, the ADIOS oil database does not clarify the correspondence between pseudo components and specific compounds. According to experimental measurement (ECCC, 2021) and the splitting scheme from similar studies (Stout and Wang, 2017; Galagan *et al.*, 2018), one of the aromatic pseudo components is chosen to approximate PAHs from the crude corresponding to around 1% of oil mass. The rest of the model settings, such as diffusion coefficients for the random walk scheme, use some typical values from previous studies (Galagan *et al.*, 2018).

Table 6-1 Spill scenario configuration and model settings.

Scenario index	SSDI	Flow rate (bbls/day)	Simulation period (days)	Depth (meters)	Release location	Oil type
1 2	No Yes	30000	5	800	50.11 °N, 49.67 °W	Hibernia-type crude (API=37.1)
Simulation step (mins)	Surface horizontal diffusion coefficient (cm^2/s)		Subsurface diffusion coefficient (cm^2/s)		Release diameter (m)	Particle release interval (mins)
			Horizontal	Vertical		
15	10^5		10^3	10	0.2	15

As a critical component of the Copernicus Earth observation programme, the Copernicus

Marine Environment Monitoring Service (CMEMS) publicly provides substantial in-situ and satellite observations and reanalysis products for the global ocean in NetCDF format (Le Traon *et al.*, 2019) (accessible at https://data.marine.copernicus.eu/products as of Feb 14, 2024). This study retrieves hydrodynamic and atmospheric variables required by OSM from CMEMS via a Python toolbox (accessible at https://github.com/copernicusmarine/cmemsapi as of Feb 14, 2024). Specifically, the CMEMS Global Ocean Reanalysis product is selected as the data source of current fields, displayed on a standard regular mesh grid at 1/12° and 50 vertical levels. The daily 3D currents are included from the top layer to the bottom, with the temporal extent from 1 Jan 1992 to 31 Dec 2020. Since no consecutive long-term wind time series compatible with selected current data is available at CMEMS, a reanalysis product consisting of two separate datasets, termed Global Ocean Hourly Reprocessed Sea Surface Wind and Stress from Scatterometer and Model, is used as expedient to agree on the temporal extent of current fields. The bias corrections of the first dataset are based on QuikSCAT SeaWinds scatterometer observations (ranges from 1999-2009 with 1/4° horizontal resolution); the second relies on Metop-A/B/C ASCAT scatterometer observations (ranges from 2007-present with 1/8° horizontal resolution). We spatially average the ASCAT dataset to reduce its resolution and merge it with the QuikSCAT SeaWinds dataset to produce a new wind field with the temporal extent from 1 Jan 1999 to 31 Dec 2020. Coastline data is the subset of a global self-consistent, hierarchical, high-resolution geography database retrieved from the GNOME Online Oceanographic Data Server. For information on spilled oil, the ADIOS OilLibrary adopts SARA (saturate, aromatic, resin, and asphaltene) categorization to estimate the physicochemical properties of specified petroleum types as the input of DWOSM. Pursuant to

the produced water concentration percentage from the Hibernia Platform (HMDCL, 2020), a certain amount of aromatic pseudo components from the original database is substituted with some primary volatile organic compounds (VOCs) that occur naturally in crude oil, including benzene, toluene, and ethylbenzene. Another common VOC contaminant (well-known as one of the BTEX compounds), xylenes, is precluded in the fate simulation due to the various properties of its three isomers (*p*-xylene, *o*-xylene, and *m*-xylene).

6.3. Results

The initial step after selecting the area of interest and environmental datasets is to assemble $M0$ (Figure 3-5). In the study area, the node number of gridded surface current data n_c is 65,702 (182 in latitude and 361 in longitude); wind data has 7,381 grid points n_w (61 in latitude and 121 in longitude). It is noteworthy that the selected atmospheric reanalysis has a temporal resolution incompatible with two other datasets. Therefore, the daily mean speed is computed to reconstruct the hourly wind product. Regarding subsurface currents, the depth-averaged velocity is derived by calculating the mean values of grid cells where the vertical projection of the release point exists. With those velocity components, $M0$ is generated with huge dimensions (8,035×146,168), representing a collection of met-ocean conditions within the study area through 22 years (1 Jan 1999 to 31 Dec 2020). PCA is then performed on $M0$ to obtain principal components that capture more than 95% of the variance. A matrix $M1$ with reduced dimensions (8,035 × 398) is accordingly generated, indicating 398 principal components at each time step. As mentioned, the simulation period D used for stochastic modeling defaults to five days. To reconstruct $M1$ as the input data of the K-means algorithm, a matrix $M2$ with dimensions (8,031×1,990) is produced by flattening 8,031 sub-patterns

having a 5-step duration at each row. As the result of applying K-means clustering to $M2$, we obtain $M3$ (8,031×1,990) and further split its rows to build a 3D matrix $M4$ (8,031×5×398). Though multiplying the eigenvectors yielded from the PCA application, $M4$ is restored to $M5$ having the comparable size ($8{,}031 \times 5 \times 146{,}168$) with $M0'$ for evaluating the agreement between extracted patterns with original datasets. After repeated comparisons, the trend of the refined Willmott's index is presented in Figure 6-2: a sharp rise in d_r from 0.05 to 0.66 as the cluster number increases from 1 to 14; then, d_r steadily reaches the termination criteria when the cluster number equals 55. So far, 55 met-ocean patterns representative of the spatiotemporal evolution of local met-ocean conditions have been successfully acquired, which offers the cornerstone for stochastic OSM. These patterns are used as the input of environmental background data for each spill scenario (Table 6-1), requiring only 108 simulation runs in total. Compared with 8,031 possible 5-day sub-patterns from raw datasets, the computational complexity of stochastic simulation is substantially reduced by order of magnitudes.

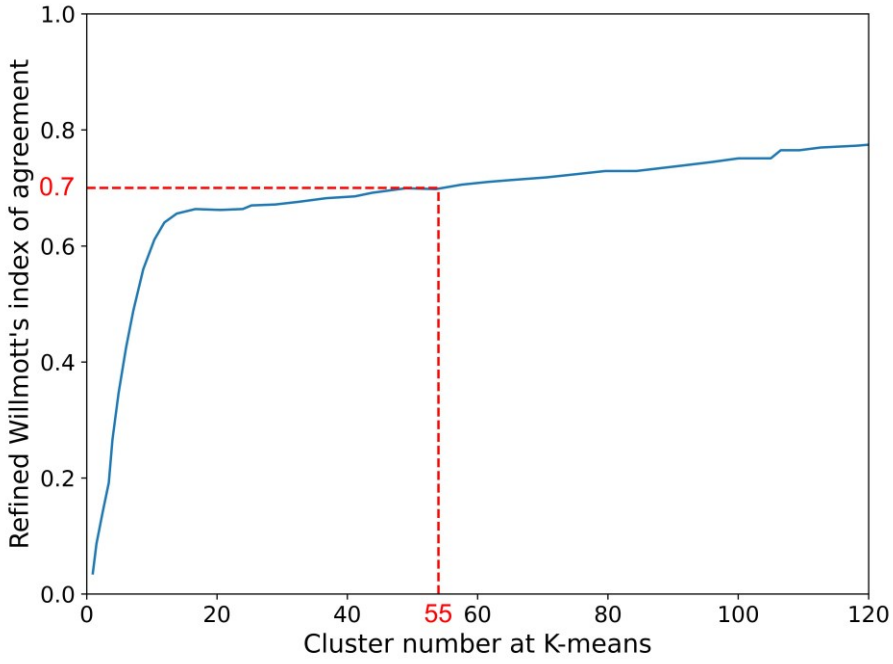

Figure 6-2 The relation between the cluster number used in the K-means clustering algorithm

and a refined Willmott's index.

Oil spill risk index and other attributes are computed at hexahedral meshes covering the maximum extent where LEs appear in all model runs, *i.e.,* 48.61° N to 51.11° N latitude, 47.67° W to 50.67° W longitude, and water depth from 800 meters to surface. The mesh is uniformly segmented by 1/20° horizontal grid cells and 50 vertical levels, generating 150,000 cubical voxels. Through averaging the output of stochastic simulation within each voxel, the scenario-averaged maps of oil contamination resulting from two hypothetical blowouts under various met-ocean conditions are exhibited in Figures 6-3 and 6-4. Figure 6-3a shows 100% oiling occurrence around the projection of the release point to the mid-depth layer (400 meters) and the sea surface, indicating oil exists in those corresponding voxels under every run of scenario 1. Limited horizontal displacement of subsurface oil implies the rapid rise velocity of droplets in the water column, consistent with the first hypothesis adopted in modeling methodology. As the oiling probability map illustrates, most slicks drift toward the southeast and east of oil surfacing locations and distance away from the east coast of Newfoundland; a few spill trajectories appear at other orientations with a likelihood less than 5%, some as far as 136 kilometers off the southwest of the oil-concentrated region where most droplets surfaced. Despite the total spill coverage reaching 23,394 km^2, only 3% of the potential oil-contaminated area repeatedly appears in almost every simulation (Figure 6-3). The mean concentration of PAHs at the mid-depth layer along the rising path of droplets is 421 μg/l (Figure 6-3b), which is likely to cause sublethal or even lethal effects on marine biota (Nagpal, 1993; French-McCay, 2018). Surface PAH concentration in spill-prone areas (>40% oiling probability) varies from 81 to 414 μg/l, substantially greater than the level (an arithmetic mean of 7.14 μg/l) in the other

contaminated zones. On the top layer, the mean area exposed to oil slicks is lower than 1.8×10^4 m^2 within over 90% polluted grid cells (Figure 6-3c); around 62 km² sea surface is covered by water-in-oil emulsions (slick volume including water content) with a thickness exceeding 15 mm, while the remaining spill area is overlaid with emulsified slicks thinner than 1 mm (arithmetic mean 0.08 mm) (Figure 6-3d).

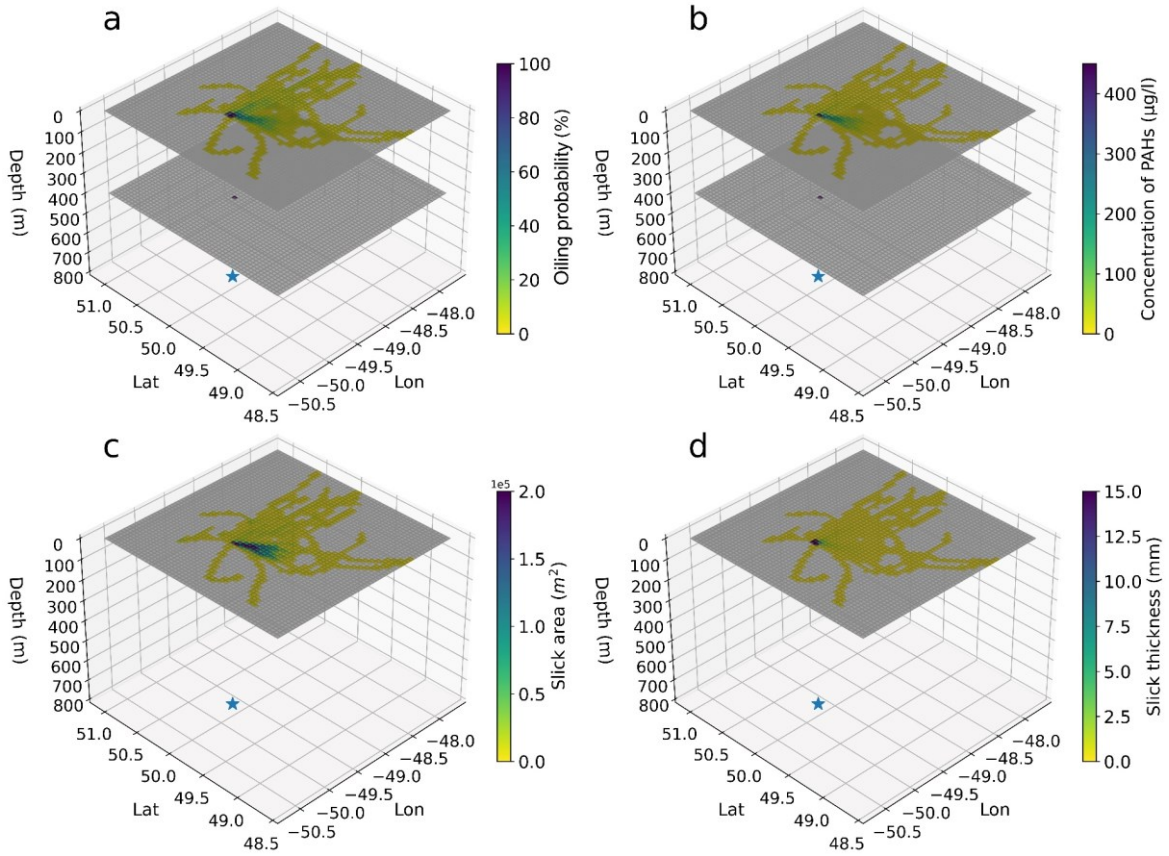

Figure 6-3 Five-day oil spill hazard mapping for scenario 1: (a) oiling probability; (b) PAH concentration; (c) exposure area to surface oil; (d) slick thickness.

Applying SSDI decelerates the rise velocity of droplets from 0.13 to 0.08 m/s (arithmetic mean), allowing the horizontal displacement of subsurface oil at the mid-water depth to magnify near six-fold with 100% oiling probability (Figures 6-3a and 6-4a). Although the maximum spatial extent and drift orientation of surface oil trajectories remain unchanged with

scenario 1, the potential spill coverage expands from 23,394 to 28,323 km^2, with 8% area having over 20% oil occurrence. It also suggests that SSDI makes fluid particles propagate horizontally across a wider region, as submerged oil with reduced size tends to stay in the water column for an extended period and surface at locations farther from the spill site. More PAH contents, ranging from 9 to 417 μg/l with an arithmetic mean of 306 μg/l, appear 400 meters below the surface under scenario 2 (Figure 6-4b). In surface voxels with oil occurrence, PAH concentrations are mainly lower than 5 μg/l and peak at 287 μg/l around spill-prone areas. Compared to the PAH-related risk under scenario 1, the peak level of PAHs at the sea surface is reduced by 31% despite the enlarged scope being potentially affected. The area exposed to slicks sharply drops from 1.6×10^5 to 1.4×10^4 m^2 as spill trajectories move away from oil surfacing locations (Figure 6-4c), which particularly have less exposure level around surfacing points than in scenario 1. Similarly, the thickness of emulsified oil reduces from 14.2 to 0.02 mm when the offset of slicks to surfacing locations increases, with an arithmetic mean of 0.11 mm in 97% of spill areas (Figure 6-4d).

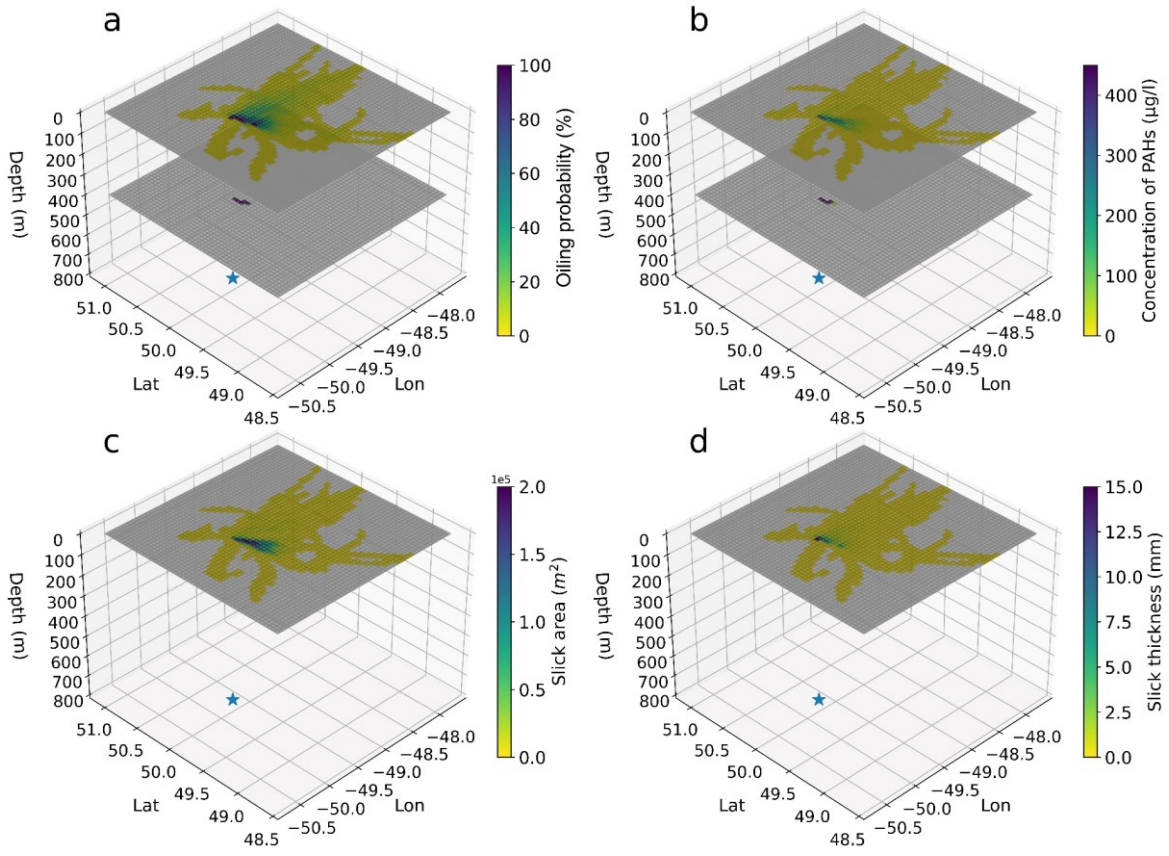

Figure 6-4 Five-day oil spill hazard mapping for scenario 2: (a) probability of oil occurrence; (b) PAHs concentration; (c) exposure area to surface oil; (d) slick thickness.

In contrast to observable SSDI-induced variations on other spill features (Figure 6-4), there is no apparent impact on the spatial distribution of VOCs in floating slicks (Figure 6-5). The surface areas exposed to toluene and ethylbenzene marginally vary from 2,530.42 to 2,376.16 km^2 and 2,808.12 to 2,684.39 km^2, respectively. These extents are roughly an order of magnitude smaller than the coverage of oiling probability five days after the blowout, which only appear on a southeast-oriented circle sector centered on the spill-prone area within a radius of around 39 km (Figures 6-3a, 6-4a, and 6-5). Peak surface concentration after treatment reduces to 2.11 µg/l benzene, 2.76 µg/l toluene, and 4.04 µg/l ethylbenzene, which is mitigated approximately by 30% than the level of scenario 1. Regardless of dispersant application, the

surface concentration of VOCs is lower than 0.40 µg/l on most oiled mesh grids. Ethylbenzene has the highest spatial averaging concentration among the three selected VOCs, with 0.25 µg/l in scenario 1 and 0.23 µg/l in scenario 2. Nonetheless, modeled 5-day VOC exposure levels to the surface water, even for peak concentrations, are far lower than the chronic effects benchmark (>590 µg/l for benzene, >30 µg/l for toluene, and >130 µg/l for ethylbenzene) for many aquatic species (ECCC, 2023).

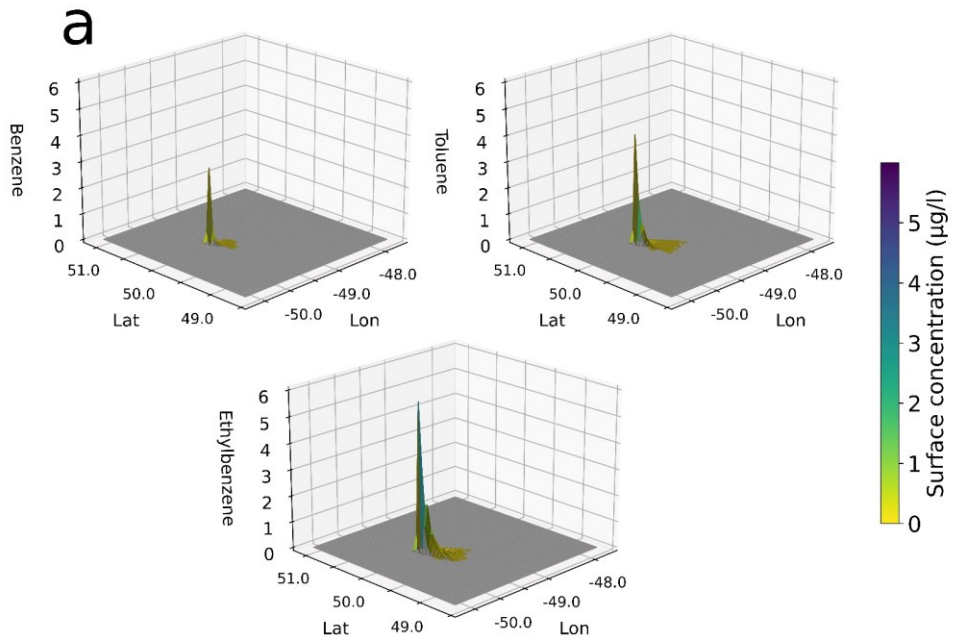

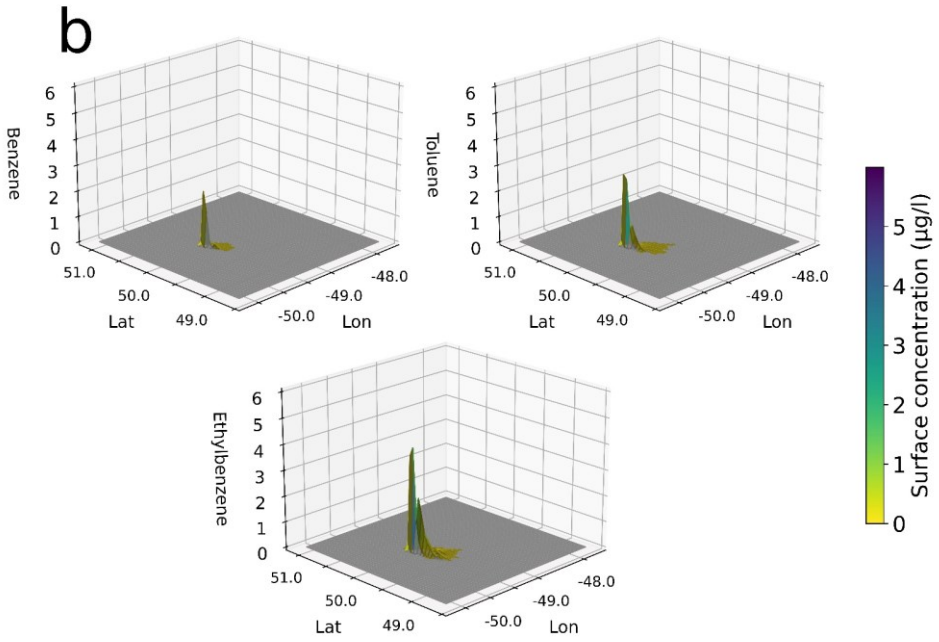

Figure 6-5 Five-day surface VOC concentration mapping under (a) scenario 1; (b) scenario 2.

The integrated risk indicator for the two spill scenarios is visualized with different scales to accentuate the discrepancy in spatial distribution (Figure 6-6). Logarithmic mapping for both scenarios exhibits the quantified risk spanning several orders of magnitude from over 10 to 10^6 (Figures 6-6a and 6-6c). A catastrophic blowout could seemingly impact vast areas of the sea surface (23,113 km^2 in scenario 1 and 28,541 km^2 in scenario 2) within the study domain. Nevertheless, the top voxels with a low-risk level ($<10^3$) account for over 93% of the total oiling area in both stochastic simulations. The risk index at grid cells with less oiling likelihood is negligibly tiny (<10) compared with spill-prone areas ($>10^5$) (Figures 6-6b and 6-6d). The linear-scale risk indicator illustrates that the dispersant treatment substantially diminishes the maximum risk index from 3.4×10^6 to 1.9×10^6. Risk levels (except peak) around where droplets reached the surface were conversely elevated from an average of 9.3×10^4 to 2.3×10^5. The surfacing time of submerged oil is deferred to some degree; hence, droplets tend to drift

downstream farther and have broader dissemination on the sea. In summary, similar to the oiling probability map, the SSDI application amplifies the risky area but mitigates the regional risk of blowouts, mirrored by a reduced arithmetic mean of risk index from 8,536 to 7,891 within the potential oiled zone.

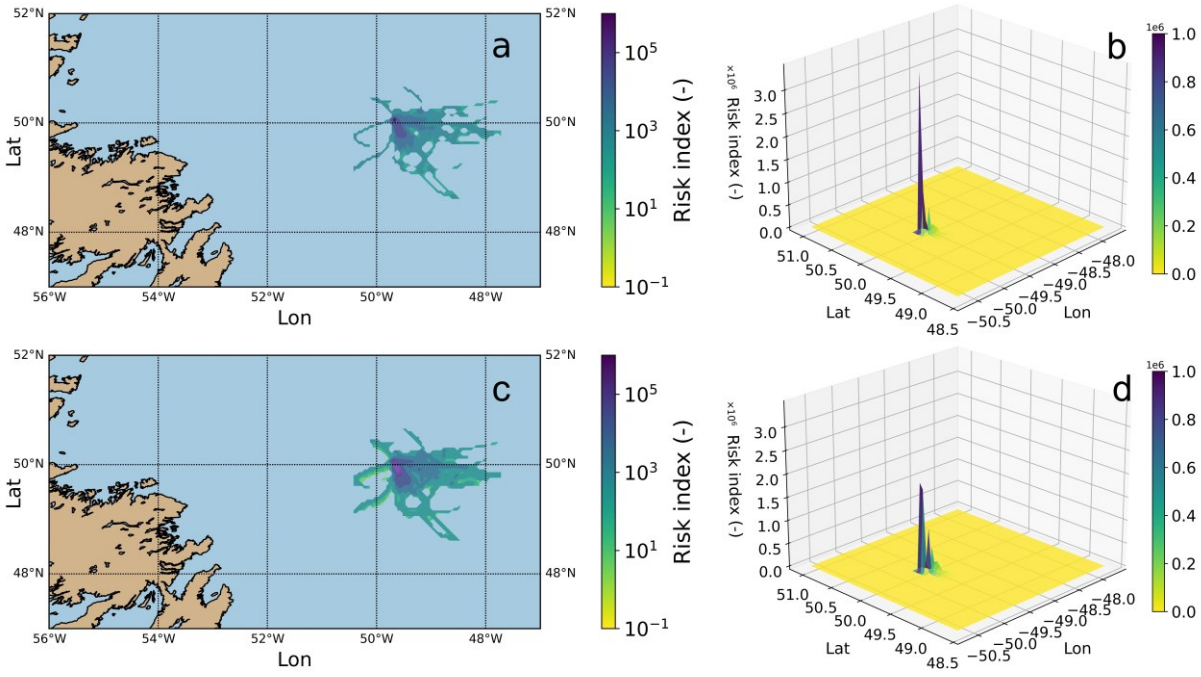

Figure 6-6 Five-day risk mapping of scenario 1 is shown in (a) logarithmic and (b) linear scales; scenario 2 is shown in (c) logarithmic and (d) linear scales.

The effectiveness of SSDI on risk mitigation for subsea blowouts is quantified using histograms (Figure 6-7). Although the potential spill area is amplified to some degree after treatment, unaltered medians of oiling probability reveal that dispersant use barely changes the overall distribution of surface oil occurrence (Figure 6-7a). Most spill areas (>83%) magnified by SSDI have less likelihood of being polluted, aligning with expanded potential trajectories having low oiling probability (<2.7%) (Figures 6-3a and 6-4a). Spill-prone areas slightly increase but have a negligible impact on the statistical distribution of oiling possibility.

Chemical dispersants also alter median emulsion thickness insignificantly from 0.39 to 0.41 mm and a maximum from 15.3 to 17.2 mm (Figure 6-7d). Unlike less effective mitigation on surface oiling probability and thickness, two contributing factors to the risk indicator (*i.e.,* PAH concentration and surface oil loading) are markedly reduced by 26% and 27%, respectively (Figures 6-7b and 6-7e). Median PAH contents at the surface decrease from 11.5 to 8.5 μg/l, dropping the highest concentration from 454 to 332 μg/l. Both scenarios present maximum surface oil loading over 10 g/m^2 and ensemble medians close to 1 g/m^2. It implies that minor slicks may appear dark brown or metallic, and the majority tend to be oil sheen on the sea (Galagan *et al.*, 2018). Reduced sub-indexes correspondingly diminish median spill risk indicators from 8.7×10^4 to 4.7×10^4 and the maximum from 1.8×10^6 to 4.7×10^6 (Figure 6-7f), demonstrating the potential capability of SSDI to eliminate blowout risk on the sea.

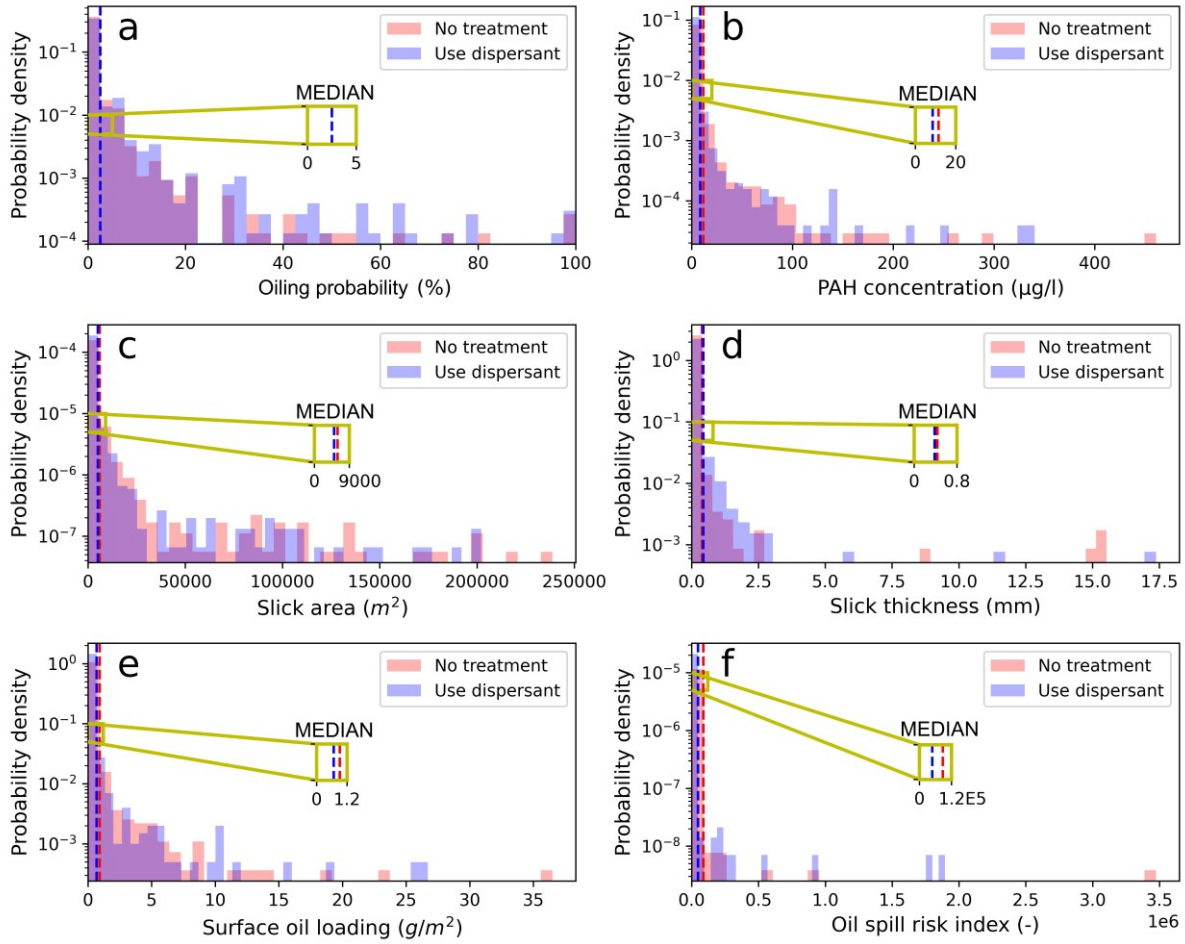

Figure 6-7 The histogram for stochastic OSM results at the sea surface with or without SSDI: (a) surface oiling probability, (b) PAH concentration, (c) slick area, (d) slick thickness, (e) surface oil loading, (f) risk index.

Note: The inset figures that zoom into vertical lines illustrate the median under the two scenarios.

The mass balance diagram depicts the predicted temporal oil distribution in three environmental compartments: water column, atmosphere, and sea surface (Figure 6-8). Without the involvement of SSDI, oil droplets could arrive on the surface only two hours after spills at a mean rise velocity of over 0.1 m/s (Figure 6-8a). Surface oil dominates the mass balance for hypothetical blowouts, and its ensemble mean keeps an almost linear increase to

1.51×10^4 Mts. The extremum of surface oil mass ranges from 1.31×10^4 to 1.76×10^4 Mts at five days. As slicks accumulate on the water, the evaporation of volatile components begins to play a critical role in the natural attenuation of oil spills. The estimated mean mass of oil entering the atmosphere is up to 0.41×10^4 Mts, accounting for 20.6% of total released petroleum. Different wind conditions engender varying evaporation rates for floating slicks, leading to a broad range of volatilized mass from 0.18×10^4 to 0.60×10^4 Mts. Submerged oil mass has a limited variation from 0.18×10^4 to 0.35×10^3 Mts and slowly climbs to 0.67×10^3 Mts at the end of the simulation. This is likely due to increased oil viscosity as the result of rapid evaporation and emulsification, severely hindering the rate of wave entrainment. Likewise, surface oil remains predominant in the spill mass balance after applying SSDI, but its ensemble mean decreased by 0.37×10^4 Mts than in scenario 1 (Figure 6-8b). An observable effect of SSDI on the mass balance prediction is the uplift in submerged oil that increased by around five times than scenario 1, despite only a minor proportion of the total released oil mass. Less evaporative mass loss, an average of 0.34×10^4 Mts, is also presented in scenario 2 as the reduced surface area of slicks. Oil entering the atmosphere varies from 0.13×10^4 to 0.52×10^4 Mts, on average 82.9% of the evaporative loss than scenario 1.

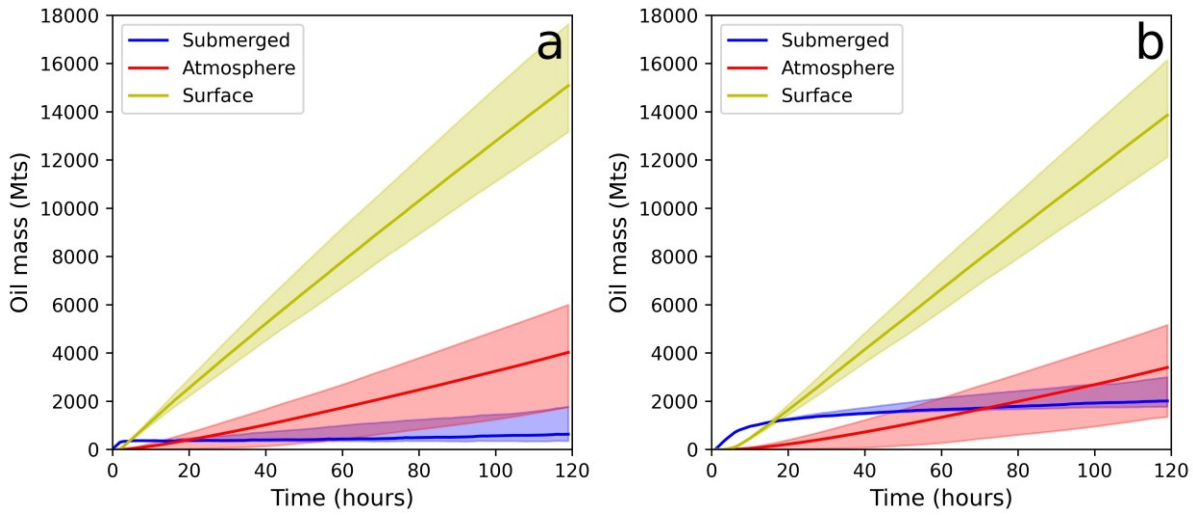

Figure 6-8 The diagram of oil mass balance from stochastic simulation under (a) scenario1 and (b) scenario2.

Note: Shaded areas depict the variation range of oil fate (mean ± maximum/minimum).

6.4. Discussion

Our study begins by extracting representative met-ocean patterns from oceanic and atmospheric reanalysis. The choice of a conservative threshold of Willmott's index allows the newly produced dataset to capture the spatiotemporal evolution of currents and winds in the area of interest. It also provides the rationale for the definition of spill scenarios regarding environmental background fields. Hazard mapping for hypothetical blowouts in the east offshore waters of Newfoundland is implemented by overlapping the results of deterministic simulations under 55 met-ocean conditions. Whether to use SSDI or not, none of the potential oil trajectories reach the seashore within five days after the spill (Figures 6-6a and 6-6c). As mentioned in section 6.1, the southeast-flowing Labrador Current dominates the local hydrodynamic regime, thereby usually migrating slicks along the current flow direction. Combined with great distances (>300 km) between active offshore fields and shorelines,

surface oil has less likelihood of arriving on the coast during a short period. This implies a longer window of opportunity for responders to tackle oil pollution before slicks are stranded. Nevertheless, the water depths of active offshore oil rigs are less than 100 meters in Newfoundland and Labrador. The coverage of spill location from this case study is also limited and thus cannot ensure the coastal area is risk-free from oil accidents closer to the shore. In the event of blowouts at shallow-water fields or coastal zones, released oil will more likely arrive at the shorelines faster than our predictions. In future works, we will investigate the spill risk of currently operating wells (*e.g.,* the White Rose and the Hibernia oil field) and pending offshore projects (*e.g.,* Bay du Nord), which are associated with potential blowouts occurring at different depths and locations (Equinor, 2023).

A good agreement between the distributions of oiling probability and PAH concentrations aligns with the utility of PAHs as an indicator of the general distribution of petroleum hydrocarbons in oil-contaminated sites (Sammarco *et al.*, 2016) (Figures 6-3 and 6-4). The predicted concentrations range from tens to hundreds of micrograms per liter, sufficient to acutely cause lethal impacts on marine biota, especially for fish at earlier life stages (French-McCay *et al.*, 2018). Treated exposure levels of PAHs are still inadequate to eliminate its biological hazards, not to mention the additional risk of adding chemical dispersants. There is a distinct discrepancy in the surface distribution between the concentrations of PAHs and VOCs (Figures 6-3, 6-4, and 6-5). Unlike heavy fractions exhibiting great persistence in crude oil, BTEX compounds are volatile due to their high vapor pressure and can evaporate off from surfaced oil within one day or less (Jordan and Payne, 1980; Avens *et al.*, 2011). Therefore, the traces of three VOCs coincide with oil surfacing locations and disappear entirely as slicks drift

away from the spill source (Figure 6-5).

Considering that the contamination levels of selected VOCs are well below the environmental quality guidelines, we believe that surfaced VOCs have no significant adverse effects on aquatic life in the upper water column for our case. However, those highly volatile chemicals emitting from fresh slicks can rapidly enter the air, exposing responder personnel working near the sea surface to VOCs through dermal contact and inhalation. Many workers participating in the DWH cleanup operations underwent respiratory distress, headaches, skin problems, nausea, and even hematuria (Sammarco *et al.*, 2016). The risk of airborne VOCs to wildlife and human health cannot be ruled out here and thus will be evaluated in follow-up research. Some recent findings suggest that SSDI significantly contributed to mitigating the atmospheric emissions of VOCs during the DWH (Gros *et al.*, 2017; Crowley *et al.*, 2018; Afshar-Mohajer *et al.*, 2019; Zhao *et al.*, 2021). Evidence shows that on-field responders were not required to wear respiratory protection after applying dispersants at the wellhead (Boufadel *et al.*, 2023). We conclude around a 30% reduction in the peak concentrations of selected volatiles, similar to the simulation result of a 28% VOC emission decrease from Gros *et al.* (2017) despite the different VOC definitions and less effective in mitigating benzene from this study.

SSDI, in response to hypothetical blowouts, magnifies pathways of simulated oil to a certain degree, especially for non-spill-prone areas, but is less consequential to the maximum spatial extent of slicks (Figures 6-3a and 6-4a). Considerable chemically dispersed petroleum eventually emerged around where the untreated oil surfaced, spread over a wider area and further from the spill site. In terms of the predicted spill mass balance (Figure 6-8), a vast

amount of treated oil (>70% total release oil mass) still leaves the water column after five days, implying the necessity for other cleanup techniques to tackle the oil pollution, such as mechanical recovery, in-situ burning, and even surface dispersant use. Taken together, these findings indicate that SSDI may be incapable of keeping most rising oil droplets submerged for a period long enough to meet the objective of decision-makers using dispersants. The effectiveness of SSDI, which significantly increases the water column sequestration of the dispersed oil phase, was also not detected during the DWH spill (Boufadel *et al.*, 2023). It was reported that the addition of dispersants could no longer substantially reduce droplet sizes when the initial DSDs are tiny (typically <300 μm) (Paris *et al.*, 2012 and 2018). In this case study, the maximum terminal velocity of untreated oil only scales down from 0.15 m/s to 0.09 m/s, which only causes the 2- to 6-hour lag time to retain submerged droplets. Hence, treated droplets with millimeter-scale diameters still transport most hydrocarbons to the sea surface. A recent study reveals that the deployment of the dispersant Corexit® 9500 failed to maintain the oil submerged as none of the significant effects were detected during the DWH blowout (Paris *et al.*, 2018). The underperformance of changing oil vertical distribution in the first and only real-world application (*i.e.,* the DWH) and adverse toxic effects make unrestricted SSDI applications responding to deep-sea spills highly debatable. The relatively shallow water depth of this hypothetical blowout may also lead to less effectiveness in reducing surface oiling (NASEM, 2020).

On the other hand, numerous numerical experiments, including this work, exhibit the promising potential of SSDI to mitigate the contamination level of certain aspects of deep-sea spills (Spaulding *et al.*, 2017; Crowley *et al.*, 2018; French-McCay *et al.*, 2018). Controversy

about the effectiveness and impacts of dispersant use, particularly on deep-sea blowouts, will continue until more scientific evidence emerges. As a novel and supplemental method to SSDI, subsea mechanical dispersion (SSMD) enhances turbulent dissipation near the release nozzle to reduce the oil droplet sizes from blowouts and performed well in extensive studies (Brandvik *et al.*, 2020). Further studies will examine its effectiveness in mitigating the risk of deep-sea blowouts.

Although datasets selected for pattern extraction cover sufficient temporospatial extent, some ocean variables vital to oil transport and fate (*e.g.,* water temperature and sea ice) are currently not included in this work. Global warming has caused an increasing annual number of ice-free days within offshore Newfoundland and Labrador (C-CORE, 2015). Even when the pack ice emerges during the limited freeze-up dates, it only exists in lower concentrations along the coast, which has minimal influence on the deepwater basins of interest (*e.g.,* the Grand Banks and the Flemish Pass). Thus, we surmise whether incorporating sea ice in met-ocean patterns is insignificant to spill risk assessment results. However, icing and pack ice conditions must be considered once blowouts occur in nearshore areas because slicks are very likely to encounter sea ice in winter. The threat of icebergs to offshore operations should also be involved in future spill risk assessments, as ocean currents sometimes carry icebergs along the east coast of Newfoundland (Kaiser, 2021). Regarding water temperature, particularly sea surface temperature, its variation can substantially affect the rate of weathering processes like evaporation and even make oil lose fluidity when the temperature is below the pour point. We will attempt to include temperature for refining met-ocean patterns in the follow-up study. Moreover, the oceanic reanalysis database used in this study originates from a global ocean

general circulation model designed to describe global-scale hydrodynamic and thermodynamic processes in oceans. More complex processes occurring at finer resolutions, such as coastal hydrodynamics, are difficult to capture by this model type.

Another major limitation of the current risk assessment is the lack of information on biological resources, especially for the distribution of oil-sensitive species. The study area encompasses a maritime region of over 370,000 km^2 offshore waters of Eastern Newfoundland, which contains a variety of marine biota and their habitats (*e.g.,* fish, coral reefs, benthos, marine mammals, and sea turtles). As the foundation of marine food webs and a crucial role in nutrient and carbon cycling between the atmosphere and ocean, the plankton community thrives in upwelling areas along the continental shelf and within the Flemish Cap (GC, 2020). The predicted exposure of PAHs reaching hundreds of micrograms per liter has a lethal impact on environmentally sensitive regions mentioned above in a brief time frame; VOCs pose fewer toxic threats through the pathways aside from inhalation because of their low concentration at the sea surface. Furthermore, a constant spill location in scenario definition and no involvement of biological information may be inadequate to obtain credible risk distributions of petroleum pollutants. In addition to including species distribution and the toxicity thresholds of PAHs to valued components, we will combine the actual oil reservoir conditions within the study area to replenish spill scenario settings regarding the spill size, location, and oil type. The environmental sensitivity index for shoreline areas will also be incorporated into the methodological framework.

6.5. Summary

This study modifies the framework of an integrated stochastic OSM by employing a new

indicator, and then applies it to evaluate the short-term PAH-related risk from potential blowouts in the offshore area of east Newfoundland. Over fifty representative met-ocean patterns are extracted from 22-year oceanic and atmospheric reanalysis products using data mining techniques. By doing so, the number of model runs pertaining to environmental background becomes well-defined, dramatically reducing the computational cost required by stochastic simulation. A newly developed DWOSM designed for deep-sea blowouts is employed for each deterministic simulation. Two hypothetical blowout scenarios around an oil field with active exploration licenses are proposed to quantitatively compare the regional spill risk level with or without SSDI application. Ultimately, we obtain a series of five-day hazard maps that characterize the spatial distribution of spill features and risk within the area of interest.

The results reveal that released oil from a catastrophic blowout can rapidly reach the sea surface within a few hours and most likely drift towards the east and southeast after surfacing. Owing to the presence of the southeast-flowing Labrador Current, the nearshore area of Newfoundland has a low risk of oil spillage shortly after the spill. An oil-infested area tends to form around the surfacing location for most oil droplets, necessitating sufficient preventive practices to counter the large volume of emerging oil. Downstream areas are open seas with dynamic conditions for diluting spilled oil. Nevertheless, the risk of valued species exposed to hazardous petroleum compounds, particularly for PAHs, cannot be ruled out, and the information on distributions of targeted marine biota must be considered in the follow-up studies. After the treatment of SSDI, an increasing portion of subsurface oil remains submerged while the spatial distribution of surface and subsurface oil is amplified. Contrary to mitigating the risk level in the spill-prone region, the risk beyond there is somewhat elevated. The

effectiveness of SSDI in spill risk reduction is still questionable and needs further investigation. Future work will focus on refining spill scenario settings and completing the met-ocean pattern.

Chapter 7 Conclusions and Future Perspective

7.1. Conclusions

This dissertation is dedicated to developing a novel operational OSM toolkit, DWOSM, for predicting the transport and fate of oil/gas released from deep-sea blowouts. Through integrating three individual modules, DWOSM is capable of forecasting a series of blowout behaviors in support of the oil spill response. Specifically, DWOSM-DSD intends to predict the diameter size of oil droplets/gas bubbles and their corresponding volume fraction; DWOSM-Nearfield aims to simulate the evolution of buoyant plume dynamics; DWOSM-Farfield is to forecast the spill trajectory and the change in oil mass and properties beyond the near field. Terminal near-field simulation results provide initial conditions to DWOSM-Fairfield, which achieves the coupling of near- and far-field modeling. Different case studies are presented in this dissertation, including a hypothetical case in Eastern Canadian waters and a real-world case of the DWH blowout in the GOM, which is used to test the applicability and validity of the DWOSD. Apart from the model development and verification, the DWOSM and a risk evaluation system are also embedded into a recent integrated stochastic modeling methodology. The PAH-related risk in the offshore waters of east Newfoundland is successfully evaluated through stochastic simulation of deep-sea blowouts. The main conclusions of the three research tasks are summarized as follows:

1. A hypothetical blowout at 800 meters in eastern Newfoundland waters is used for model testing by comparing the integration of three OOSMs. DSD simulations are verified with

experimental observations and outcomes from a PDM, indicating that the prediction for oil DSDs primarily agrees with experimental and modeling results. The spill trajectory comparison shows considerable similarity in surface slicks under constant environmental fields, while the two models have the same drift direction but a less extended subsurface oil trajectory of DWOSM-Farfield than SIMAP. A discrepancy in the results of the modeled oil budget is due to different selections of entrainment algorithms. Spill trajectory results from DWOSM and GNOME are consistent under actual fields, proving the good applicability of DWOSM for spill trajectory forecast. These results indicate that the new model is comprehensive for numerically characterizing different deepwater spill processes.

2. The DWH blowout is taken for real-field validation by comparing the hindcast result with observational data and previous modeling outcomes. Simulated intrusion height, chemical composition of surfaced gas, and oil stranding locations are highly close to measurements, implying that DWOSM can capture the intricate deep-sea spill behaviors. The hindcast of surface oil trajectory is aligned with the oiling footprint at most moments. For oil budget calculation, the surface oil mass may be overestimated first but then agree with the remote sensing-based estimate. This case study demonstrates the ability to forecast large-scale deep-sea spills in response to blowout events.
3. A modified stochastic modeling framework is applied to evaluate the deepwater spill risk in an offshore area of Newfoundland. Five-day risk mapping results reveal the coastal area of Newfoundland has a low-risk level of oil contamination within the short term after the blowout. A comparison between the two modeling scenarios exhibits the potential of applying SSDI to mitigate the spill risk but amplify the oil dissemination. The predicted

distribution of hazardous petroleum compounds shows that, unlike rapidly evaporated VOCs, PAHs emitting from a catastrophic spill can severely threaten aqueous species.

7.2. Contributions

The main contributions of this study to develop and verify the novel DWOSM, which can be summarized below:

1. Unlike most deepwater oil spill toolkits, which couple near- and far-field models using the results at the end of the near field as the input for far-field modeling, DWOSM adopts near-field particle tracking to smooth the transition between the two models. The coupling of near- and far-field modeling is well-tested in the context of hypothetical and field cases. It demonstrates that such an integration approach can effectively capture deep-sea spill processes occurring at distinct spatiotemporal scales.
2. The sophisticated thermodynamic modeling based on the PR-EOS is integrated into the DWOSM, enabling this model to predict the evolution of the thermodynamic and physicochemical properties of dispersed oil and gas under varying ambient conditions in the deep sea. Particularly, the mass transfer and rise velocity of particles can be computed using constantly updated information. Such an advance has not been involved in most current OOSMs.
3. The DWOSM and a PAH-related risk evaluation system are incorporated into a state-of-the-art stochastic modeling methodology, which allows quantitative characterization of the risk level of spill exposure to marine life. This stochastic simulation-based risk assessment result provides scientific evidence for decision-making support in response to subsea blowouts in Eastern Canadian waters with pending offshore activities.

7.3. Recommendations for future studies

This section lists some limitations of DWOSM and modeling efforts and then proposes corresponding recommendations for future work as follows:

1. Some critical weathering processes for the long-term oil fate, such as sedimentation and surface oil biodegradation, are presently not considered in DWOSM. More oil spill behaviors will be incorporated into the fate algorithms.
2. SSDI is the only oil spill response technology available to be simulated in the DWOSM system, whereas several countermeasures are widely used to mitigate the negative impact of oil spills in practice, such as skimmer, booming, surface dispersant application, and in-situ burning. Future studies will endeavor to integrate cutting-edge algorithms for modeling the cleanup processes.
3. The thresholds tailored for the risk evaluation indicator of this study, particularly for PAH concentration, are not species-specific and cannot provide helpful information about the threat to specific aquatic life. Data relevant to local biological resources, such as the LC_{50} and temporospatial distribution of valued ecosystem components, will be collected and incorporated in the future spill risk assessment.

References

Afenyo, M., Veitch, B., & Khan, F. (2016). A state-of-the-art review of fate and transport of oil spills in open and ice-covered water. *Ocean Engineering*, 119, 233-248.

Afshar-Mohajer, N., Fox, M. A., & Koehler, K. (2019). The human health risk estimation of inhaled oil spill emissions with and without adding dispersant. *Science of the Total Environment*, 654, 924-932.

Ainsworth, C. H., Chassignet, E. P., French-McCay, D., Beegle-Krause, C. J., Berenshtein, I., Englehardt, J., ... & Zheng, Y. (2021). Ten years of modeling the Deepwater Horizon oil spill. *Environmental Modelling & Software*, 142, 105070.

Al Shami, A., Harik, G., Alameddine, I., Bruschi, D., Garcia, D. A., & El-Fadel, M. (2017). Risk assessment of oil spills along the Mediterranean coast: A sensitivity analysis of the choice of hazard quantification. *Science of the Total Environment*, 574, 234-245.

Amir-Heidari, P., & Raie, M. (2019). A new stochastic oil spill risk assessment model for Persian Gulf: Development, application and evaluation. *Marine Pollution Bulletin*, 145, 357-369.

Amir-Heidari, P., Arneborg, L., Lindgren, J. F., Lindhe, A., Rosén, L., Raie, M., ... & Hassellöv, I. M. (2019). A state-of-the-art model for spatial and stochastic oil spill risk assessment: A case study of oil spill from a shipwreck. *Environment International*, 126, 309-320.

Avens, H. J., Unice, K. M., Sahmel, J., Gross, S. A., Keenan, J. J., & Paustenbach, D. J. (2011). Analysis and modeling of airborne BTEX concentrations from the Deepwater Horizon oil spill. *Environmental Science & Technology*, 45(17), 7372-7379.

Bandara, U. C., & Yapa, P. D. (2011). Bubble sizes, breakup, and coalescence in deepwater

gas/oil plumes. *Journal of Hydraulic Engineering*, 137(7), 729-738.

BBC. (2020, August 11). Mauritius oil spill: Locals scramble to contain environmental damage. Retrieved from https://www.bbc.com/news/world-africa-53754751

Bennett, N. D., Croke, B. F., Guariso, G., Guillaume, J. H., Hamilton, S. H., Jakeman, A. J., ... & Andreassian, V. (2013). Characterising performance of environmental models. *Environmental Modelling & Software*, 40, 1-20.

Berry, A., Dabrowski, T., & Lyons, K. (2012). The oil spill model OILTRANS and its application to the Celtic Sea. *Marine Pollution Bulletin*, 64(11), 2489-2501.

Beyer, J., Trannum, H. C., Bakke, T., Hodson, P. V., & Collier, T. K. (2016). Environmental effects of the Deepwater Horizon oil spill: a review. *Marine Pollution Bulletin*, 110(1), 28-51.

Board, M., Board, O. S., & National Research Council. (2003). Oil in the sea III: inputs, fates, and effects. National academies Press. Retrieved from https://doi.org/10.17226/10388

Boufadel, M. C., Özgökmen, T., Socolofsky, S. A., Kourafalou, V. H., Liu, R., & Lee, K. (2023). Oil transport following the Deepwater Horizon blowout. *Annual Review Of Marine Science*, 15, 67-93.

Boufadel, M. C., Socolofsky, S., Katz, J., Yang, D., Daskiran, C., & Dewar, W. (2020a). A review on multiphase underwater jets and plumes: Droplets, hydrodynamics, and chemistry. *Reviews of Geophysics*, 58(3), e2020RG000703.

Boufadel, M., Bracco, A., Chassignet, E. P., Chen, S. S., D'asaro, E., Dewar, W. K., ... & Shepherd, J. G. (2021). Physical Transport Processes that Affect the Distribution of Oil in the Gulf of Mexico. *Oceanography*, 34(1), 58-75.

Boufadel, M., Liu, R., Zhao, L., Lu, Y., Özgökmen, T., Nedwed, T., & Lee, K. (2020b). Transport of oil droplets in the upper ocean: impact of the eddy diffusivity. *Journal of Geophysical Research: Oceans*, 125(2), e2019JC015727.

Boxall, J. A., Koh, C. A., Sloan, E. D., Sum, A. K., & Wu, D. T. (2012). Droplet size scaling of water-in-oil emulsions under turbulent flow. *Langmuir*, 28(1), 104-110.

Brandvik, P. J., Davies, E., Leirvik, F., Johansen, Ø., & Belore, R. (2021). Large-scale basin testing to simulate realistic oil droplet distributions from subsea release of oil and the effect of subsea dispersant injection. *Marine Pollution Bulletin*, 163, 111934.

Brandvik, P. J., Johansen, Ø., Leirvik, F., Farooq, U., & Daling, P. S. (2013). Droplet breakup in subsurface oil releases–Part 1: Experimental study of droplet breakup and effectiveness of dispersant injection. *Marine Pollution Bulletin*, 73(1), 319-326.

Brandvik, P. J., Krause, D. F., Leirvik, F., Daling, P. S., Owens, Z., Gilman, L., ... & Koranek, M. (2021, May). Subsea Mechanical Dispersion (SSMD) a Possible New Option for the Oil Spill Response Toolbox?. In *International Oil Spill Conference* (Vol. 2021, No. 1, p. 689545).

Brandvik, P.J., Johansen, Ø., & Farooq, U. (2014a). Subsea release of oil & gas–a downscaled laboratory study focused on initial droplet formation and the effect of dispersant injection. In *International Oil Spill Conference Proceedings* (Vol. 2014, No. 1, pp. 283-298). American Petroleum Institute.

Brandvik, P.J., Johansen, Ø., Farooq, U., Glen, A., & Leirvik, F. (2014b). Subsurface oil releases – Experimental study of droplet distributions and different dispersant injection techniques Version 2 (Technical report No. SINTEF A26122). Trondheim: SINTEF.

Buchanan, I., & Hurford, N. (1988). Methods for predicting the physical changes in oil spilt at sea. *Oil and Chemical Pollution*, 4(4), 311-328.

Callaghan, D. P., Nielsen, P., Short, A., & Ranasinghe, R. W. M. R. J. B. (2008). Statistical simulation of wave climate and extreme beach erosion. *Coastal Engineering*, 55(5), 375-390.

Camilli, R., Reddy, C. M., Yoerger, D. R., Van Mooy, B. A., Jakuba, M. V., Kinsey, J. C., ... & Maloney, J. V. (2010). Tracking hydrocarbon plume transport and biodegradation at Deepwater Horizon. *Science*, 330(6001), 201-204.

CBC. (2022, April 6). Federal government approves Controversial Bay du Nord Oil Project. Retrieved from https://www.cbc.ca/news/canada/newfoundland-labrador/bay-du-nord-approval-1.6410509

C-CORE. (2015). Metocean Climate Study Offshore Newfoundland & Labrador. STUDY MAIN REPORT, 1. Volume 2: Regional Trends and Comparisons with Other Regions. Retrieved from https://oilconl.com/wp-content/uploads/2018/01/NALCOR-MetOcean-Vol.-2-Final-2017.pdf

Chapman, P., Socolofsky, S., & Hetland, R. (2014, May). From blowout to beach: An integrated modeling approach. In *International Oil Spill Conference Proceedings* (Vol. 2014, No. 1, pp. 919-932). American Petroleum Institute.

Chiri, H., Abascal, A. J., & Castanedo, S. (2020). Deep oil spill hazard assessment based on spatio-temporal met-ocean patterns. *Marine Pollution Bulletin*, 154, 111123.

Clift, R., Grace, J.R., and Weber, M.E. (2005). Bubbles, Drops, and Particles. Mineola, NY: Dover Civil and Mechanical Engineering, Dover Publications. c1978.

Cohen, Y., Mackay, D., & Shiu, W. Y. (1980). Mass transfer rates between oil slicks and water. *The Canadian Journal of Chemical Engineering*, 58(5), 569-575.

Cooper, C., Adams, E., & Gros, J. (2021). An evaluation of models that estimate droplet size from subsurface oil releases. *Marine Pollution Bulletin*, 163, 111932.

Crowley, D., French-McCay, D., Santos, L., Chowdhury, B., & Markussen, R. (2018). Modeling atmospheric volatile organic compound concentrations resulting from a deepwater oil well blowout–Mitigation by subsea dispersant injection. *Marine Pollution Bulletin*, 136, 152-163.

CTV news. (2022, May 11). N.L. oil regulator releases call for offshore exploration bids after federal delay. Atlantic. Retrieved from https://atlantic.ctvnews.ca/n-l-oil-regulator-releases-call-for-offshore-exploration-bids-after-federal-delay-1.5898690

Danesh, A. (1998). PVT and phase behaviour of petroleum reservoir fluids. Elsevier.

Daskiran, C., Xue, X., Cui, F., Katz, J., & Boufadel, M. C. (2021). Large eddy simulation and experiment of shear breakup in liquid-liquid jet: formation of ligaments and droplets. *International Journal of Heat and Fluid Flow*, 89, 108810.

Davis, C. S., & Loomis, N. C. (2014). Deepwater Horizon Oil Spill (DWHOS) Water Column Technical Working Group Image Data Processing Plan: Holocam, Description of Data Processing Methods Used to Determine Oil Droplet Size Distributions from in Situ Holographic Imaging during June 2010 on Cruise M/V Jack Fitz 3. Woods Hole, MA: Woods Hole Oceanographic Institution and MIT.

Dearden, C., Culmer, T., & Brooke, R. (2021). Performance measures for validation of oil spill dispersion models based on satellite and coastal data. *IEEE Journal of Oceanic*

Engineering, 47(1), 126-140.

Degnarain, N. (2020, August 21). UN Satellites Reveal 30 Kilometers of Mauritius Shoreline Heavily Affected by Wakashio Oil Spill. Forbes. Retrieved from https://www.forbes.com/sites/nishandegnarain/2020/08/21/un-satellites-reveal-30-kilometers-of-mauritius-shoreline-heavily-affected-by-wakashio-oil-spill/?sh=2ff991852a1d

Delvigne, G. A. L., & Sweeney, C. (1988). Natural dispersion of oil. *Oil and Chemical Pollution*, 4(4), 281-310.

Dissanayake, A. L., Gros, J., & Socolofsky, S. A. (2018). Integral models for bubble, droplet, and multiphase plume dynamics in stratification and crossflow. *Environmental Fluid Mechanics*, 18, 1167-1202.

Driskell, W. B., & Payne, J. R. (2018). Macondo oil in northern Gulf of Mexico waters–part 2: dispersant-accelerated PAH dissolution in the Deepwater Horizon plume. *Marine Pollution Bulletin*, 129(1), 412-419.

Drozdowski, A., Nudds, S., Hannah, C. G., Niu, H., Peterson, I., Perrie, W., & Department of Fisheries and Oceans, Dartmouth, NS(Canada). Ocean Sciences Div. (2011). Review of oil spill trajectory modelling in the presence of ice (No. 274). DFO, Dartmouth, NS (Canada). Retrieved from https://publications.gc.ca/collections/collection_2012/mpo-dfo/Fs97-18-274-eng.pdf

ECCC. (2023). Canadian Environmental Protection Act, 1999. Federal Environmental Quality Guidelines: Benzene, Toluene, Ethylbenzene, Xylene (BTEX). Ottawa (ON): Government of Canada. Retrieved from

https://www.canada.ca/content/dam/eccc/documents/pdf/pded/feqg-btex/cepa-draft-feqg-benzene-toluene-ethylbenzene-xylene.pdf

Environment and Climate Change Canada (ECCC). (2021). Environment Canada crude oil and petroleum product database. Open Government Portal. (n.d.). Retrieved from https://open.canada.ca/data/en/dataset/53c38f91-35c8-49a6-a437-b311703db8c5

Equinor. (2023). The Bay du Nord Project. Equinor. Retrieved from https://www.equinor.com/where-we-are/canada-bay-du-nord

Etkin, D. S., Michel, J., McCay, D. F., Boufadel, M., & Li, H. (2008, May). Integrating state-of-the-art shoreline interaction knowledge into spill modeling. In *International Oil Spill Conference* (Vol. 2008, No. 1, pp. 915-922). American Petroleum Institute.

Fingas, M. (2017). Introduction to Oil Spill Modeling. Oil Spill Science and Technology (second ed.), Gulf Publishing Company, pp. 419-454

Fingas, M. (2018). The challenges of remotely measuring oil slick thickness. *Remote Sensing*, 10(2), 319.

Fingas, M., & Fieldhouse, B. (2004). Formation of water-in-oil emulsions and application to oil spill modelling. *Journal of Hazardous Materials*, 107(1-2), 37-50.

French-McCay, D. (2016). Potential effects thresholds for oil spill risk assessments. In *Proceedings of the 39th AMOP technical seminar on environmental contamination and response* (pp. 285-303). Emergencies Science Division, Environment Canada Ottawa, ON, Canada.

French-McCay, D. P., Jayko, K., Li, Z., Spaulding, M. L., Crowley, D., Mendelsohn, D., ... & Rowe, J. J. (2021a). Oil fate and mass balance for the Deepwater Horizon oil spill.

Marine Pollution Bulletin, 171, 112681.

French-McCay, D. P., Spaulding, M. L., Crowley, D., Mendelsohn, D., Fontenault, J., & Horn, M. (2021b). Validation of oil trajectory and fate modeling of the Deepwater Horizon oil spill. *Frontiers in Marine Science*, 8, 618463.

French-McCay, D., Balouskus, R., Ducharme, J., Gearon, M. S., Kim, Y., Zamorski, S., ... & Wilson, R. (2017). Potential oil trajectories and surface oil exposure from hypothetical discharges in the Chukchi and Beaufort seas. In *Proceedings of the 40th AMOP Technical Seminar on Environmental Contamination and Response.* Emergencies Science Division. Environment Canada, Ottawa, ON, Canada (pp. 660-693).

French-McCay, D., Crowley, D., Rowe, J. J., Bock, M., Robinson, H., Wenning, R., ... & Parkerton, T. F. (2018). Comparative risk assessment of spill response options for a deepwater oil well blowout: Part 1. Oil spill modeling. *Marine Pollution Bulletin*, 133, 1001-1015.

Galagan, C., McCay, D.F., Rowe, J., McStay, L. (2018). Simulation Modeling of Ocean Circulation and Oil Spills in the Gulf of Mexico Volume II: Appendixes I through V. U.S. Department of the Interior, Bureau of Ocean Energy Management, Gulf of Mexico OCS Region. Retrieved from https://espis.boem.gov/Final%20Reports/BOEM_2018-040.pdf

Gao, Y., Glennon, B., He, Y., & Donnellan, P. (2021). Dissolution kinetics of a bcs class ii active pharmaceutical ingredient: Diffusion-based model validation and prediction. *ACS Omega*, 6(12), 8056-8067.

Garcia-Pineda, O., MacDonald, I. R., Li, X., Jackson, C. R., & Pichel, W. G. (2013). Oil spill

mapping and measurement in the Gulf of Mexico with textural classifier neural network algorithm (TCNNA). *IEEE Journal of Selected Topics in Applied Earth Observations and Remote Sensing*, 6(6), 2517-2525.

Geng, X., Boufadel, M. C., Ozgokmen, T., King, T., Lee, K., Lu, Y., & Zhao, L. (2016). Oil droplets transport due to irregular waves: Development of large-scale spreading coefficients. *Marine Pollution Bulletin*, 104(1-2), 279-289.

Government of Canada (GC). (2020). Regional Assessment of Offshore Oil and Gas Exploratory Drilling East of Newfoundland and Labrador. Final Report. Retrieved from https://iaac-aeic.gc.ca/050/documents/p80156/134068E.pdf

Gros, J., Dissanayake, A. L., Daniels, M. M., Barker, C. H., Lehr, W., & Socolofsky, S. A. (2018). Oil spill modeling in deep waters: Estimation of pseudo-component properties for cubic equations of state from distillation data. *Marine Pollution Bulletin*, 137, 627-637.

Gros, J., Socolofsky, S. A., Dissanayake, A. L., Jun, I., Zhao, L., Boufadel, M. C., ... & Arey, J. S. (2017). Petroleum dynamics in the sea and influence of subsea dispersant injection during Deepwater Horizon. *Proceedings of the National Academy of Sciences*, 114(38), 10065-10070.

Guo, W. (2017). Development of a statistical oil spill model for risk assessment. *Environmental Pollution*, 230, 945-953.

Guyana's Ministry of Natural Resources (GMNR). (2022, December 9). Guyana launches First Licensing Round for Offshore Oil and Gas Exploration and Production. Retrieved from https://petroleum.gov.gy/article/guyanas-gov-launches-first-licensing-round-offshore-

oil-and-gas-exploration-and-production

Harris, P., Alo, B.; Bera, A., Bradshaw, M., Coakley, B., Grosvik, B., Lourenço, N., Moreno, J., Shrimpton, M., Simcock, A. (2015). Chapter 21. Offshore Hydrocarbon Industries. Oxford University Press: Oxford, UK.

Hazen, T. C., Dubinsky, E. A., DeSantis, T. Z., Andersen, G. L., Piceno, Y. M., Singh, N., ... & Mason, O. U. (2010). Deep-sea oil plume enriches indigenous oil-degrading bacteria. *Science*, 330(6001), 204-208.

Hibernia Management & Development Company Ltd (HMDCL). (2020). Hibernia 2018 EEM Report Volume 1. Retrieved from https://www.cnlopb.ca/wp-content/uploads/eem/eem2018hib.pdf

Hinze, J. O. (1955). Fundamentals of the hydrodynamic mechanism of splitting in dispersion processes. *AIChE Journal*, 1(3), 289-295.

Holand, P. (2017). Loss of Well Control Occurrence and Size Estimators, Phase I and II. Report prepared for Bureau of Safety and Environmental Enforcement. Report# ES201471/2, Washington, DC. Retrieved from https://www.bsee.gov/sites/bsee.gov/files/tap-technical-assessment-program/765aa.pdf

Humphrey, B., Owens, E., & Sergy, G. (1993, March). Development of a stranded oil in coarse sediment (SOCS) model. In *International Oil Spill Conference* (Vol. 1993, No. 1, pp. 575-582). American Petroleum Institute.

Humphrey, B., Patrick, G., & Owens, E. H. (1992). Coarse Sediment and Oil Database Fate Model. Environment Canada, Environmental Protection Directorate. Retrieved from https://www.bsee.gov/sites/bsee.gov/files/osrr-oil-spill-response-research/158ai-

pdf.pdf

IEA. (2018). Offshore Energy Outlook. Retrieved from https://www.iea.org/reports/world-energy-outlook-2018/electricity

Johansen, J. L., Allan, B. J., Rummer, J. L., & Esbaugh, A. J. (2017). Oil exposure disrupts early life-history stages of coral reef fishes via behavioural impairments. *Nature Ecology & Evolution*, 1(8), 1146-1152.

Johansen, Ø. (2003). Development and verification of deep-water blowout models. *Marine Pollution Bulletin*, 47(9-12), 360-368.

Johansen, Ø., Brandvik, P. J., & Farooq, U. (2013). Droplet breakup in subsea oil releases–Part 2: Predictions of droplet size distributions with and without injection of chemical dispersants. *Marine Pollution Bulletin*, 73(1), 327-335.

Johansen, Ø., Reed, M., & Bodsberg, N. R. (2015). Natural dispersion revisited. *Marine Pollution Bulletin*, 93(1-2), 20-26.

Jordan, R. E., & Payne, J. R. (1980). Fate and weathering of petroleum spills in the marine environment: a literature review and synopsis. United States.

Kaiser, M. J. (2021). A Review of exploration, development, and production cost offshore Newfoundland. *Natural Resources Research*, 30(2), 1253-1290.

Kashefi, K., Pereira, L. M., Chapoy, A., Burgass, R., & Tohidi, B. (2016). Measurement and modelling of interfacial tension in methane/water and methane/brine systems at reservoir conditions. *Fluid Phase Equilibria*, 409, 301-311.

Kenworthy, W. J., Cosentino-Manning, N., Handley, L., Wild, M., & Rouhani, S. (2017). Seagrass response following exposure to Deepwater Horizon oil in the Chandeleur

Islands, Louisiana (USA). *Marine Ecology Progress Series*, 576, 145-161.

Keramea, P., Spanoudaki, K., Zodiatis, G., Gikas, G., & Sylaios, G. (2021). Oil spill modeling: A critical review on current trends, perspectives, and challenges. *Journal of Marine Science and Engineering*, 9(2), 181.

Kherif, F., & Latypova, A. (2020). Principal component analysis. In Machine Learning (pp. 209-225). Academic Press.

Kujawinski, E. B., Kido Soule, M. C., Valentine, D. L., Boysen, A. K., Longnecker, K., & Redmond, M. C. (2011). Fate of dispersants associated with the Deepwater Horizon oil spill. *Environmental Science & Technology*, 45(4), 1298-1306.

Le Traon, P. Y., Reppucci, A., Alvarez Fanjul, E., Aouf, L., Behrens, A., Belmonte, M., ... & Zacharioudaki, A. (2019). From observation to information and users: The Copernicus Marine Service perspective. *Frontiers in Marine Science*, 6, 234.

Lee, J. H., & Cheung, V. (1990). Generalized Lagrangian model for buoyant jets in current. *Journal of Environmental Engineering*, 116(6), 1085-1106.

Lehr, W., Fraga, R. J., Belen, M. S., & Cekirge, H. M. (1984). A new technique to estimate initial spill size using a modified Fay-type spreading formula. *Marine Pollution Bulletin*, 15(9), 326-329.

Lehr, W., Jones, R., Evans, M., Simecek-Beatty, D., & Overstreet, R. (2002). Revisions of the ADIOS oil spill model. *Environmental Modelling & Software*, 17(2), 189-197.

Li, Z., Spaulding, M. L., & French-McCay, D. (2017). An algorithm for modeling entrainment and naturally and chemically dispersed oil droplet size distribution under surface breaking wave conditions. *Marine Pollution Bulletin*, 119(1), 145-152.

Li, Z., Spaulding, M., McCay, D. F., Crowley, D., & Payne, J. R. (2017). Development of a unified oil droplet size distribution model with application to surface breaking waves and subsea blowout releases considering dispersant effects. *Marine Pollution Bulletin*, 114(1), 247-257.

Lin, H., & Duan, Y. Y. (2005). Empirical correction to the Peng–Robinson equation of state for the saturated region. *Fluid Phase Equilibria*, 233(2), 194-203.

Little, D., Hudson, G., Masotti, R., Deighton, I., & Dale, R. (2021, November). Deep water plays of the Orphan Basin, Offshore Newfoundland, Canada. In *First EAGE Workshop on East Canada Offshore Exploration* (Vol. 2021, No. 1, pp. 1-5). European Association of Geoscientists & Engineers.

Liu, Y., MacFadyen, A., Ji, Z. G., & Weisberg, R. H. (Eds.). (2013). Monitoring and modeling the deepwater horizon oil spill: a record breaking enterprise. John Wiley & Sons.

Liubartseva, S., Federico, I., Coppini, G., & Lecci, R. (2021). Stochastic oil spill modeling for environmental protection at the Port of Taranto (southern Italy). *Marine Pollution Bulletin*, 171, 112744.

Lopez-Echeverry, J. S., Reif-Acherman, S., & Araujo-Lopez, E. (2017). Peng-Robinson equation of state: 40 years through cubics. *Fluid Phase Equilibria*, 447, 39-71.

Mackay, D., & Matsugu, R. S. (1973). Evaporation rates of liquid hydrocarbon spills on land and water. *The Canadian Journal of Chemical Engineering*, 51(4), 434-439.

Mackay, D., Buist, I., Mascarenhas, R., & Patterson, R. (1980). Oil spills processes and models. Canada: Environment Canada, Ottawa. Retrieved from https://publications.gc.ca/collections/collection_2020/eccc/en40/En40-980-1980-

eng.pdf

Makarynskyy, O. (Ed.). (2021). Marine Hydrocarbon Spill Assessments: From Baseline Information Through to Decision Support Tools. Elsevier.

Maslo, A., Panjan, J., & Žagar, D. (2014). Large-scale oil spill simulation using the lattice Boltzmann method, validation on the Lebanon oil spill case. *Marine Pollution Bulletin*, 84(1-2), 225-235.

McNutt, M. K., Camilli, R., Crone, T. J., Guthrie, G. D., Hsieh, P. A., Ryerson, T. B., ... & Shaffer, F. (2012). Review of flow rate estimates of the Deepwater Horizon oil spill. *Proceedings of the National Academy of Sciences*, 109(50), 20260-20267.

Milgram, J. H. (1983). Mean flow in round bubble plumes. *Journal of Fluid Mechanics*, 133, 345-376.

Morton, B. R., Taylor, G. I., & Turner, J. S. (1956). Turbulent gravitational convection from maintained and instantaneous sources. *Proceedings of the Royal Society of London*. Series A. Mathematical and Physical Sciences, 234(1196), 1-23.

Murawski, S. A., Ainsworth, C. H., Gilbert, S., Hollander, D. J., Paris, C. B., Schlüter, M., & Wetzel, D. L. (2020). Deep Oil Spills. Springer.

Murawski, S. A., Ainsworth, C. H., Gilbert, S., Hollander, D. J., Paris, C. B., Schlüter, M., & Wetzel, D. L. (Eds.). (2019). Scenarios and responses to future deep oil spills: fighting the next war. Springer.

Nagpal, N. K. (1993). Ambient water quality criteria for polycyclic aromatic hydrocarbons (PAHs). BC Environment, Water Quality Branch. Retrieved from https://www2.gov.bc.ca/assets/gov/environment/air-land-

water/water/waterquality/water-quality-guidelines/approved-wqgs/bc_env_pah_waterqualityguideline_technical.pdf

National Academies of Sciences, Engineering, and Medicine (NASEM). (2020). The use of dispersants in marine oil spill response. Washington, DC: The National Academies Press. Retrieved from https://doi.org/10.17226/25161.

Nelson, J. R., & Grubesic, T. H. (2017). A repeated sampling method for oil spill impact uncertainty and interpolation. *International Journal of Disaster Risk Reduction*, 22, 420-430.

Nelson, J. R., & Grubesic, T. H. (2018). Oil spill modeling: risk, spatial vulnerability, and impact assessment. *Progress in Physical Geography: Earth and Environment*, 42(1), 112-127.

Nelson, J. R., & Grubesic, T. H. (2019). Oil spill modeling: computational tools, analytical frameworks, and emerging technologies. *Progress in Physical Geography: Earth and Environment*, 43(1), 129-143.

Nelson, J. R., Grubesic, T. H., Sim, L., Rose, K., & Graham, J. (2015). Approach for assessing coastal vulnerability to oil spills for prevention and readiness using GIS and the Blowout and Spill Occurrence Model. *Ocean & Coastal Management*, 112, 1-11.

Neto, A. M. B., Ribeiro, J., Aznar, M., & Bannwart, A. C. (2015). Thermodynamic modeling of vapor-liquid equilibrium for petroleum fluids. *Proc. Blucher Math*, 1(1), 610-619.

Nissanka, I. D., & Yapa, P. D. (2016). Calculation of oil droplet size distribution in an underwater oil well blowout. *Journal of Hydraulic Research*, 54(3), 307-320.

Nissanka, I. D., & Yapa, P. D. (2018). Calculation of oil droplet size distribution in ocean oil

spills: A review. *Marine Pollution Bulletin*, 135, 723-734.

Niu, H., Li, S., Li, P., King, T., & Lee, K. (2017). Stochastic modeling of the fate and behaviors of an oil spill in the Salish Sea. *International Journal of Offshore and Polar Engineering*, 27(04), 337-345.

Pal, R., & Rhodes, E. (1989). Viscosity/concentration relationships for emulsions. *Journal of Rheology*, 33(7), 1021-1045.

Paris, C. B., Berenshtein, I., Trillo, M. L., Faillettaz, R., Olascoaga, M. J., Aman, Z. M., ... & Joye, S. B. (2018). BP Gulf science data reveals ineffectual subsea dispersant injection for the Macondo blowout. *Frontiers in Marine Science*, 5, 389.

Paris, C. B., Hénaff, M. L., Aman, Z. M., Subramaniam, A., Helgers, J., Wang, D. P., ... & Srinivasan, A. (2012). Evolution of the Macondo well blowout: simulating the effects of the circulation and synthetic dispersants on the subsea oil transport. *Environmental Science & Technology*, 46(24), 13293-13302.

Payne, J. R., & Driskell, W. B. (2018). Macondo oil in northern Gulf of Mexico waters–part 1: assessments and forensic methods for Deepwater Horizon offshore water samples. *Marine Pollution Bulletin*, 129(1), 399-411.

Pedersen, K.S., Christensen, P.L., & Shaikh, J.A. (2014). Phase Behavior of Petroleum Reservoir Fluids (2nd ed.). CRC Press. https://doi.org/10.1201/b17887

Pesch, S., Jaeger, P., Jaggi, A., Malone, K., Hoffmann, M., Krause, D., ... & Schlüter, M. (2018). Rise velocity of live-oil droplets in deep-sea oil spills. *Environmental Engineering Science*, 35(4), 289-299.

Prince, R. C., Butler, J. D., & Redman, A. D. (2017). The rate of crude oil biodegradation in

the sea. *Environmental Science & Technology*, 51(3), 1278-1284.

Rajendran, S., Aboobacker, V. M., Seegobin, V. O., Al Khayat, J. A., Rangel-Buitrago, N., Al-Kuwari, H. A. S., ... & Vethamony, P. (2022). History of a disaster: A baseline assessment of the Wakashio oil spill on the coast of Mauritius, Indian Ocean. *Marine Pollution Bulletin*, 175, 113330.

Reddy, C. M., Arey, J. S., Seewald, J. S., Sylva, S. P., Lemkau, K. L., Nelson, R. K., ... & Camilli, R. (2012). Composition and fate of gas and oil released to the water column during the Deepwater Horizon oil spill. *Proceedings of the National Academy of Sciences*, 109(50), 20229-20234.

Reed, M. (1989). The physical fates component of the natural resource damage assessment model system. *Oil and Chemical Pollution*, 5(2-3), 99-123.

Reed, M., Gundlach, E., & Kana, T. (1989). A coastal zone oil spill model: development and sensitivity studies. *Oil and Chemical Pollution*, 5(6), 411-449.

Riazi, M. R. (2021). Oil spill occurrence, simulation, and behavior. CRC Press.

Ron, B. (2019, January 8). BP unlocks a billion oil barrels in Gulf of Mexico with new technology. Reuters. Retrieved from https://www.reuters.com/article/us-bp-discovery-idUSKCN1P21M0

Ryerson, T. B., Camilli, R., Kessler, J. D., Kujawinski, E. B., Reddy, C. M., Valentine, D. L., ... & Warneke, C. (2012). Chemical data quantify Deepwater Horizon hydrocarbon flow rate and environmental distribution. *Proceedings of the National Academy of Sciences*, 109(50), 20246-20253.

Samaras, A. G., De Dominicis, M., Archetti, R., Lamberti, A., & Pinardi, N. (2014). Towards

improving the representation of beaching in oil spill models: A case study. *Marine Pollution Bulletin*, 88(1-2), 91-101.

Sammarco, P. W., Kolian, S. R., Warby, R. A., Bouldin, J. L., Subra, W. A., & Porter, S. A. (2016). Concentrations in human blood of petroleum hydrocarbons associated with the BP/Deepwater Horizon oil spill, Gulf of Mexico. *Archives of Toxicology*, 90(4), 829-837.

Santner, R., Cocklan-Vendl, M., Stong, B., Michel, J., Owens, E. H., & Taylor, E. (2011, March). The Deepwater Horizon MC252-Macondo shoreline cleanup assessment technique (SCAT) program. In *International Oil Spill Conference* (Vol. 2011, No. 1, p. 270).

Shim, C. B., Jung, Y. S., Yoon, J. I., & Joo, H. G. (2011). Application of backward differentiation formula to spatial reactor kinetics calculation with adaptive time step control. *Nuclear Engineering and Technology*, 43(6), 531-546.

Shultz, J. M., Walsh, L., Garfin, D. R., Wilson, F. E., & Neria, Y. (2015). The 2010 Deepwater Horizon oil spill: the trauma signature of an ecological disaster. *The Journal of Behavioral Health Services & Research*, 42, 58-76.

Sim, L., Graham, J., Rose, K., Duran, R., Nelson, J., Umhoefer, J., & Vielma, J. (2015). Developing a comprehensive deepwater blowout and spill model. US Department of Energy, National Energy Technology Laboratory: Albany, NY, USA, 44. Retrieved from https://gsp.humboldt.edu/jimsprofessional/Publications/2015%20Sim%20Developing%20a%20Comprehensive%20Deepwater%20Blowout%20and%20Spill%20Model.pdf

Simecek-Beatty, D., & Lehr, W. J. (2017). Extended oil spill spreading with Langmuir circulation. *Marine Pollution Bulletin*, 122(1-2), 226-235.

Sinaga, K. P., & Yang, M. S. (2020). Unsupervised K-means clustering algorithm. *IEEE access*, 8, 80716-80727.

Socolofsky, S. A., Adams, E. E., Boufadel, M. C., Aman, Z. M., Johansen, Ø., Konkel, W. J., ... & Nedwed, T. J. (2015). Intercomparison of oil spill prediction models for accidental blowout scenarios with and without subsea chemical dispersant injection. *Marine Pollution Bulletin*, 96(1-2), 110-126.

Socolofsky, S. A., Jun, I., Boufadel, M. C., Liu, R., Lu, Y., Arey, J. S., & McFarlin, K. M. (2022). Development of an offshore response guidance tool for determining the impact of SSDI on released gas and benzene from artificial subsea oil well blowout simulations. *Marine Pollution Bulletin*, 184, 114114.

Spanoudaki, K. (2016, April). Mathematical modelling of oil spill fate and transport in the marine environment incorporating biodegradation kinetics of oil droplets. In *EGU General Assembly Conference Abstracts* (pp. EPSC2016-13155).

Spaulding, M., Li, Z., Mendelsohn, D., Crowley, D., French-McCay, D., & Bird, A. (2017). Application of an integrated blowout model system, OILMAP DEEP, to the Deepwater Horizon (DWH) spill. *Marine Pollution Bulletin*, 120(1-2), 37-50.

Spier, C., Stringfellow, W. T., Hazen, T. C., & Conrad, M. (2013). Distribution of hydrocarbons released during the 2010 MC252 oil spill in deep offshore waters. *Environmental Pollution*, 173, 224-230.

Stiver, W., & Mackay, D. (1984). Evaporation rate of spills of hydrocarbons and petroleum

mixtures. *Environmental Science & Technology*, 18(11), 834-840.

Stout, S., & Wang, Z. (Eds.). (2017). Oil Spill Environmental Forensics Case Studies. Butterworth-Heinemann.

Süli, E., & Mayers, D. F. (2003). An introduction to numerical analysis. Cambridge University Press.

Tarr, M.A., Zito, P., Overton, E.B., Olson, G.M., Adhikari, P.L., & Reddy, C.M. (2016). Weathering of oil spilled in the marine environment. *Oceanography*, 29(3), 126-135.

Thrift-Viveros, D. L., Jones, R., & Boufadel, M. (2015, June). Development of a new oil biodegradation algorithm for NOAA's oil spill modelling suite (GNOME/ADIOS). In *Proceedings of the 38th AMOP Technical Seminar*, Vancouver, BC, Canada (pp. 2-4).

US EIA (2023). Independent statistics and analysis. Retrieved from https://www.eia.gov/international/data/world.

Vahabzadeh, M., & Megarbane, B. (2022). A two-decade review of butane toxicity as a substance of abuse. *Basic & Clinical Pharmacology & Toxicology*, 131(3), 155-164.

Wang, C. Y., & Calabrese, R. V. (1987). Drop Breakup in Turbulent Stirred-Tank Contactors. Part II: Relative Influence of Viscosity and Interfacial Tension.

Wang, D., Guo, W., Kong, S., & Xu, T. (2020). Estimating offshore exposure to oil spill impacts based on a statistical forecast model. *Marine Pollution Bulletin*, 156, 111213.

Wang, Q., Lü, Y., & Li, Q. (2022). A review on submarine oil and gas leakage in near field: droplets and plume. *Environmental Science and Pollution Research*, 1-14.

Willmott, C. J., Ackleson, S. G., Davis, R. E., Feddema, J. J., Klink, K. M., Legates, D. R., ... & Rowe, C. M. (1985). Statistics for the evaluation and comparison of models. *Journal*

of Geophysical Research: Oceans, 90(C5), 8995-9005.

Willmott, C. J., Robeson, S. M., Matsuura, K., & Ficklin, D. L. (2015). Assessment of three dimensionless measures of model performance. *Environmental Modelling & Software*, 73, 167-174.

World Wildlife Fund (WWF). (2019, Sep 6). Northeast Newfoundland Marine Refuge should be exempt from oil and gas development. Retrieved from https://wwf.ca/media-releases/northeast-newfoundland-marine-refuge-should-be-exempt-from-oil-and-gas-development-wwf-canada/

Wright, B. (2023, April 20). Newfoundland & Labrador Launches Two Offshore Licensing rounds. JPT. Retrieved from https://jpt.spe.org/newfoundland-labrador-launches-two-offshore-licensing-rounds

Wüest, A., Brooks, N. H., & Imboden, D. M. (1992). Bubble plume modeling for lake restoration. *Water Resources Research*, 28(12), 3235-3250.

Xie, H., Yapa, P. D., & Nakata, K. (2007). Modeling emulsification after an oil spill in the sea. *Journal of Marine Systems*, 68(3-4), 489-506.

Yang, F., Xie, C., Xu, S., Ning, Z., & Krooss, B. M. (2017). Supercritical methane sorption on organic-rich shales over a wide temperature range. *Energy & Fuels*, 31(12), 13427-13438.

Yang, Z., Chen, Z., & Lee, K. (2023). Development and testing of a 2D offshore oil spill modeling tool (OSMT) supported by an effective calibration method. *Marine Pollution Bulletin*, 188, 114696.

Yang, Z., Chen, Z., Lee, K., Owens, E., Boufadel, M. C., An, C., & Taylor, E. (2021). Decision

support tools for oil spill response (OSR-DSTs): Approaches, challenges, and future research perspectives. *Marine Pollution Bulletin*, 167, 112313.

Yapa, P. D., Wimalaratne, M. R., Dissanayake, A. L., & DeGraff Jr, J. A. (2012). How does oil and gas behave when released in deepwater?. *Journal of Hydro-Environment Research*, 6(4), 275-285.

Zeinstra-Helfrich, M., Koops, W., & Murk, A. J. (2017). Predicting the consequence of natural and chemical dispersion for oil slick size over time. *Journal of Geophysical Research: Oceans, 122(9)*, 7312-7324.

Zelenke, B., O'Connor, C., Barker, C. H., Beegle-Krause, C. J., & Eclipse, L. (2012). General NOAA operational modeling environment (GNOME) technical documentation. Retrieved from https://response.restoration.noaa.gov/sites/default/files/GNOME_Tech_Doc.pdf

Zhao, L., Boufadel, M. C., Adams, E., Socolofsky, S. A., King, T., Lee, K., & Nedwed, T. (2015). Simulation of scenarios of oil droplet formation from the Deepwater Horizon blowout. *Marine Pollution Bulletin*, 101(1), 304-319.

Zhao, L., Boufadel, M. C., King, T., Robinson, B., Gao, F., Socolofsky, S. A., & Lee, K. (2017). Droplet and bubble formation of combined oil and gas releases in subsea blowouts. *Marine Pollution Bulletin*, 120(1-2), 203-216.

Zhao, L., Boufadel, M. C., Socolofsky, S. A., Adams, E., King, T., & Lee, K. (2014b). Evolution of droplets in subsea oil and gas blowouts: Development and validation of the numerical model VDROP-J. *Marine Pollution Bulletin*, 83(1), 58-69.

Zhao, L., Mitchell, D. A., Prince, R. C., Walker, A. H., Arey, J. S., & Nedwed, T. J. (2021).

Deepwater Horizon 2010: Subsea dispersants protected responders from VOC exposure. *Marine Pollution Bulletin*, 173, 113034.

Zhao, L., Torlapati, J., Boufadel, M. C., King, T., Robinson, B., & Lee, K. (2014a). VDROP: A comprehensive model for droplet formation of oils and gases in liquids-Incorporation of the interfacial tension and droplet viscosity. *Chemical Engineering Journal*, 253, 93-106.

Zheng, L., & Yapa, P. D. (2000). Buoyant velocity of spherical and nonspherical bubbles/droplets. *Journal of Hydraulic Engineering*, 126(11), 852-854.

Zheng, L., & Yapa, P. D. (2002). Modeling gas dissolution in deepwater oil/gas spills. *Journal Of Marine Systems*, 31(4), 299-309.

Zhu, K., Mu, L., & Xia, X. (2021). An ensemble trajectory prediction model for maritime search and rescue and oil spill based on sub-grid velocity model. *Ocean Engineering*, 236, 109513.

Appendices

A: Solution Techniques

1. Trilinear interpolation

The trilinear equation is derived by applying the linear interpolation multiple times. It approximates the value of a function at an intermediate point $C\ (x, y, z)$ within the local axial rectangular prism linearly using data on the lattice points (Figure A-1).

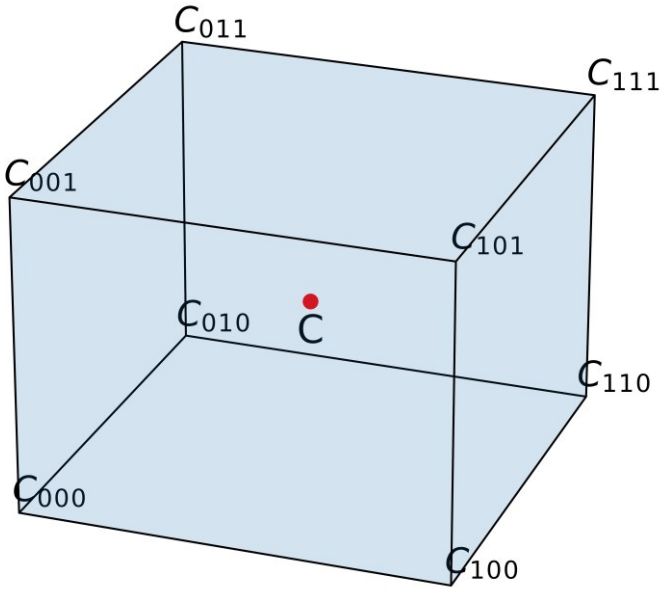

Figure A-1 Schematic of trilinear interpolation.

The solution to the interpolation problem can be expressed as:

$$f(x, y, z) = a_0 + a_1x + a_2y + a_3z + a_4xy + a_5xz + a_6yz + a_7xyz \qquad \text{(A-1)}$$

where the coefficients are solved by the linear system below:

$$\begin{bmatrix} 1 & x_0 & y_0 & z_0 & x_0y_0 & x_0z_0 & y_0z_0 & x_0y_0z_0 \\ 1 & x_1 & y_0 & z_0 & x_1y_0 & x_1z_0 & y_0z_0 & x_1y_0z_0 \\ 1 & x_0 & y_1 & z_0 & x_0y_1 & x_0z_0 & y_1z_0 & x_0y_1z_0 \\ 1 & x_1 & y_1 & z_0 & x_1y_1 & x_1z_0 & y_1z_0 & x_1y_1z_0 \\ 1 & x_0 & y_0 & z_1 & x_0y_0 & x_0z_1 & y_0z_1 & x_0y_0z_1 \\ 1 & x_1 & y_0 & z_1 & x_1y_0 & x_1z_1 & y_0z_1 & x_1y_0z_1 \\ 1 & x_0 & y_1 & z_1 & x_0y_1 & x_0z_1 & y_1z_1 & x_0y_1z_1 \\ 1 & x_1 & y_1 & z_1 & x_1y_1 & x_1z_1 & y_1z_1 & x_1y_1z_1 \end{bmatrix} \begin{bmatrix} a_0 \\ a_1 \\ a_2 \\ a_3 \\ a_4 \\ a_5 \\ a_6 \\ a_7 \end{bmatrix} = \begin{bmatrix} c_{000} \\ c_{100} \\ c_{010} \\ c_{110} \\ c_{001} \\ c_{101} \\ c_{011} \\ c_{111} \end{bmatrix}$$

here x_0 denotes the lattice point below x, and x_1 denotes the lattice point above x and similarly for y_0, y_1, z_0, z_1. Solving this system can yield the result:

$$a_0 = \frac{-c_{000}x_1y_1z_1+c_{001}x_1y_1z_0+c_{010}x_1y_0z_1-c_{011}x_1y_0z_0}{(x_0-x_1)(y_0-y_1)(z_0-z_1)} + \frac{c_{100}x_0y_1z_1-c_{101}x_0y_1z_0-c_{110}x_0y_0z_1+c_{111}x_0y_0z_0}{(x_0-x_1)(y_0-y_1)(z_0-z_1)} \tag{A-2}$$

$$a_1 = \frac{c_{000}y_1z_1-c_{001}y_1z_0-c_{010}y_0z_1+c_{011}y_0z_0}{(x_0-x_1)(y_0-y_1)(z_0-z_1)} + \frac{-c_{100}y_1z_1+c_{101}y_1z_0+c_{110}y_0z_1-c_{111}y_0z_0}{(x_0-x_1)(y_0-y_1)(z_0-z_1)} \tag{A-3}$$

$$a_2 = \frac{c_{000}x_1z_1-c_{001}x_1z_0-c_{010}x_1z_1+c_{011}x_1z_0}{(x_0-x_1)(y_0-y_1)(z_0-z_1)} + \frac{-c_{100}x_0z_1+c_{101}x_0z_0+c_{110}x_0z_1-c_{111}x_0z_0}{(x_0-x_1)(y_0-y_1)(z_0-z_1)} \tag{A-4}$$

$$a_3 = \frac{c_{000}x_1y_1-c_{001}x_1y_1-c_{010}x_1y_0+c_{011}x_1y_0}{(x_0-x_1)(y_0-y_1)(z_0-z_1)} + \frac{-c_{100}x_0y_1+c_{101}x_0y_1+c_{110}x_0y_0-c_{111}x_0y_0}{(x_0-x_1)(y_0-y_1)(z_0-z_1)} \tag{A-5}$$

$$a_4 = \frac{-c_{000}z_1+c_{001}z_0+c_{010}z_1-c_{011}z_0+c_{100}z_1-c_{101}z_0-c_{110}z_1+c_{111}z_0}{(x_0-x_1)(y_0-y_1)(z_0-z_1)} \tag{A-6}$$

$$a_5 = \frac{-c_{000}y_1+c_{001}y_1+c_{010}y_0-c_{011}y_0+c_{100}y_1-c_{101}y_1-c_{110}y_0+c_{111}y_0}{(x_0-x_1)(y_0-y_1)(z_0-z_1)} \tag{A-7}$$

$$a_6 = \frac{-c_{000}x_1+c_{001}x_1+c_{010}x_1-c_{011}x_1+c_{100}x_0-c_{101}x_0-c_{110}x_0+c_{111}x_0}{(x_0-x_1)(y_0-y_1)(z_0-z_1)} \tag{A-8}$$

$$a_7 = \frac{c_{000}-c_{001}-c_{010}+c_{011}-c_{100}+c_{101}+c_{110}-c_{111}}{(x_0-x_1)(y_0-y_1)(z_0-z_1)} \tag{A-9}$$

2. BDF5

The first order ODEs can be written as:

$$y' = f(t, y) \tag{A-10}$$

with initial condition $y(t_0) = y_0$ in the interval $a \leq t \leq b$.

The BDF5 is expressed an implicit form as below:

$$y_{n+1} - y_n = hf(t_{n+1}, y_{n+1}) \tag{A-11}$$

$$y_{n+2} - \frac{4}{3}y_{n+1} + \frac{1}{3}y_n = \frac{2}{3}hf(t_{n+2}, y_{n+2}) \tag{A-12}$$

$$y_{n+3} - \frac{18}{11}y_{n+2} + \frac{9}{11}y_{n+1} - \frac{2}{11}y_n = \frac{6}{11}hf(t_{n+3}, y_{n+3}) \quad \text{(A-13)}$$

$$y_{n+4} - \frac{48}{25}y_{n+3} + \frac{36}{25}y_{n+2} - \frac{16}{25}y_{n+1} + \frac{3}{25}y_n = \frac{12}{25}hf(t_{n+4}, y_{n+4}) \quad \text{(A-14)}$$

$$y_{n+5} - \frac{300}{137}y_{n+4} + \frac{300}{137}y_{n+3} - \frac{200}{137}y_{n+2} + \frac{75}{137}y_{n+1} - \frac{12}{137}y_n = \frac{60}{137}hf(t_{n+5}, y_{n+5}) \quad \text{(A-15)}$$

where h represents the step size and $t_n = t_0 + nh$.

3. Adaptive step size control

For the n^{th} order method, the local error at the i-th point is approximated by:

$$e_i^{(n)} \cong y_i^{(n)} - y_i^{(n-1)} \quad \text{(A-16)}$$

where $y_i^{(n)}$ is the estimated solution obtained by the n^{th} order method and $y_i^{(n-1)}$ is the estimated solution obtained by the $n-1^{th}$ order method.

The local error in each step need to satisfy the following condition:

$$|e_i| \leq \varepsilon \quad \text{(A-17)}$$

where $\varepsilon = r|y_i| + a_i$ is the specified error tolerance, the scalar relative error tolerance r has a default value of 10^{-3}, and the vector of absolute error tolerances a_i has by default all its values equal to 10^{-6}.

Once the local error does not meet this criteria, the step size is adjusted as below:

$$h_i = (\frac{\varepsilon}{e_i})^{\frac{1}{n}} h_i' \quad \text{(A-18)}$$

where h_i and h_i' are the new time step size and the old time step at the i^{th} step, respectively.

B: Two-phase Flash Calculations

1. Flash calculation development

Flash calculation algorithms aim to determine the fraction of gas and liquid and the composition of each phase at equilibrium. From a thermodynamic viewpoint, a necessary condition of equilibrium is that the fugacities of the individual components should be the same for an isothermal system. Considering the case of two-phase equilibrium in a N_c-component mixture of an overall composition z, the fugacities of liquid $\hat{f}_i^l$ and gas $\hat{f}_i^v$ are:

$$\hat{f}_i^l = \hat{f}_i^v, i = 1,2, \dots, N_c \tag{A-19}$$

The thermodynamic model enables to calculate component fugacities, given temperature T, pressure P, and phase composition (x in liquid and y in gas):

$$\hat{f}_i^l = \hat{f}_i(T, P, x) =, \hat{f}_i^v = \hat{f}_i(T, P, y) \tag{A-20}$$

The equilibrium factor of i-th component K_i is the ratio of the liquid fugacity coefficient to the gas fugacity coefficient:

$$K_i = \frac{\emptyset_i^l}{\emptyset_i^v} = \frac{\hat{f}_i^l/(x_i P)}{\hat{f}_i^v/(y_i P)} = \frac{y_i}{x_i}\frac{\hat{f}_i^l}{\hat{f}_i^v} \tag{A-21}$$

where $K_i = \frac{y_i}{x_i}$ at equilibrium.

The Rachford-Rice equation derived from material balance is

$$g(V) = \sum_{i=1}^{C} z_i \frac{K_i - 1}{1 - V + VK_i} \tag{A-22}$$

$$g'(V) = -\sum_{i=1}^{C} z_i \frac{(K_i - 1)^2}{1 - V + VK_i} \tag{A-23}$$

where V is the overall fraction of vapor phase.

2. PR-EOS

PR-EOS can be expressed in the form:

$$P = \frac{RT}{v - b} - \frac{a(T)}{v(v+b) + b(v-b)} \tag{A-24}$$

where v is the molar volume, $a(T)$ is the temperature-dependent attractive parameter, b is the co-volume parameter. For the pure component i, $a(T)$ and b are:

$$a(T) = a_c\alpha(T) = a_c\left(1 + m\left(1 - \sqrt{\frac{T}{T_c}}\right)\right)^2 \tag{A-25}$$

$$b = 0.07780\frac{RT_c}{P_c} \tag{A-26}$$

$$a_c = 0.45724\frac{R^2{T_c}^2}{P_c} \tag{A-27}$$

$$m = \begin{cases} 0.37464 + 1.54226\omega - 0.26992\omega^2, & \omega \le 0.49 \\ 0.379642 + 1.48503\omega - 0.164423\omega^2 + 0.016666\omega^3, & \omega > 0.49 \end{cases} \tag{A-28}$$

where T_c and P_c are the critic temperature and pressure. The acentric factor ω means the deviation of the molecular shape from spherically symmetric structure.

For a muti-component system, the mixing rule is required to describe the prevailing forces between molecules of different components forming the mixture. $a(T)$ and b for a mixture are described as:

$$b = \sum_j y_j b_j \tag{A-29}$$

$$a(T) = \sum_i \sum_j y_i y_j \left(1 - \delta_{ij}\right)[a(T)_i a(T)_j]^{\frac{1}{2}} \tag{A-30}$$

where δ_{ij} is the binary interaction parameter between components i and j.

For computation of the compressibility factor Z, PR-EOS can be rewritten as:

$$Z^3 - (1 - B)Z^2 + (A - 3B^2 - 2B)Z - (AB - B^2 - B^3) = 0 \tag{A-31}$$

$$A = \frac{aP}{R^2T^2} \quad B = \frac{bP}{RT} \tag{A-32}$$

The fugacity of a petroleum fluid of a muti-component system is calculated by:

$$f = e^{-\ln(Z-B)+(Z-1)B_p - \frac{A}{2^{1.5}B}\left[A_p - B_p\right]\ln\left(\frac{Z+(2^{0.5}+1)B}{Z-(2^{0.5}-1)B}\right)} \tag{A-33}$$

$$A_p = \frac{2a(T)^{\frac{1}{2}}\sum_{j=1}^{N} y_j a_j (1-\delta_{ij})}{a(T)} \qquad B_p = b_i / \sum b_i \tag{A-34}$$

3. Flash calculation procedure

The successive substitution method is implemented until its convergence is satisfied

(Figure B-1). The flash calculation procedure is as follows:

Step 1: feeding the input data including temperature, pressure and fluid composition with the molar fractions of each component. The thermodynamic properties known for each component include molecular weight, critical temperature and pressure, critical volume, critical compressibility factor, and acentric factor.

Step 2: obtain an estimate for K_i using Wilson's correlation as below:

$$\ln(K_i) = \ln\left(\frac{P_{c,i}}{P}\right) + 5.373(1+\omega_i)(1-\frac{T_{c,i}}{T}) \quad \text{(A-35)}$$

Step 3: using the Newton-Raphson method to solve the Rachford-Rice equation as:

$$V_{n+1} = V_n - \frac{g(V_n)}{g'(V_n)} \quad \text{(A-36)}$$

The error function is $\left|\frac{V_{n+1}-V_n}{V_{n+1}}\right|$, and this criterion for convergence a tolerance is 10^{-5}.

Step 4: compute the mole fractions of components in the vapor and liquid:

$$x_i = \frac{z_i}{1-\beta+\beta K_i} \quad y_i = \frac{K_i z_i}{1-\beta+\beta K_i} \quad \text{(A-37)}$$

Step 5: compute the compressibility factor using the Newton-Raphson method.

Step 6: compute the fugacity coefficients of the vapor and liquid phases ($\hat{f}_i^l$ and $\hat{f}_i^v$) using the new compressibility factors.

Step 7: update K_i and check if the convergence condition is satisfied:

$$\left(\frac{f_L}{f_v} - 1\right)^2 < 10^{-8} \quad \text{(A-38)}$$

Step 8: repeat steps 2- 7 until convergence is attained.

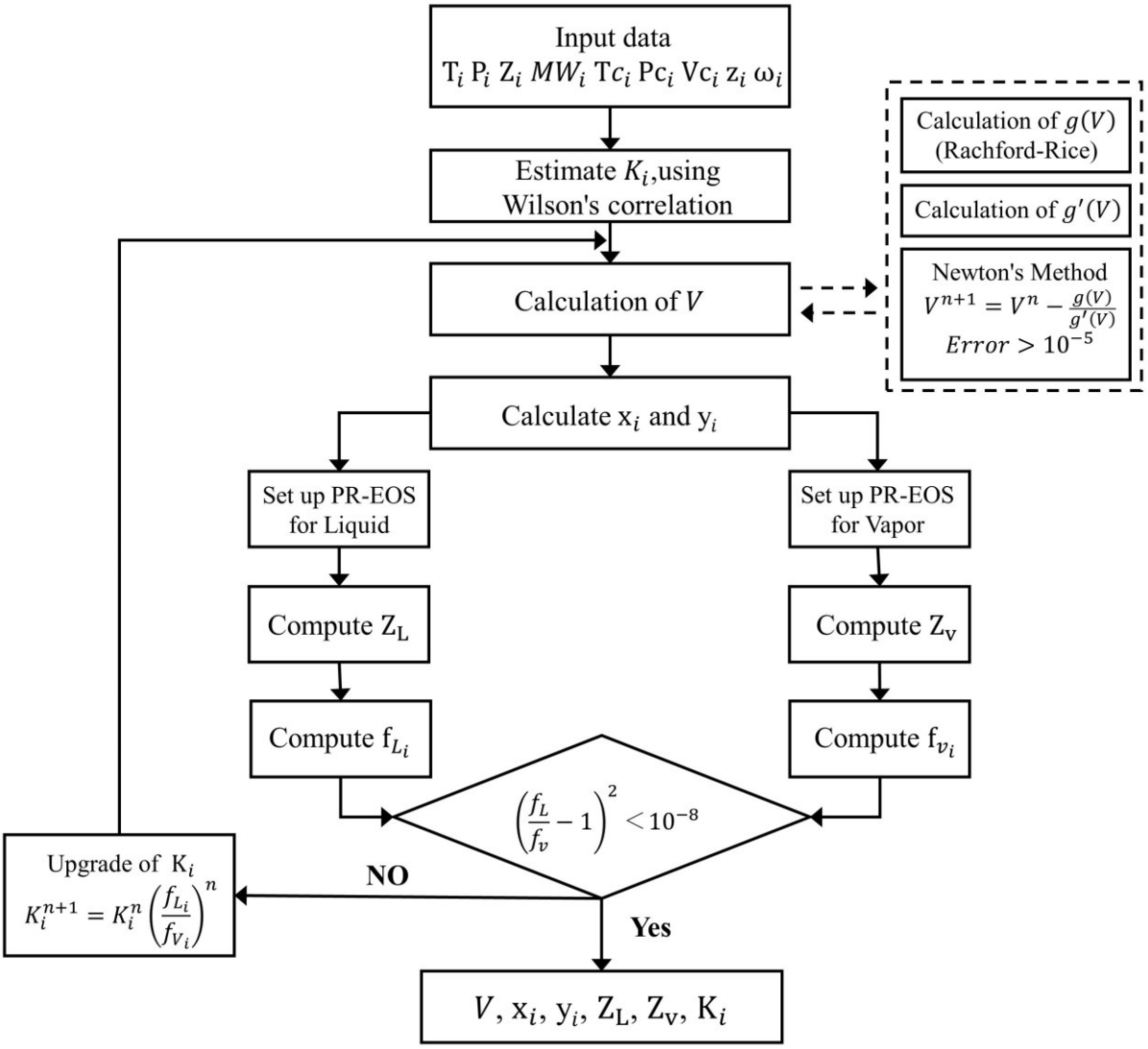

Figure B-2 Flowchart of two-phase flash calculations (modified from Neto et al. (2015)).

C: Risk Assessment

Table C-1 The thresholds for surface oil pollution, modified from Galagan *et al.* (2018).

Threshold	Scaling coefficient	Rationale
		Concentration of PAHs (C_{PAH} in μg/l)
$C_{PAHs} = 0$	0	No impacts.
$0 < C_{PAHs} \leq 1$	1	A screening threshold of 1μg/l is commonly applied to assess potential impacts on sensitive marine resources and early life stages because no significant ecological effects were found when exposure concentration was below this level.
$1 < C_{PAHs} \leq 10$	2	Exposure exceeding 10μg/l may induce sublethal effects on the aqueous biota.
$10 < C_{PAHs} \leq 1000$	3	Sublethal and chronic toxicity of PAHs to most marine animals (Nagpal, 1993); acutely toxic to some aquatic biota (French-McCay, 2018).
$1000 < C_{PAHs}$	4	Lethal concentration 50 (LC_{50}) of PAHs to majority of marine aquatic life (Nagpal, 1993).
		Surface oil loading (δ in g/m^2)
$0 \leq \delta < 0.01$	0	No impacts.
$0.01 \leq \delta < 1$	1	Appear as barely visible or sporadic or rainbow sheen. A conservative threshold to assess the potential impact on socioeconomic resources.
$1 \leq \delta < 10$	2	Appear as sporadic sheen or rainbow sheen (Fingas, 2018). A conservative threshold for assessing sublethal effects of surface oil on marine life.
$10 \leq \delta < 1000$	3	Mostly thick oil (Fingas, 2018). Sublethal effects on marine mammals and sea turtles.
$1000 \leq \delta$	4	Thick oil or water-in-oil emulsion (Fingas, 2018). Risk of mortality for all marine life.

D: Supporting Material for Chapter 4

Table D-1 A summary of inputs to DWOSM for simulating a hypothetical oil blowout.

Parameter	Value (unit)	Source
Oil flow rate at the release point	3000 (bbl/day)	-
GOR	0 (scf/bbl)	
Depth of the release point	800 (m)	-
Equivalent circular diameter of the release	0.05 (m)	-
Release duration	2021.10.20 12:00 - 10.30 12:00 10:30	-
Release interval	15 min	-
Location	Latitude: 50.11 Longitude: -49.67	-
Substance released	Representative east coast Canadian crude recovered off the coast of Newfoundland	The ADIOS Oil Database
Number of oil elements in each release interval	10	-
Current data	NetCDF file	Global Ocean 1/12° Physics Analysis and Forecast updated Daily
Wind data	NetCDF file	Global Ocean Wind L4 Near real Time 6 hourly Observations
Coefficients for surface horizontal diffusion, subsurface horizontal diffusion, subsurface vertical diffusion	10^5, 10^3, 10 (cm^2/s)	-

E: Supporting Material for Chapter 5

Table E-1 A summary of model inputs for the DWH hindcast.

Parameter	Value (unit)	Source
Current data	HYCOM + NCODA Gulf of Mexico 1/25° Reanalysis (GOMu0.04/expt_50.1)	Cummings & Smedstad., 2013.
CTD data	Derive from the interpolated current data	
Wind data	ERA5 hourly data	Hersbach *et al.*, 2023
Shoreline data	Global Self-consistent, Hierarchical, High-resolution Geography Database (GSHHG)	Wessel & Smith, 1996
Spill site location	88.366◦W, 28.738◦N at the water depth of 1500 m	McNutt *et al.*, 2012; Reddy *et al.*, 2012
GOR	1600 standard cubic feet of gas per barrel of oil (scf/bbl)	
Oil flow rate	60000 (bbl/day)	
Oil type and properties	A crude oil produced from the GOM	The ADIOS Oil Database
Gas composition	Measurement for the mass fraction and chemical composition of natural gas released from BP blowout	Reddy *et al.*, 2012
Release diameter	0.48 (m)	Crowley *et al.*, 2018
Simulation duration	2010.04.22 10:30 - 05.06 10:30 (CDT time)	-
Particle release frequency	30 particles (15 droplets + 15 bubbles) emanating from the near-field model per 15 mins	-
Horizontal diffusion coefficients	10^6 cm^2/s for surface LEs 10^3 cm^2/s for subsurface LEs	French-McCay *et al.*, 2021b
Vertical diffusion coefficients	1 cm^2/s for subsurface LEs	
SSDI application	Strat from 2010.04.30 12:00 (CDT time)	Ramírez-León, 2012
Step size for simulation	15 (min)	-